Summer 2016

The Deoxygenation and Hydrogenation Properties of Noble Metal-Based Bimetallic Phosphide Catalysts

Paul M. Cochran
Western Washington University, cochrap@students.wwu.edu

The Deoxygenation and Hydrogenation Properties of Noble Metal-Based Bimetallic Phosphide Catalysts

By

Paul M. Cochran

Accepted in Partial Completion

Of the Requirements for the Degree

Master of Science

Kathleen L. Kitto, Dean of the Graduate School

ADVISORY COMMITTEE

Chair, Dr. Mark E. Bussell

Dr. Gregory W. O'Neil

Dr. Robert F. Berger

MASTER'S THESIS

In presenting this thesis in partial fulfillment of the requirements for a master's degree at Western Washington University, I grant to Western Washington University the non-exclusive royalty-free right to archive, reproduce, distribute, and display the thesis in any and all forms, including electronic format, via any digital library mechanisms maintained by WWU.

I represent and warrant this is my original work, and does not infringe or violate any rights of others. I warrant that I have obtained written permissions from the owner of any third party copyrighted material included in these files.

I acknowledge that I retain ownership rights to the copyright of this work, including but not limited to the right to use all or part of this work in future works, such as articles or books.

Library users are granted permission for individual, research and non-commercial reproduction of this work for educational purposes only. Any further digital posting of this document requires specific permission from the author.

Any copying or publication of this thesis for commercial purposes, or for financial gain, is not allowed without my written permission.

Signature: Paul Cochran

Date: 6/24/2016

The Deoxygenation and Hydrogenation Properties of Noble Metal-Based Bimetallic Phosphide Catalysts

A Thesis

Presented to

The Faculty of

Western Washington University

In Partial Fulfillment

Of the Requirements for the Degree

Master of Science

By

Paul Cochran

June 2016

Abstract

With increasing concern regarding the environmental impacts of fossil fuels, and the difficulty of extracting petroleum feedstocks, alternative liquid fuels are becoming more desirable. Bio-oil, which is oil derived from biomass, is a renewable source of liquid fuels. However, the high oxygen and water content of bio-oil results in high corrosivity and low energy density, making it unusable in the current liquid fuel infrastructure. The process of removing heteroatom impurities from oil is known as hydrotreating. Current hydrotreating catalysts are optimized for refinement of petroleum, and are not suitable for bio-oil deoxygenation. Transition metal phosphides (such as Ru_2P) are a class of materials that have garnered interest recently for their unique electronic, magnetic, and catalytic properties. Several metal-rich phosphide phases have also demonstrated promising hydrotreating activity and resistance to deactivation compared to noble metal catalysts. Some bimetallic phosphide phases have been shown to possess even greater activity than their monometallic counterparts due to synergistic effects between the constituent metals.

A series of $Co_xRu_{2-x}P$ ($0 \leq X \leq 2$) and $Co_xRh_{2-x}P$ ($0 \leq X \leq 2$) catalysts supported on silica (SiO_2) were prepared via impregnation followed by temperature programmed reduction (TPR). The furan and crotonaldehyde deoxygenation properties of the $Co_xRu_{2-x}P/SiO_2$ catalysts were investigated and it was observed that the Co-rich catalysts possessed a higher activity than the Ru-rich catalysts with selectivity towards decarbonylation pathways and the production of C_3 hydrocarbons. The $Co_xRu_{2-x}P/SiO_2$ series showed no deactivation over 48 h in an 8 mol% furan/H_2 feed at 578 K. The crotonaldehyde deoxygenation properties of the $Co_xRh_{2-x}P/SiO_2$ were also investigated, and found to be more active than the $Co_xRu_{2-x}P/SiO_2$ catalysts, with the Rh-rich catalysts possessing greater crotonaldehyde conversions than the Co-rich catalysts.

Acknowledgements

Research Advisor: Dr. Mark E. Bussell

Thesis Committee Members: Dr. Gregory W. O'Neil

Dr. Robert F. Berger

Research Group Members: Peter Topalian, Tess Clinkingbeard, Catherine Miles, and Sam Danforth

Instrument Support: Clint Burgess, Charles Wandler, and Kyle Mikkelsen

Financial Support: National Science Foundation

Western Washington University Chemistry Department

Western Washington University Advanced Materials Science and Engineering Center

Table of Contents

List of Figures

List of Tables

Introduction

1.1 Biofuels

Liquid fuels are an important part of the global transportation system, with petroleum-derived liquid fuel consumption accounting for nearly 33% of total world energy consumption in 2012.[1] Global consumption of liquid fuels is projected to continue increasing for the foreseeable future as nations in the Middle East, Africa, South America, and Asia continue to grow and develop.[2] Liquid fuels are well-suited for use in the transportation and industrial sectors due to their high energy density and stability. While many of the alternative and renewable sources of energy (nuclear, wind, solar, etc.) being developed are promising, transitioning industrial and transportation infrastructure away from the consumption of liquid fuels would be both expensive and impractical, necessitating the development of renewable sources of energy which are compatible with existing fuel infrastructure. Biofuels, or fuels derived from biomass, are promising alternatives to fossil fuels. They are renewable, possess a smaller carbon footprint than fossil fuels, can be used in existing liquid fuel infrastructure, and in many cases can be mixed directly with petroleum-derived fuels such as diesel, gasoline, and aviation fuel. Biofuels also typically possess lower sulfur contents than petroleum-based fuels, and as such their combustion carries a lower tendency for poisoning the expensive reforming catalysts used in emission control devices.[3]

There are currently three classes of feedstock for the production of biofuels, depending on the source of the biomass used. First generation biofuels are derived from plant matter consumable by humans, such as corn, and typically take the form of either ethanol derived from fermentation of sugars, or biodiesel produced from the transesterification of edible oils. First generation biofuels are easy to produce relative to those produced from other biomass feedstocks; however, the fact that their production consumes food crops makes them problematic for long term or large scale use as

alternative fuels. Second generation biofuels are derived from biomass unfit for human consumption, commonly lignocellulosic biomass such as wood, agricultural waste, or switch grass. Second generation biofuels can take the form of either ethanol produced from cellulose or bio-oil derived fuels produced from any form of lignocellulosic biomass. Second generation biofuels do not compete with food crops for feedstocks, but, the lignocellulosic structure of second generation biomass makes fuel production energy intensive, typically requiring the use of a thermal degradation process such as pyrolysis. One advantage to second generation biofuels is the diversity of available biomass; nearly any biomass, including municipal waste and other forms of waste biomass can be used to produce fuels, making second generation biofuels a versatile energy source. Finally, third generation biofuels are sourced from algal feedstocks, and can be used to produce many different liquid fuels, including ethanol, gasoline, diesel, and jet fuel. Third generation feedstocks show promise for use in production of liquid fuels as algae has the potential to be farmed in a variety of climates. However, there are concerns regarding the water and phosphorous costs of growing algae that must first be answered before it can be farmed on an industrial scale. Additionally, the technology used to process algal biomass into consumable fuels is still in its infancy.

Bio-oil produced from the degradation of second generation biomass is currently the most promising source of renewable liquid fuel, as it does not compete with the food industry for crops and is simpler and more cost efficient to produce than algal bio-oils. The lignocellulosic biomass used to produce bio-oil is also relatively inexpensive and abundant relative to other biofuel feedstocks.[4] Lignocellulosic biomass is primarily composed of three classes of compounds: cellulose - a large, straight-chain polysaccharide composed of glucose monomers; hemicellulose - a family of shorter, branched-chain polysaccharides composed of many different sugar monomers; and lignin - a complex and oxygen-rich phenolic polymer which lacks a primary structure (Fig. 1.1).[5] It is

important to note the presence of oxygen in all of the major constituents of lignocellulosic biomass, as this high oxygen content affects the properties of the bio-oil produced.

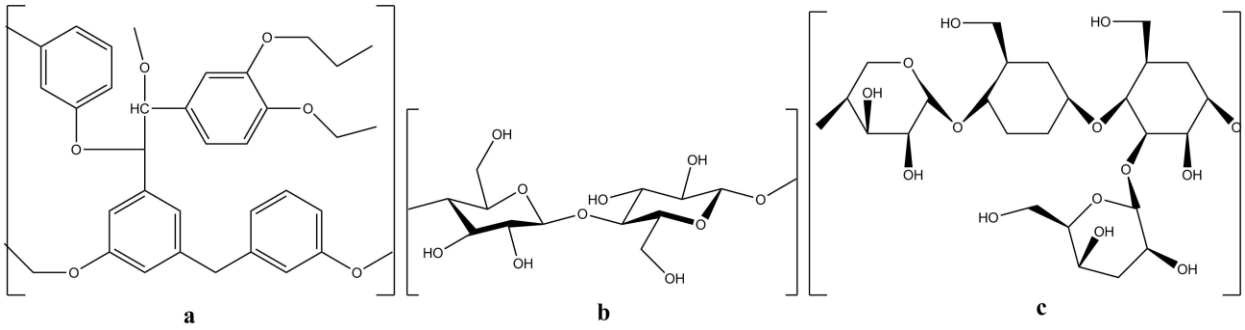

Figure 1.1: Example structures of the constituent polymers of lignocellulosic biomass: a) lignin, b) cellulose, c) hemicellulose.[5]

1.2 Bio-oil

There are several thermochemical processes that can be used to convert biomass to hydrocarbon fuels, including gasification, liquefaction, and pyrolysis.[6] The most promising of these techniques is fast pyrolysis (Fig. 1.2), or the thermochemical decomposition of biomass in the absence of oxygen at high temperatures (typically between 648-800 K), and it is preferentially used over other thermochemical conversion techniques due to the lower capital investment required and the high fraction of liquid product, known as pyrolysis oil, that it produces.[4,6,7]

Three product fractions are produced from fast pyrolysis; a gas fraction that can be combusted to heat the pyrolysis reactor; solid products, also known as bio-char, which are used as fuel, soil amendments, or as a carbon sink; and finally the liquid fraction, commonly referred to as bio-oil or pyrolysis oil.[6] Pyrolysis reactors tend to generate very little waste, as most of the non-liquids generated can be used in other applications. The distribution of products generated by pyrolysis is determined by the rate at which biomass is heated, with methods being categorized as

either fast or slow pyrolysis. Faster pyrolysis methods have been shown to generate a larger fraction of liquid product, making them desirable for use over slow pyrolysis in the conversion of biomass.[6]

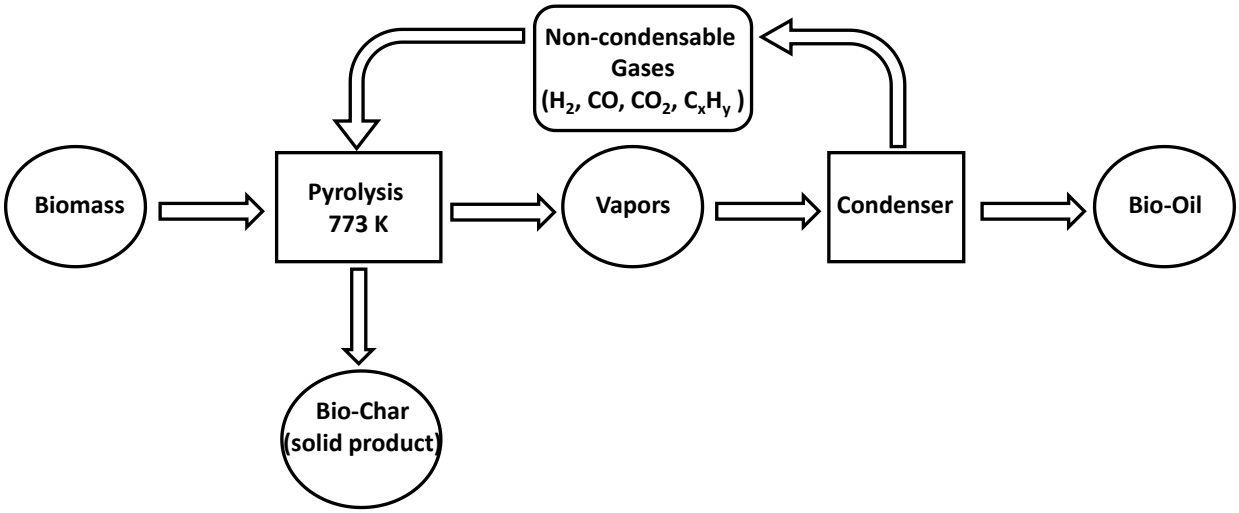

Figure 1.2: Biomass fast pyrolysis diagram.[6,8,9]

The specific source of biomass (i.e. pine wood, switch grass, municipal waste) used to produce pyrolysis oil changes the chemical composition of the resulting bio-oil. There are, however, general trends in bio-oil composition that necessitate different refinement processes than those used for petroleum (Table 1.1).

Table 1.1: Bio-oil *vs.* crude oil characteristics.[6]

	Bio-oil	**Crude Oil**
Water (wt%)	15-30	0.1
pH	2.8-3.8	-
Density (kg/L)	1.05-1.25	0.86
Viscosity 50 ^{o}C (cP)	40-100	180
C (wt%)	55-65	83-86
O (wt%)	28-40	<1
S (wt%)	<0.05	<4

The most significant properties that distinguish bio-oil from petroleum are its high moisture content (15-30 wt%), high oxygen content (20-50 wt%), and low sulfur content (<0.05 wt%).[4,6] Bio-oil also possesses low heating value, chemical instability, poor volatility, high viscosity, and corrosiveness; all of which limit its potential to be substituted directly for petroleum-derived fuels.

The oxygen content in pyrolysis oil is in the form of heterocyclic rings, aromatic alcohols, hydroxy-carbonyl compounds, carboxylic acids, anhydrosugars, and larger fragments of lignocellulosic polymers (Fig. 1.3).[1] Many of these compounds are quite reactive, and cause bio-oil to be chemically unstable and prone to polymerization reactions, exacerbating the undesirable physical properties of the oil. Table 1.2 reports the relative abundance of different compound present in wood-derived bio-oil.[42]

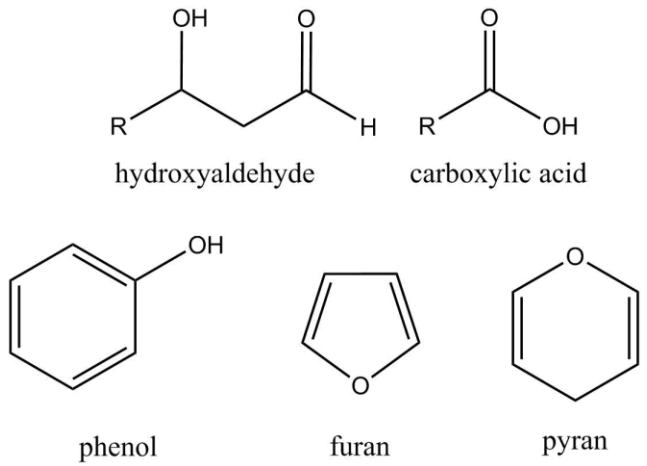

Figure 1.3: Example compounds present in bio-oil.

Table 1.2: Composition of wood-derived bio-oil.[10]

Compound	Relative abundance (wt%)
H_2O	22.0
Acids, Esters	20.2
Alcohols, Aldehydes	9.3
Ketones, Lactones	15.0
Furans	6.6
Pyrans	1.5
Phenols	23.5

The oxygenated functional groups present in bio-oil increase its acidity, with a pH range of 2.8-3.8 being reported in the literature,[2,6] and increase the polarity of many of the compounds in the oil, resulting in phase separation.[11,12] The low pH, high moisture content, and chemical instability also pose challenges in the storage and handling of bio-oil. The high oxygen content of bio-oil results

in many undesirable physical and chemical properties that make crude bio-oil unsuitable for use as a transportation fuel. While production of pyrolysis oil from biomass is relatively cheap and efficient, its chemical and physical properties present significant challenges that must be overcome before it can be utilized as a transportation fuel or used to supplement petroleum-based fuels. Oxygen removal is therefore critical in the production of fuel from bio-oil.

1.3 Hydrotreating

The process of removing heteroatoms (S, N, O, and metals) from fuel feedstocks with hydrogen is known as hydrotreating. In petroleum refinement, hydrotreating is primarily performed in order to remove sulfur and nitrogen impurities in processes referred to as hydrodesulfurization (HDS) and hydrodenitrogenation (HDN), respectively. In bio-oil refinement, the process of removing oxygen is referred to as hydrodeoxygenation (HDO). Hydrotreating processes involve two types of reactions: hydrogenation reactions, in which a pi bond reacts with H_2; and hydrogenolysis reactions, in which a sigma bond is cleaved by reaction with H_2. There are several reactions by which catalytic deoxygenation can occur; the three most common are hydrodeoxygenation (HDO), decarbonylation,

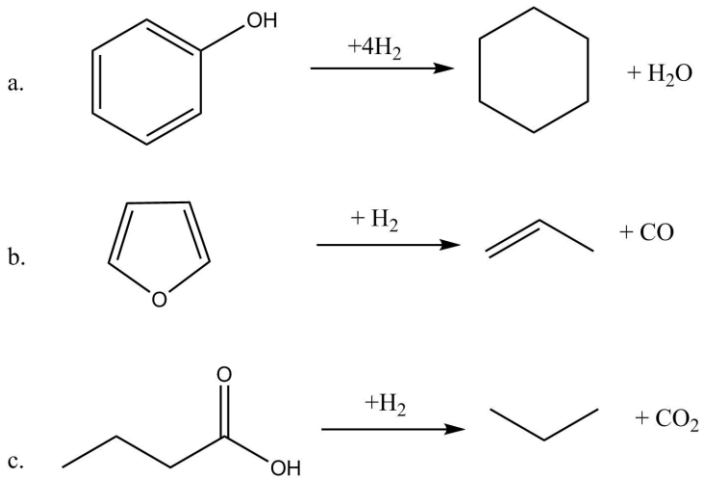

Figure 1.4 Catalytic deoxygenation pathways: a) hydrodeoxygenation, b) decarbonylation, c) decarboxylation.

and decarboxylation (Fig. 1.4). In hydrodeoxygenation (Fig. 1.4a), hydrogenolysis of C-O bonds leads to oxygen removal as water; this reaction yields the largest possible hydrocarbon fragment, preserving the energy density of the resulting fuel at the cost of consuming more hydrogen than other deoxygenation pathways. HDO pathways also tend to hydrogenate aromatics before HDO occurs, resulting in significant hydrogen consumption. Decarbonylation (Fig. 1.4b) and decarboxylation (Fig. 1.4c) pathways involve the removal of oxygen as carbon monoxide (CO) and carbon dioxide (CO_2), respectively. While these reactions tend to consume less hydrogen than HDO, they also produce fuel components with lower energy density. Additionally, the CO produced by decarbonylation can bond strongly to active catalytic sites, potentially poisoning the catalysts used for deoxygenation.

Due to the chemical and physical differences between bio-oil and petroleum, the reaction conditions and processes common in crude oil hydroprocessing cannot be easily carried over to bio-oil upgrading. For bio-oil processed at the temperatures necessary for deoxygenation to occur(573-673 K), the desired deoxygenation reactions (Fig. 1.4) are in competition with undesirable polymerization reactions.[13] These polymerization reactions produce high molecular weight compounds, resulting in greater deactivation of catalysts via coke deposition, and clogging of the reactor bed.[11,13,14] It is believed that the chemical instability of bio-oils is primarily due to the carbonyl content of the oil, and it has been shown that hydrogenation of carbonyls is an important step in the stabilization of bio-oil.[14] For this reason, bio-oil deoxygenation is typically performed in two steps: a mild hydrogenation step is first carried out at a low temperature (448-523 K) with the goal of hydrogenating carbonyl groups present in the bio-oil, followed by a high temperature hydrotreating step (523-673 K) in which desired deoxygenation reactions can occur (Fig. 1.5).[15]

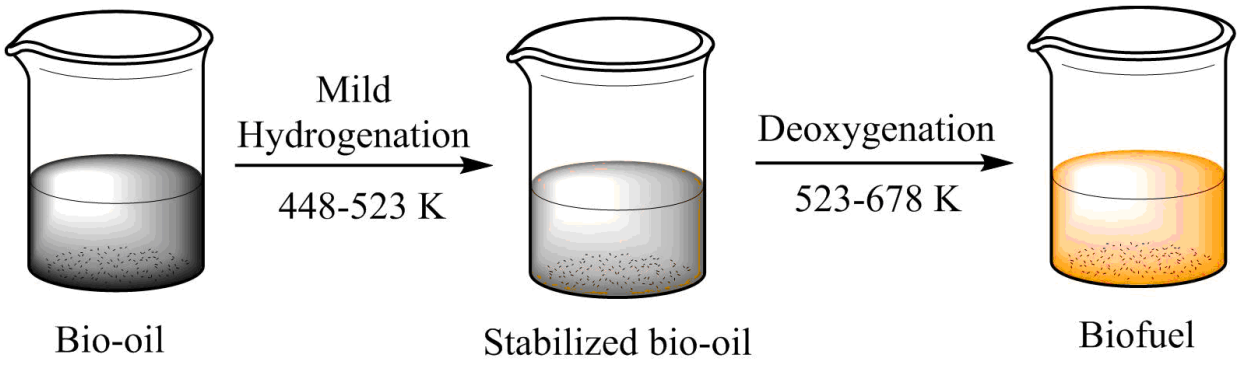

Figure 1.5: Common steps in the processing of bio-oil.

Elliott et al. studied the deoxygenation of pine-derived bio-oil in an attempt to develop process technology for converting pyrolysis oil into petroleum refinery feedstock.[11] A two-stage, fixed-bed flow reactor was used with the first stage of the reactor at a low temperature (343 K) to stabilize the feed, and the second stage of the reactor at a higher temperature (673 K) to deoxygenate the oil. A sulfided Ru/C catalyst was used in the low temperature stage as a hydrogenation catalyst, followed by a sulfided Co-Mo/C hydrotreating catalyst in the second, higher temperature stage. The sulfided catalysts were very active toward deoxygenation pathways, with the oxygen content reduced from 50 wt% to less than 1 wt% in most instances. There were several problems identified with the process, however, the first of which being the addition of a sulfiding reagent to the reactor feed in order to maintain catalyst stability. The addition of sulfur to bio-oil deprives the resulting biofuel of one of its advantages - low sulfur content; additionally, the second hydrotreating stage was observed to produce significant amounts of water, which is known to degrade alumina supports as well as oxidize molybdenum sulfide structures, resulting in lowered catalytic activity.[4,14]

Venderbosch et al. used a Ru/C catalyst in a variety of different reactor conditions in order to study the effects of different hydrotreating and hydrogenation steps in the processing of bio-oil.[14] Bio-oil was passed through four sequential reactors at varying temperatures, and the liquid effluent

was collected and analyzed. The study confirmed that polymerization and coke deposition compete with deoxygenation pathways under hydrotreating conditions, and showed that several hydrogenation steps at steadily increasing temperatures helped to stabilize the bio-oil, resulting in a greater amount of deoxygenation and less coke deposition. They also observed significant hydrogen consumption, and suggested that a high pressure thermal treatment step (HPTT) be used in which bio-oil is stabilized by placing it under high temperature and pressure conditions, followed by removal of the resultant aqueous product fraction may be a more desirable stabilization step than hydrogenation, as a significant amount of hydrogen consumption results from hydrogenation of products in the aqueous product fraction. While bio-oil studies give insight into the viability of different catalysts in deoxygenation processes, the chemical complexity of bio-oil makes it difficult to understand the mechanisms and kinetics by which deoxygenation occurs.

In order to design more effective catalysts for bio-oil upgrading, it is necessary to understand the kinetics and mechanisms by which oxygen-containing functional groups interact with and react on different catalysts. Many studies now focus on the deoxygenation of model compounds representing the different species present in bio-oil. Common model compounds include furans, carboxylic acids, and phenolics (such as guaiacol).[4,5,16] In this thesis research, furan and crotonaldehyde were used as model compounds (Fig. 1.6). Furan was used because furan derivatives are common in bio-oil, often constituting 5-7 wt% of bio-oils,[10] while crotonaldehyde was chosen because it allows for study of both deoxygenation and hydrogenation pathways.

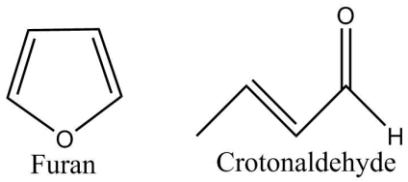

Figure 1.6: Model compounds for bio-oil used in this research.

Not only are carbonyl compounds prevalent in bio-oil, but as an unsaturated aldehyde, crotonaldehyde allows for investigation of selective hydrogenation properties of catalysts, which are of interest to many fine chemical industries.[17-22] Crotonaldehyde can also be used to probe low temperature hydrogenation, as the energy barrier for such reactions is lower than for aromatic compounds such as furan. The study of hydrogenation pathways is important for the investigation of different catalysts for use in the stabilization of bio-oil.

Many studies have attempted to determine the manner by which model compounds adsorb to surface sites on catalysts in order to probe and understand the reaction pathways. Badawi et al. used density functional theory (DFT), a computational chemistry technique, to model furan adsorption on a MoS_2 surface and found that furan adsorption was different from the adsorption of its sulfur analogue, thiophene. While thiophene was found to readily adsorb to a non-defective edge-sites, furan adsorption could only take place across Mo atoms exposed by edge defects.[23] Choe performed FTIR and TPD studies of the deoxygenation of furan on a sulfided Co-Mo/Al_2O_3 catalyst and proposed reaction mechanisms for the deoxygenation of furan at both low and high temperatures, as well as suggesting that furan adsorption occurred primarily via the oxygen atom in a "tilted on top" mode (Fig. 1.7).[24] These studies into the mechanisms of deoxygenation catalysis provide a deeper understanding of the reactivity of different catalysts, and allow for consideration of catalytic properties and selectivity in the development of catalysts for bio-oil refinement.

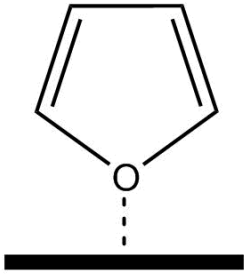

Figure 1.7: Proposed "tilted on top" adsorption mode of furan.[24]

1.4 Catalysis

Industrial scale hydrotreating and hydroprocessing reactions are performed using heterogeneous catalysts. Catalysts lower the activation energy associated with chemical reactions, allowing those reactions to occur at higher rates and lower temperatures than they would without a catalyst. While many catalysts are composed of expensive noble metals (i.e. Pt, Pd, Rh), they are not consumed by the reactions they catalyze, allowing for a large number of reactant turnovers to products to be carried out by a relatively small amount of catalyst. The activity of a catalyst describes its ability to catalyze a specific reaction, with more active catalysts being able to perform more reactions per unit time. Another important quality of a catalyst is its product selectivity. For a given molecule there may be many different reactions that can occur, and catalysts with different compositions and surface structures will often catalyze certain reaction pathways over others (Fig. 1.4). It is important, therefore, to choose a catalyst with a high activity and strong selectivity toward the desired product.

Most conventional hydrotreating catalysts are based on molybdenum sulfide (MoS_2).[11,15,25-27] These catalysts are effective for removing sulfur and nitrogen impurities; however, they possess a low active site density and require sulfur in the feed in order to remain in an active state. Bio-oils contain a much lower amount of sulfur (< 0.05 wt%) than petroleum oils (~1-4 wt%),[25,28] and the use of MoS_2-based catalysts requires sulfur additives in the feed, which would counteract the goal of low sulfur content in the fuel. Water and oxygenated compounds are also known to be highly detrimental to the stability of the sulfided Mo catalysts used in industrial hydrotreating.[26,27] The low concentration of sulfur and high concentration of water and oxygen in bio-oil makes the use of sulfided Mo catalysts in bio-oil processing unfeasible, and as such there is a need to develop hydrotreating catalysts which are more suitable for use in bio-oil processing. Several types of

catalysts are currently being investigated for their deoxygenation capabilities and potential for use in commercial scale bio-oil upgrading.

Noble metal catalysts (e.g. Pt, Pd, Ru) have shown a high degree of hydrotreating activity, their potential is limited due to high cost and deactivation under hydrotreating conditions caused either by poisoning of active sites with carbon monoxide and/or sulfur and coke deposition.[29] Nevertheless, noble metals have been observed to be effective hydroprocessing catalysts, and many have shown promise for use in hydrotreatment of pyrolysis oil. Wildschut et. al. reported that noble metal catalysts (Ru/C, Pt/C, Pd/C) exhibited a greater hydrocarbon yield and deoxygenation than sulfided Ni-Mo/Al_2O_3 and Co-Mo/Al_2O_3 catalysts, with Ru catalysts believed to be the most promising.[11] Li et al. studied the selective hydrogenation of crotonaldehyde over a Ru/ZnO catalyst, and found that using a $RuCl_3$ reagent in the impregnation synthesis of a Ru/ZnO increased the number of acidic sites on the surface of the ZnO support. The surface acidity of the support was shown to be related to both the activity of the Ru catalyst, as well as its selectivity towards the desired unsaturated alcohol product; however, high surface acidities were also shown to result in an increased rate of deactivation. The mechanism of deactivation was attributed to generation of CO via decarbonylation, resulting in catalyst poisoning, as well as the deposition of carbon onto the catalyst surface.[16] Yu et al. studied the activity and deactivation of bimetallic Ru-Ir/ZnO catalysts synthesized at varying reduction temperatures. This study also drew connections between surface acidity and catalytic performance, as well as attributing catalytic deactivation to carbon deposition and CO poisoning of catalytic surfaces. The use of a bimetallic system, in this case Ru-Ir/SiO_2, resulted in a lower susceptibility to poisoning than a monometallic Ru/SiO_2 catalyst, implying that some bimetallic systems may show improved resistance to deactivation relative to the constituent metal phases.[30]

Transition metal phosphides have been investigated for their potential as hydrotreating catalysts, as many metal phosphides have been shown to possess metallic properties, stability under hydrotreating conditions, and high catalytic activities.[25] Metal phosphide catalysts often exhibit favorable product selectivities and are useful in deoxygenation reactions, where the reaction conditions may not be practical for sulfide-based catalysts. Zhao et al. reported the guaiacol deoxygenation activities of several different metal phosphides supported on silica and compared them to the activities of commercial $CoMoS/Al_2O_3$ and Pd/Al_2O_3 catalysts.[16] The commercial $CoMoS/Al_2O_3$ catalyst was found to rapidly deactivate via coking due to the acidity of the guaiacol, while the Pd/Al_2O_3 catalyst possessed a higher initial activity than the metal phosphide catalysts. However, the Pd/Al_2O_3 catalyst produced only catechol, which is an undesirable product. A Ni_2P/SiO_2 catalyst was found to out-perform both catalysts, producing primarily the desired deoxygenation products, such as cresol and benzene.

Noble metal phosphides have also shown promise as hydrotreating catalysts, often showing greater stability than their noble metal counterparts. As well, each metal often has several different phosphide phases, between which there can be significant differences in catalytic activity and stability. Bowker et al. report the synthesis of Ru_2P/SiO_2, RuP/SiO_2, and Ru/SiO_2 catalysts, as well as the furan deoxygenation properties of each catalyst.[28] While both of the Ru phosphide phases were found to possess greater furan deoxygenation activities than the Ru/SiO_2 catalyst; the Ru_2P/SiO_2 catalyst in particular was shown to possess a much greater activity than the RuP/SiO_2 catalyst. The Ru phosphide catalysts also showed different product selectivities than Ru/SiO_2, selecting primarily for C_4H_y hydrocarbons via hydrodeoxygenation pathways while the Ru/SiO_2 catalyst primarily produced C_3H_y hydrocarbons via decarbonylation pathways. Bowker et al. also reported the synthesis and dibenzothiophene (DBT) desulfurization properties of Ru and Pd catalysts and several of their phosphide phases.[31] Some of the metal phosphide phases were found to degrade under

hydrotreating conditions; however, most of the metal phosphides studied retained their phase purity over the course of 60-72 h under DBT HDS conditions. Burns et al. studied the thiophene hydrodesulfurization properties of several Co_xP_y/SiO_2 catalysts prepared via impregnation with varying P/Co molar ratios.[32] The catalysts with the highest HDS activities were those prepared with a P/Co ratio of 0.5 and 1.5, containing phase-pure Co_2P and CoP, respectively. Both of these catalysts showed very little deactivation over 72 h under thiophene HDS conditions, while a sulfided Co/SiO_2 catalyst deactivated rapidly over the same time period under similar conditions. The CoP/SiO_2 catalyst was shown to be nearly four times as active as the Co_2P/SiO_2 catalyst.

Many bimetallic phosphides have been shown to be active hydrotreating catalysts, often possessing greater activities than their constituent monometallic phosphides, suggesting that interactions between different metals may have a positive effect on the catalytic properties of phosphides.[29] While the efficacy of bimetallic phosphides in deoxygenation reactions has not been extensively studied, there have been many studies that have reported promising HDS and HDN properties of several bimetallic phosphide compositions.[33-35] Several studies have also shown that varying the metal composition in bimetallic phosphides can have significant effects on the selectivity and activity of these catalysts. Some transition metal phosphide phases adopt similar crystalline structures (e.g. Ru_2P and Co_2P) and their bimetallic phosphides form solid solutions, in which one crystalline phase is present instead of two separate monometallic phosphide phases.[33] Abu et al. reported the synthesis and carbazole HDN activity of a series of Ni_xMoP/SiO_2 catalysts.[34] The bimetallic phosphide catalysts possessed lower turnover frequencies than a reference MoP/SiO_2 catalyst, however they showed higher carbazole conversions and a much higher selectivity towards the fully hydrogenated bicyclohexane product than MoP/SiO_2. Oyama et al. have reported the synthesis and 4,6-dimethyldibenzothiophene (4,6-DMDBT) HDS properties of silica-supported $Ni_{2-x}Fe_xP$ catalysts.[35] Using X-ray absorption fine structure analysis, they determined that the

phosphides were composed of Ni and Fe atoms distributed in the metal sites of the hexagonal Fe_2P structure, confirming that the bimetallic phosphide catalysts formed solid solutions instead of a biphasic mixture of two metal phosphides. Several of the $Ni_{2-x}Fe_xP/SiO_2$ catalysts possessed higher 4,6-DMDBT conversions than the sulfided Mo-based catalysts, and selected for desulfurization via the direct desulfurization pathway (DDS), while HDS over commercial catalysts such as sulfided Co-Mo or Ni-Mo typically proceeds via a hydrogenation route (HYD) where the 4,6-DMDBT is partially hydrogenated prior to desulfurization.[35]

1.5 Thesis Goals

The purpose of this thesis research is to investigate the properties of several bimetallic phosphide catalysts containing noble (e.g. Ru, Rh) and earth-abundant (e.g. Co) metals in the deoxygenation of model compounds representing several major functional groups present in bio-oil. Series of silica-supported $Co_xRu_{2-x}P$ and $Co_xRh_{2-x}P$ catalysts were prepared with varying metal composition ($0 \leq x \leq 2$). The furan deoxygenation properties of the $Co_xRu_{2-x}P/SiO_2$ catalysts were investigated, and trends between composition and catalytic activity were studied. The crotonaldehyde conversion properties of the $Co_xRu_{2-x}P/SiO_2$ and $Co_xRh_{2-x}P/SiO_2$ catalysts were investigated for both deoxygenation and selective hydrogenation activity, and trends between catalyst composition, activity and selectivity were investigated. Following catalytic measurements, the crystalline structure was analyzed via XRD, and carbon and sulfur analysis was carried out to determine the degree of coking on the surface of the catalysts. All catalysts were characterized via X-ray diffraction (XRD), energy-dispersive X-ray diffraction (EDX), X-ray photoelectron spectroscopy (XPS), BET surface area analysis, and CO chemisorption.

2. Experimental Methods

2.1 Catalyst Preparation

All reagents were used as received with the exception of fumed silica (Cabot, Carb-O-Sil, EH-5, 200 m^2/g, 99.9%), which was calcined in air at 773 K for 3 h. Calcined silica was stored in an oven at 393 K prior to use. All gases used in synthesis and characterization were ultra-high purity (UHP) and were purified before use with molecular sieve (Alltech) and oxygen purification (Alltech, Oxy-Clear) traps to remove trace oxygen, water, and particulate matter.

2.1.1 Temperature Programmed Reduction

Catalyst precursors were reduced to metal phosphides following impregnation and drying, then passivated so that they could be handled in air. The dried precursors were reduced via a temperature programmed reduction (TPR) process (Fig. 2.1). A sample of catalyst precursor (~0.25 g) was placed in a quartz U-tube on top of a quartz wool plug. The tube was purged with UHP He (60 ml/min) for 30 min, and a ceramic fiber furnace was placed around the tube. Hydrogen (100 mL/min) was flowed over the precursor as it was heated at 5 K/min to a final temperature of 773 K, where it was held under flowing H_2 for 1 h. The quartz U-tube was then cooled to room temperature and purged with He for 30 min, after which it was passivated with a mixture of 1 mol% O_2/He for 2 h. The passivation process formed a thin oxide layer on the surface of the metal phosphide nanoparticles, allowing the catalysts to be handled in air; the passivation layer was removed from the catalyst via H_2 reduction prior to use in catalytic reactor or characterization measurements.

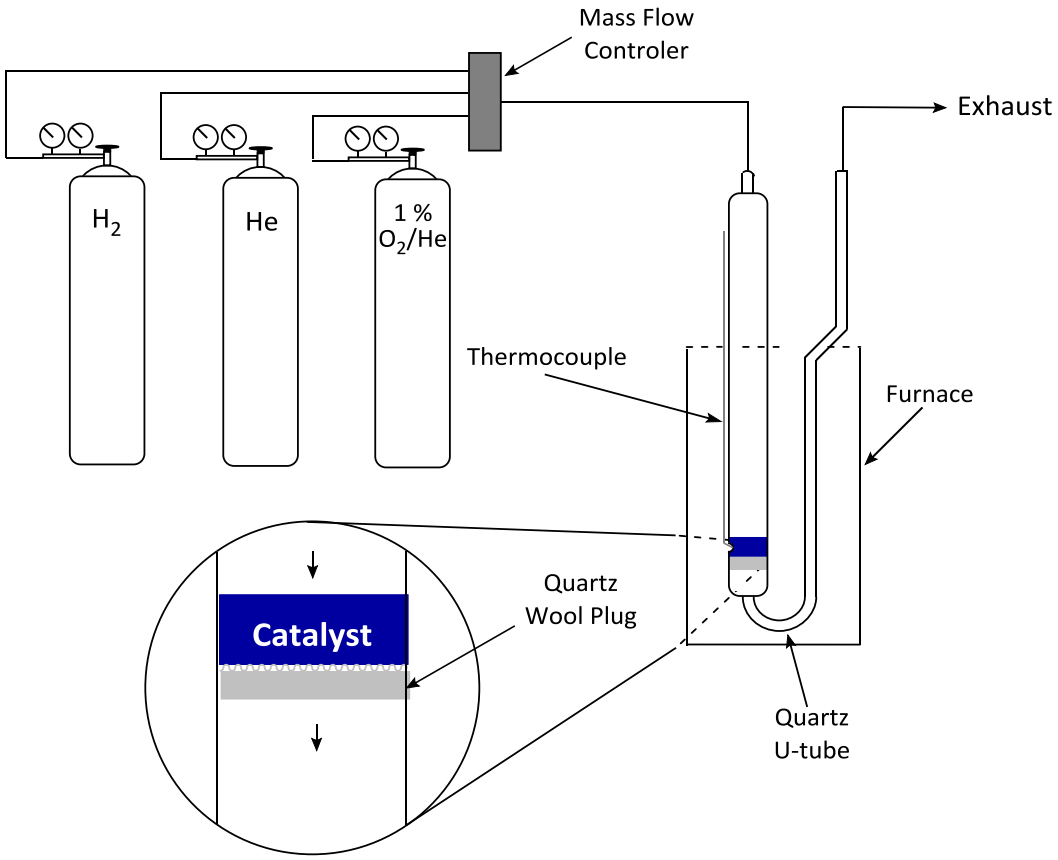

Figure 2.1: Schematic of temperature-programmed reduction apparatus.

2.1.2 Synthesis of Metal Catalysts

Ru Precursor Synthesis

A Ru/SiO_2 precursor was prepared such as to have a final Ru loading of 13.3% by weight (Fig. 2.2), such that it contained the same amount of Ru as a 15 wt% Ru_2P/SiO_2 catalyst.

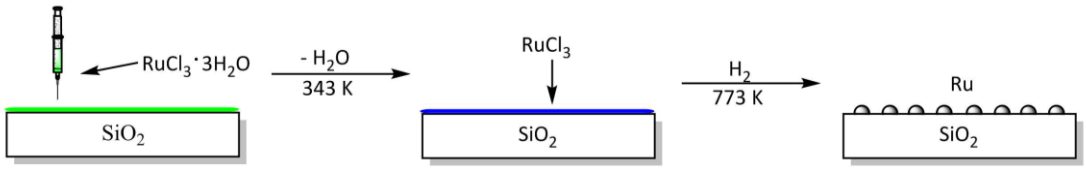

Figure 2.2: Process for Ru/SiO_2 catalyst synthesis.

Ruthenium (III) chloride trihydrate ($RuCl_3 \bullet 3H_2O$, 0.9131 g, Pressure Chemical Co.) was dissolved in 5 mL nanopure water (dark brown solution) and then impregnated dropwise onto silica (~2.0 g) until incipient wetness, at which point it was dried at 393 K before further impregnation was carried out. This process was repeated until the entire solution was impregnated onto the silica support. The precursor was reduced to a Ru/SiO_2 catalyst at 650 K under flowing hydrogen prior to catalytic study or characterization.

Co Precursor Synthesis

A Co/SiO_2 precursor was prepared such as to have a final Co loading of 11.9% by weight, such that it contained the same amount of Co as a 15 wt% Co_2P/SiO_2 catalyst. Cobalt(II) nitrate hexahydrate ($Co(NO_3)_2 \bullet 6H_2O$, 1.3803 g, Alpha Aesar) was dissolved in 5 mL nanopure water (clear red solution), then impregnated dropwise onto silica (~2.0 g) until incipient wetness, at which point it was dried at 393 K before further impregnation was carried out. This process was repeated until the entire solution was impregnated onto the silica support. The precursor was reduced to a Co/SiO_2 catalyst at 650 K under flowing hydrogen prior to catalytic study or characterization.

2.1.3 Synthesis of Metal Phosphide Catalysts

Ru_2P/SiO_2 Synthesis

A Ru_2P/SiO_2 catalyst (15 wt% Ru_2P) was prepared as follows. Hypophosphorous acid (H_3PO_2, 0.2878 g, 50 wt% in H_2O, Sigma Aldrich) was dissolved in 5 mL nanopure water (clear and colorless solution). Ruthenium (III) chloride trihydrate (0.7917 g, Pressure Chemical Co.) was added to the hypophosphorous acid solution (dark brown solution), then impregnated dropwise onto silica (~2.0 g) until incipient wetness, at which point it was dried at 343 K before further impregnation was carried out. This process was repeated until the entire solution was impregnated onto the silica

support. The dried precursor was then placed on a quartz wool plug in a quartz u-tube, where it was purged under flowing He (30 ml/min) for 30 min. The sample was then reduced via a TPR process in which it was heated to 773 K at a ramp rate of 5 K/min under flowing H_2 (60 ml/min), then held at 773 K for 1 h under flowing H_2 (60 ml/min). The sample was allowed to cool, then purged under flowing He (30 ml/min) for 30 min, after which it was passivated under a flowing mixture of 1% O_2/He for 2 h to yield the Ru_2P/SiO_2 catalyst.

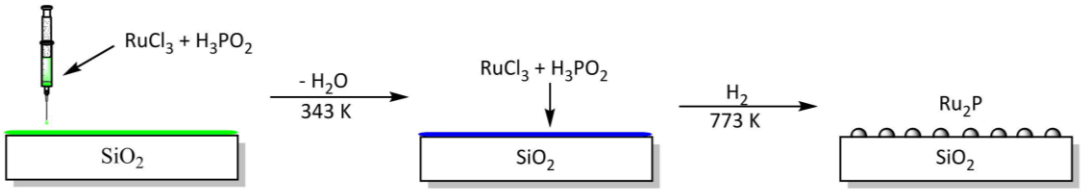

Figure 2.3: Process for Ru_2P/SiO_2 catalyst synthesis.

Rh_2P/SiO_2 Synthesis

A Rh_2P/SiO_2 catalyst (15 wt% Rh_2P) was prepared as follows. Hypophosphorous acid (0.1417 g, 50 wt% in H_2O, Sigma Aldrich) was dissolved in 5 mL nanopure water (clear and colorless solution). Rhodium (III) chloride hydrate ($RhCl_3 \bullet 2.66H_2O$, 0.3834 g, Pressure Chemical Co.) was added to the hypophosphorous acid solution to give a dark red solution, which was then impregnated dropwise onto silica (~1.0 g) until incipient wetness, at which point it was dried at 343 K before further impregnation was carried out. This process was repeated until the entire solution was impregnated onto the silica support. The dried precursor was then reduced via TPR (773 K) and passivated under 1 mol% O_2/He to yield the Rh_2P/SiO_2 catalyst as described previously.

Co_2P/SiO_2 Synthesis

A Co_2P/SiO_2 catalyst (15 wt% Co_2P) was prepared as follows. Hypophosphorous acid (0.2878 g, 50 wt% in H_2O, Sigma Aldrich) was dissolved in 5 mL nanopure water (clear and colorless

solution). Cobalt(II) nitrate hexahydrate (1.3803 g, Alfa Aesar, 98-102%) was added to the hypophosphorous acid solution (clear red solution), which was then impregnated dropwise onto silica (~2.0 g) until incipient wetness, at which point it was dried at 343 K before further impregnation was carried out. This process was repeated until the entire solution was impregnated onto the silica support. The dried precursor was then reduced via TPR (773 K) and passivated under 1 mol% O_2/He to yield the Co_2P/SiO_2 catalyst as described previously.

2.1.4 Synthesis of Bimetallic Phosphide Catalysts

$Co_xRu_{1-x}P/SiO_2$ Synthesis

A series of silica supported $Co_xRu_{2-x}P$ precursors was prepared as follows such that the final loading of $Co_xRu_{2-x}P$ was 15 wt% on silica (Table 2.1 and Fig. 2.4).

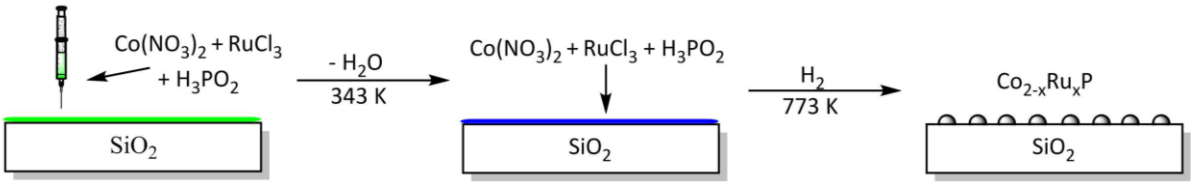

Figure 2.4: Process for $Co_xRu_{2-x}P/SiO_2$ catalyst synthesis.

Table 2.1: Reagent masses for 15 wt% $Co_xRu_{2-x}P/SiO_2$ catalysts.

Nominal Composition	$Co(NO_3)_3{\cdot}6H_2O$	$RuCl_3{\cdot}3H_2O$	H_3PO_2 (50 wt% in H_2O)	SiO_2
$Co_{0.25}Ru_{1.75}P$	0.1154 g	0.7256 g	0.3014 g	2.0 g
$Co_{0.5}Ru_{1.5}P$	0.2422 g	0.6528 g	0.3164 g	2.0 g
$Co_{0.75}Ru_{1.25}P$	0.3823 g	0.5724 g	0.3329 g	2.0 g
Co_1Ru_1P	0.5379 g	0.4832 g	0.3513 g	2.0 g
$Co_{1.25}Ru_{0.75}P$	0.7116 g	0.3836 g	0.3718 g	2.0 g
$Co_{1.5}Ru_{0.5}P$	0.9069 g	0.2716 g	0.3948 g	2.0 g
$Co_{1.75}Ru_{0.25}P$	1.1279 g	0.1448 g	0.4209 g	2.0 g

Hypophosphorous acid (50 wt% solution) was dissolved in 5 mL nanopure water (clear and colorless solution). Ruthenium(III) chloride trihydrate (Pressure Chemical Co.), and cobalt(II) nitrate hexahydrate (Alfa Aesar, 98-102%) were added to the hypophosphorous acid solution to give a dark brown solution. The solution was then impregnated dropwise onto silica (~2.0 g) until incipient wetness, at which point it was dried at 343 K before further impregnation was carried out. This process was repeated until the entire solution was impregnated onto the silica support. The dried precursor was then reduced via TPR (773 K) and passivated under 1 mol% O_2/He to yield the $Co_xRu_{2-x}P/SiO_2$ catalyst as described previously.

High loading $Co_xRu_{1-x}P/SiO_2$ Synthesis

A series of silica supported $Co_xRu_{2-x}P$ precursors was prepared as follows such that the final loading of $Co_xRu_{2-x}P$ was 25 wt% on silica (Table 2.2).

Table 2.2: Reagent masses for 25 wt% $Co_xRu_{2-x}P/SiO_2$ catalysts.

Nominal Composition	$Co(NO_3)_3 \cdot 6H_2O$	$Ru(Cl_3) \cdot 3H_2O$	H_3PO_2 (50 wt% in H_2O)	SiO_2
$Co_{0.25}Ru_{1.75}P$	0.1090 g	0.6853 g	0.2846 g	1.0 g
$Co_{0.5}Ru_{1.5}P$	0.2288 g	0.6165 g	0.2988 g	1.0 g
$Co_{0.75}Ru_{1.25}P$	0.3611 g	0.5406 g	0.3144 g	1.0 g
Co_1Ru_1P	0.5080 g	0.4564 g	0.3318 g	1.0 g
$Co_{1.25}Ru_{0.75}P$	0.6721 g	0.3623 g	0.3511 g	1.0 g
$Co_{1.5}Ru_{0.5}P$	0.8565 g	0.2565 g	0.3729 g	1.0 g
$Co_{1.75}Ru_{0.25}P$	1.0653 g	0.1367 g	0.3975 g	1.0 g

Hypophosphorous acid (50 wt% solution) was dissolved in 5 mL nanopure water (clear and colorless solution). Ruthenium(III) chloride trihydrate (Pressure Chemical Co.), and cobalt(II) nitrate hexahydrate (Alfa Aesar, 98-102%) were added to the hypophosphorous acid solution to give a dark brown solution. The solution was then impregnated dropwise onto silica (~1.0 g) until incipient wetness, at which point it was dried at 343 K before further impregnation was carried out. This

process was repeated until the entire solution was impregnated onto the silica support. The dried precursor was then reduced via TPR (773 K) and passivated under 1 mol% O_2/He to yield the $Co_xRu_{2-x}P/SiO_2$ catalyst as described previously.

$Co_xRh_{1-x}P$ Series Synthesis

A series of silica-supported $Co_xRh_{1-x}P$ precursors was prepared such that the final loading of $Co_xRh_{2-x}P$ was 15 wt% on silica (Table 2.3). Hypophosphorous acid (50 wt% in H_2O) was dissolved in 5 mL nanopure water (clear and colorless solution). Rhodium(III) chloride hydrate (Pressure Chemical Co.), and cobalt(II) nitrate hexahydrate (Alfa Aesar, 98-102%) were added to the hypophosphorous acid solution to form a dark red solution. The solution was then impregnated dropwise onto silica (~1.0 g) until incipient wetness, at which point it was dried at 343 K before further impregnation was carried out. This process was repeated until the entire solution had been impregnated onto the silica support. The dried precursor was then reduced via TPR (773 K under flowing hydrogen) and passivated under 1 mol% O_2/He to yield the $Co_xRh_{2-x}P/SiO_2$ catalyst as described previously.

Table 2.3: Reagent masses for $Co_xRh_{2-x}P/SiO_2$ catalysts.

Nominal Composition	**$Co(NO_3)_3{\cdot}6H_2O$**	**$Rh(Cl_3)\cdot2.66H_2O$**	**H_3PO_2 (50 wt% in H_2O)**	**SiO_2**
$Co_{0.25}Rh_{1.75}P$	0.0569 g	0.3519 g	0.1486 g	1.0 g
$Co_{0.5}Rh_{1.5}P$	0.1196 g	0.3170 g	0.1562 g	1.0 g
$Co_{0.75}Rh_{1.25}P$	0.1890 g	0.2784 g	0.1646 g	1.0 g
Co_1Rh_1P	0.2664 g	0.2354 g	0.1740 g	1.0 g
$Co_{1.25}Rh_{0.75}P$	0.3531 g	0.1873 g	0.1844 g	1.0 g
$Co_{1.5}Rh_{0.5}P$	0.4510 g	0.1329 g	0.1964 g	1.0 g
$Co_{1.75}Rh_{0.25}P$	0.5624 g	0.0710 g	0.2099 g	1.0 g

2.2 X-Ray Diffraction

X-Ray diffraction (XRD) patterns were acquired of the Co/SiO_2 and Ru/SiO_2 catalysts as well as the $Co_xRu_{2-x}P/SiO_2$ and $Co_xRh_{2-x}P/SiO_2$ catalysts using a PANalytical X'Pert Pro MRD X-ray diffractometer. The diffractometer used monochromatized x-rays (λ=1.5418 Å), and was operated at a voltage of 45 kV and a current of 40 mA. Powdered samples were mounted to glass microscope slides by depositing ~50 mg of catalyst onto the slide; methanol was then added to the powder to form a paste. A metal spatula was used to shape the paste into a 2 cm diameter circle on the slide. Once the methanol had evaporated, the slide was mounted into the instrument for analysis. Diffraction patterns were acquired using X'Pert Data Collector software over a Bragg angle (2θ) range of 20-80°. Reference XRD patterns were taken from the JCPDS powder diffraction file database.[36] Experimental and reference diffraction patterns were used to analyze phase purity.

The average size of the metal or metal phosphide crystallites in the prepared and tested catalysts was calculated using the Scherrer equation (Equation 2.1), which relates peak broadening in an XRD pattern to the average size of crystallites within the sample being analyzed.[37]

$$D_C = \frac{K\lambda}{\beta cos\theta} \tag{2.1}$$

The shape factor, K, is equal to 1, as spherical particles were assumed. The incident wavelength, λ, was 1.5418 Å. The peak broadening, β, is equal to the full width at half maximum (FWHM) of the peak analyzed, and θ is equal to the Bragg angle of the peak.

2.3 Energy-Dispersive X-ray Spectroscopy

Scanning electron microscopy energy dispersive X-ray spectroscopy (SEM-EDX) was used to determine the elemental composition of the prepared catalysts. A Vega TS 5136MM scanning electron microscope outfitted with an EDAX energy dispersive X-ray analysis system and a retractable backscatter detector (BSE). Analysis was performed with a 15 kV electron beam. Catalysts were prepared for analysis by loading ~50 mg of catalyst into a pellet die, where it was then compressed under a pressure of 10,000 psi; the resulting wafer was then mounted to an SEM sample standoff using a piece of double-sided carbon tape. Prior to analysis, samples were sputter-coated for 1 min with a mixture of Pd and Au, in order to ensure sample conductivity. EDX spectra were acquired by averaging elemental compositions across three sampling areas on each pellet. Elemental compositions were normalized to the mol% P and could then be calculated from the mol% reported for each element.

2.4 CO Chemisorption

CO chemisorption measurements were used to estimate the concentration of active sites in the catalysts. All chemisorption measurements were carried out on a Micromeritics Autochem 2950 HP instrument running software provided by Micromeritics. Chemisorption analysis was carried out as follows, 50 mg of the passivated catalyst was placed in a sample tube that was then attached to the Micromeritics Autochem 2950 HP system, and a furnace was enclosed around it. The sample was degassed at 333 K for 1 h under argon flow (60 mL/min), then the passivating oxide layer was removed from the catalyst via a TPR procedure in which the sample was heated to 673 K at 10 K/min under flowing hydrogen (60 mL/min), then held at that temperature for 1 h under flowing hydrogen (60 mL/min). The sample was then purged with helium and cooled to 273 K using liquid nitrogen.

The sample was then pulsed with 1 mL pulses of a 10 mol% CO/He gas mixture, with a thermal conductivity detector (TCD) measuring the amount of CO leaving the sample tube. CO pulses were stopped after successive peaks ceased to show increases in area, indicating that the catalyst sample had become fully saturated with CO. A temperature programmed desorption (TPD) process was then run on the sample under flowing helium to desorb CO from the sample. Following chemisorption, the sample tube was removed and weighed again to give a final sample mass. This sample mass was used to determine the CO chemisorption capacity in units of μmol CO/g catalyst.

2.5 BET Surface Area

Single-point Brunauer-Emmett-Teller (BET) surface areas were obtained using a Micromeritics Pulse Chemisorb 2700 instrument. Approximately 0.10 g sample was placed into a quartz sample tube which was then attached to the Pulse Chemisorb 2700 and purged with He (16 mL/min) for 30 min in order to degas the sample. Following degas, the samples were then reduced. A typical reduction began by heating the sample under flowing H_2 (20 mL/min) to 673 K over the course of 1 h, the sample was then held at 673 K for 2 h before a second degas was carried out in which the sample was purged in He for 1 h at 673 K. The sample was then cooled to room temperature. A three-point calibration of the Pulse Chemisorb 2700 was performed by injecting set volumes (0.2, 0.6, 1.0 mL) of N_2 drawn from the headspace of a liquid nitrogen dewar. A linear calibration curve could then be fitted to the three points generated, determining the relationship between N_2 volume detected and the response observed from the detector. A dewar of liquid N_2 was then used to cool the sample to 77 K while a 35 mL/min flow of 28.6 % N_2/He was passed over the sample. As N_2 physisorbed onto the surface of the sample, the deficit of N_2 in the gas flow was measured by the Pulse Chemisorb 2700. Once N_2 adsorption was complete and the detector had

equilibrated, the liquid N_2 bath was removed and replaced by a bath of room temperature water, and the desorption of N_2 from the sample was then measured.

BET theory is an adaptation of Langmuir theory, a model for monolayer molecular adsorption, which is used to instead describe multilayer molecular adsorption.[38] Three key assumptions are made in BET theory; it is assumed that molecules adsorb onto the surface of a sample in infinite layers, that there is no interaction between each adsorption layer, and finally that Langmuir theory can be applied to each layer. The assumptions made in BET theory result in the general form of the BET equation (equation 2.2), where c is the BET constant, V_m is the monolayer adsorbed gas volume, V is the volume of adsorbed gas, and P and P_0 are the equilibrium and saturation pressures of the adsorbed gas, respectively.

$$\frac{1}{V_a[\left(\frac{P_0}{P}\right)-1]} = \frac{c-1}{V_m c}\left(\frac{P}{P_0}\right) + \frac{1}{V_m c} \tag{2.2}$$

The volume of gas adsorbed to a surface is measured at several relative pressures (p/p_0), allowing for calculation of both the BET constant and the volume of the adsorbed monolayer. In single-point BET surface area calculations, a simplified formula is used in which the volume of gas adsorbed (V_a) is measured at a single relative pressure (P/P_0) as opposed to measuring it at multiple relative pressures, where relative pressure is the ratio of the partial pressure of the gas being adsorbed, and P_0 is its saturation pressure. V_a is calculated directly from a calibrated detector's response to N_2 gas desorbing from a sample's surface, after which point the volume of an apparent monolayer (V_m) is calculated (equation 2.3). The specific surface area of the sample (equation 2.4) can then be calculated using V_m, Avogadro's number (N_a), the mass of the sample (m), and the molar volume of a gas at STP (V_{molar}).

$$V_m = V_a\left(1 - \frac{P}{P_0}\right) \quad (2.3)$$

$$SA = \frac{V_m N_a}{m V_{molar}} \quad (2.4)$$

2.6 X-Ray Photoelectron Spectroscopy

X-ray photoelectron spectroscopy (XPS) was performed using a Surface Physics M-Probe ESCA spectrometer equipped with a monochromatic Al K_α anode and using a takeoff angle of 55°. Approximately 0.05 g of catalyst was pressed into a circular pellet at 10,000 psi using a pellet die, the pellet was then secured to a copper plate using double-sided tape and placed in an ultra-high vacuum chamber. Spectra were collected at pressures between 1.0-5.0x10^{-9} torr; with survey scans being performed with a pass energy of 166.5 eV using an ovular 2.2 x 2.0 mm spot and high resolution scans using a pass energy of 5.1 eV and a circular spot 250 µm in diameter. High resolution scans were acquired in the Co $2p_{3/2}$, Ru $3d_{5/2}$, Rh $3d_{5/2}$, and P 2p regions. A flood gun was used to correct for sample charging. Spectra were corrected to the carbon 1s peak at 284.6 eV for the $Co_xRh_{2-x}P/SiO_2$ catalysts and to the Si 2p peak at 103.5 eV for the $Co_xRu_{2-x}P/SiO_2$. Spectra were analyzed using CASA XPS software.

2.7 Carbon and Sulfur Analysis

A LECO SC-144DR Sulfur and Carbon Analyzer was used to quantify the sulfur and carbon content on catalysts following deoxygenation. Approximately 0.05 g of sample was placed in a ceramic crucible; the sample was then combusted at 1625 K for 3 min. Oxidized carbon (CO_2) and sulfur (SO_2) products generated from the catalyst sample were quantified via IR spectroscopy, allowing for determination of the wt% of both C and S.

2.8 Catalytic Activity Measurements

Catalytic deoxygenation measurements were carried out using an atmospheric flow reactor shown in Figure 2.5.

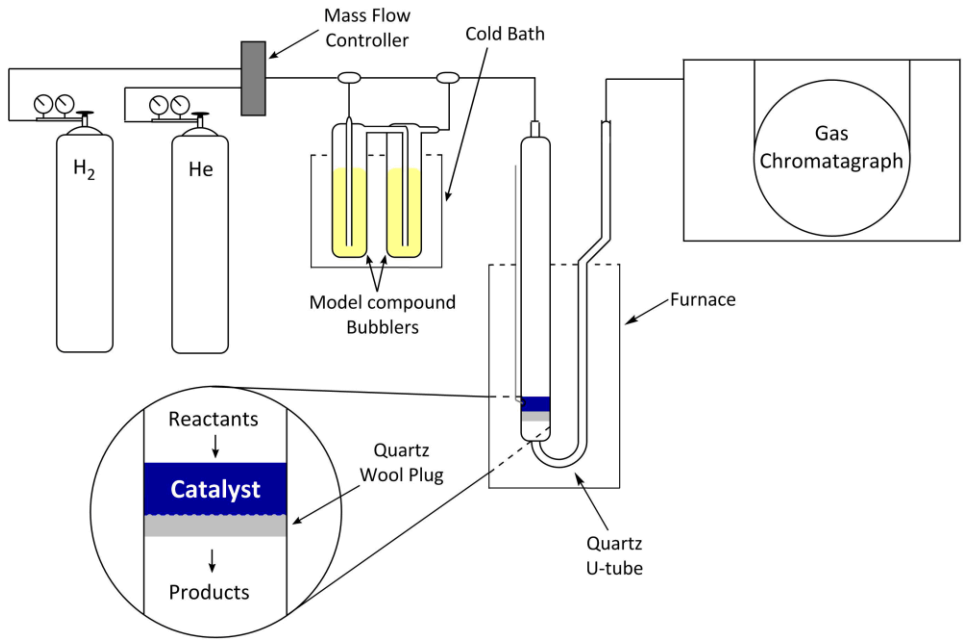

Figure 2.5: Schematic of deoxygenation flow reactor system.

A quartz wool plug was placed at the bottom of a quartz u-tube, and the catalyst sample (0.1000 g) was deposited on the plug. The u-tube was then placed inside of a ceramic furnace and attached to the flow reactor. Glass bubblers filled with the oxygenated compound being analyzed (furan or crotonaldehyde) were cooled via a recirculating refrigeration bath (Thermo Haake, C30-P) filled with antifreeze (NAPA). Bath temperatures were set to 250 K for furan studies and 273 K for crotonaldehyde studies. Gas flows were controlled by a mass flow controller (MKS Instruments, type 1159B), while the sample temperature was controlled using a ceramic fiber furnace (Watlow) attached to a microprocessor temperature controller (Omega, Type CN-2011K) and monitored by a Type K thermocouple mounted externally to the u-tube. During activity measurements, the reactor

effluent was analyzed by an on-line HP-5890 series II gas chromatograph (GC) equipped with a pneumatic sampling valve.

For furan deoxygenation measurements, the GC was fitted with parallel columns and detectors (Figure 2.6); an alumina column (Agilent, GS-alumina) attached to a flame ionization detector (FID) allowed for separation and quantification of hydrocarbons in the reactor effluent, while a carbon column (Agilent, GS-CarbonPlot) attached to a thermal conductivity detector (TCD), allowed for separation and quantification of permanent gases (CO, CO_2) in the reactor effluent.

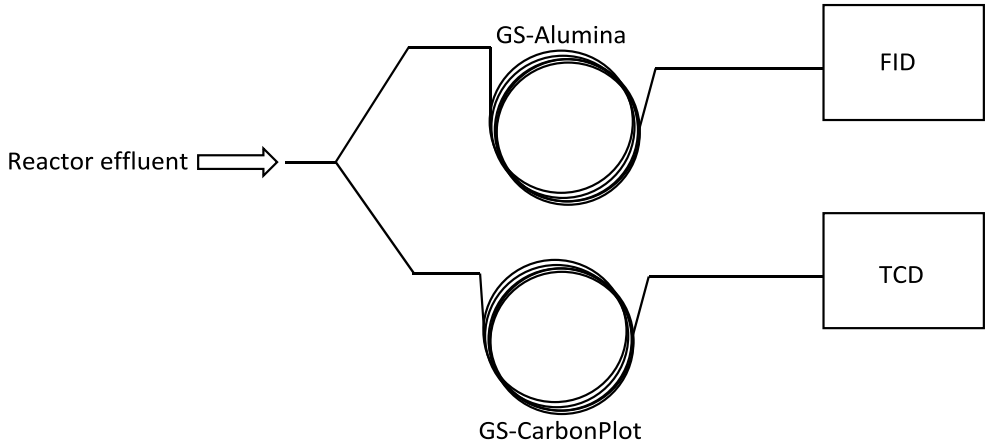

Figure 2.6: GC column set-up for furan deoxygenation studies.

For crotonaldehyde deoxygenation measurements, a single column was used from which the effluent was split to two parallel detectors (Figure 2.7). A bonded polystyrene-divinylbenzene column (Agilent, Plot-Q) was used to separate the effluent compounds, following which the column was split to TCD and FID detectors that quantified the permanent gases and hydrocarbons, respectively.

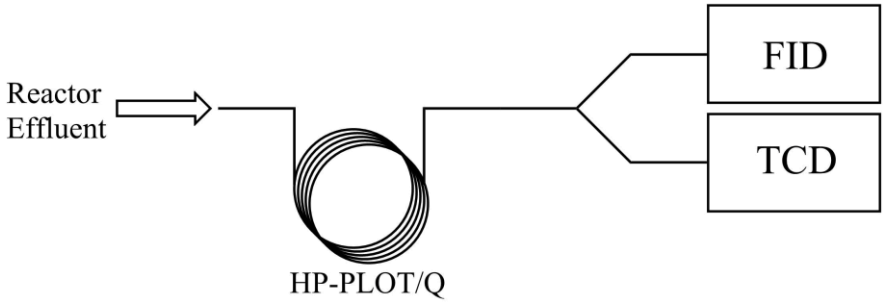

Figure 2.7: GC column set-up for crotonaldehyde deoxygenation studies.

Deoxygenation product concentrations were calculated using single-point response factors for each major product formed. Response factors for hydrocarbon products were determined by flowing calibration gases containing known concentrations of the products through the GC. Calibration gas mixtures were purchased from Scotty Specialty Gases and provided by Air Liquide (Table 2.4).

Table 2.4: Standardized gas mixtures (Air Liquide).

Compound(s)	Concentration	Balance
N-butane	1%	N_2
Cis-2-butene	1%	N_2
Propane	1%	N_2
Trans-2-butene	1%	N_2
Propylene	1003 ppm	N_2
1-butene	1002 ppm	N_2
Methane; ethane; propane; n-pentane; n-butane; n-propane; n-propane	1010-1020 ppm	N_2
n-butane; 1-butene; cis-2-butene; ethyl acetylene; isobutene; isobutylene; trans-2-butene; 1,3-butadiene	15 ppm	N_2
Acetylene; n-butane; ethane; ethylene; methane; methyl acetylene; propane; propylene	15 ppm	N_2

Response factors for products of crotonaldehyde hydrogenation and deoxygenation (butanol, crotyl alcohol, butyraldehyde) were obtained by direct injections of a series of solutions of known concentrations in methanol (Fischer, HPLC grade, 99.9%) for each compound. Each calibration standard was measured in triplicate, and integrated peak areas and the concentrations of the standards were used to calculate response factors for each product analyzed. The retention times and calculated response factors for expected products are reported in table 2.5.

Table 2.5: Retention times and response factors for expected crotonaldehyde deoxygenation products in a plot/Q column.

Compound	Retention Time (min)	Response Factor (ppm/count)
Methane	2.3	0.015625
Ethylene	3.6	0.007407
Acetylene	3.9	0.005917
Ethane	4.2	0.006897
Propylene	8.1	0.004237
Propane	8.5	0.004115
Propyne	9.0	0.004484
Butyne	12.2	0.003448
Isobutene	12.6	0.003953
1-butene	12.6	0.002907
Butane	12.8	0.003279
Trans-butene	13.1	0.003289
Cis-butene	13.3	0.003311
Butyraldehyde	19.1	0.00243
Crotonaldehyde	20.8	0.0035
Crotonol	22.3	0.00243
Butanol	22.5	0.002591

2.8.1 Deoxygenation measurements

Furan deoxygenation measurements were carried out at a reaction temperature of 573 K for 48 h for the $Co_xRu_{2-x}P/SiO_2$ catalysts. 0.1 g of catalyst was first placed in a quartz u-tube, the sample was purged with He (15 mL/min) for 30 min, following which the sample was then subjected to a

TPR process to remove the passivation layer present on the metal phosphide catalysts, and to reduce Ru/SiO_2 precursors to the metallic state. The sample was heated to 650 K under flowing H_2 (50 mL/min) over 1 h and held at 650 K for 2 h, following which it was then cooled to 573 K. The hydrogen gas feed was then redirected through the chilled, furan-filled bubblers (250 K), resulting in an 8.2 mol% mixture of furan/H_2 being passed over the catalyst. The reactor effluent was analyzed each hour for 48 h by the on-line HP5890 series II Gas chromatograph using parallel columns and detectors in order to measure the furan deoxygenation activity and selectivity as a function of time on-stream. A typical FID plot for furan deoxygenation testing is shown in figure 2.8, with peaks listed in table 2.6.

Table 2.6: Peak assignments for the GC trace plotted in Fig. 2.8.

Peak	Assignment	Retention Time (min)	Column
1	Methane	1.3	GS-CarbonPLOT
2	Ethane	1.6	GS-CarbonPLOT
3	Propane	3.8	GS-CarbonPLOT
4	Propylene/butane	10.5	GS-CarbonPLOT
5	Trans-2-butene	14.9	GS-CarbonPLOT
6	1-butene	15.2	GS-CarbonPLOT
7	Cis-2-butene	15.7	GS-CarbonPLOT
8	Isobutylene	15.8	GS-CarbonPLOT
9	Furan	23.3	GS-CarbonPLOT
10	CO	1.4	GS-Alumina
11	propylene	16.3	GS-Alumina
12	butane	17.2	GS-Alumina
13	furan	28.7	GS-Alumina

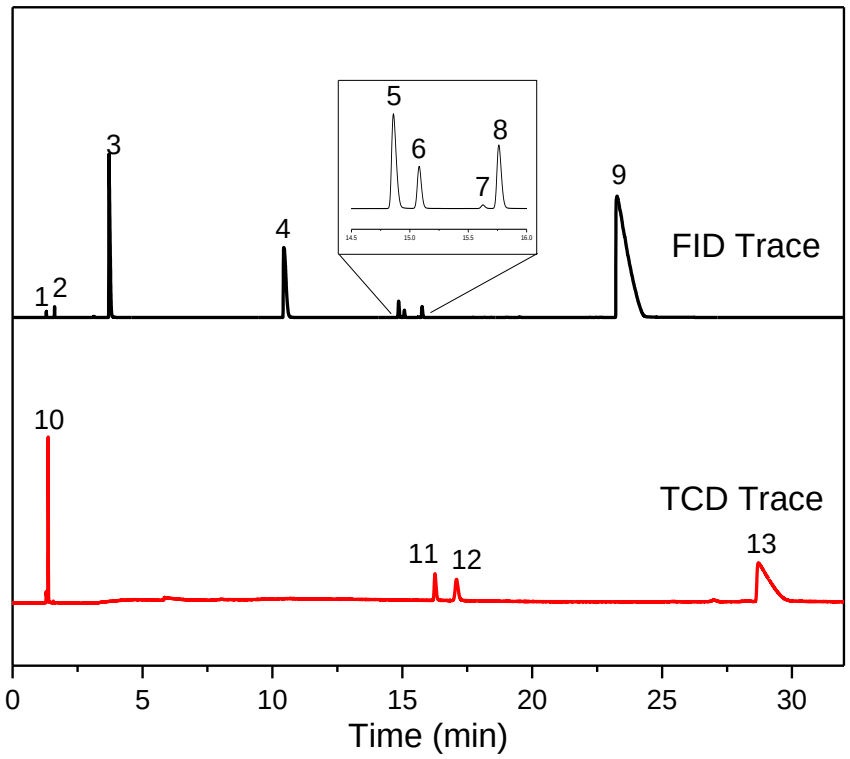

Figure 2.8: FID and TCD traces for furan deoxygenation over $Co_{1.00}Ru_{1.00}P/SiO_2$ after 48 h on-stream.

Crotonaldehyde deoxygenation measurements were carried out over a range of temperatures for the $Co_xRu_{2-x}P/SiO_2$ (473-573 K) and $Co_xRh_{2-x}P/SiO_2$ (303-523 K) catalysts. 0.1 g of catalyst was placed in a quartz u-tube, the sample was purged with He (15 mL/min) for 30 min, following which the sample was then subjected to a TPR process to remove the passivation layer present on the metal phosphide catalysts, and to reduce Ru/SiO_2 precursors to the metallic state. The sample was heated to 650 K under flowing H_2 (50 mL/min) over 1 h and then held at 650 K for 2 h. The catalyst sample was then cooled to 303 K, and hydrogen was flowed through bubblers filled with crotonaldehyde that had been cooled to 273 K, resulting in a 1 mol% crotonaldehyde/ H_2 mixture being passed over the catalyst. The catalyst was heated to the first temperature at which its deoxygenation properties would be tested, and effluent from the reactor was analyzed every 30 min for 3 h using an on-line HP5890 series II Gas chromatograph containing a HP-PLOT/Q column, the flow from which was split to parallel flame ionization (FID) and thermal conductivity (TCD) detectors.

The catalyst was then heated to the next temperature at which it would be tested. This process was repeated for a series of temperatures between 303 K and 573 K in order to study the change in catalytic activity and selectivity as a function of temperature. A typical FID plot for crotonaldehyde deoxygenation testing is shown in figure 2.9, with peaks listed in table 2.7.

Table 2.7: Peak assignments for the GC trace plotted in Fig. 2.9.

Peak	Assignment	Retention Time (min)
1	propylene	8.5
2	propane	9.0
3	1-butene	12.64
4	butane	12.8
5	trans-butene	13.1
6	cis-butene	13.3
7	butyraldehyde	19.1
8	crotonaldehyde	20.8
9	crotyl alcohol	22.3
10	butanol	22.5

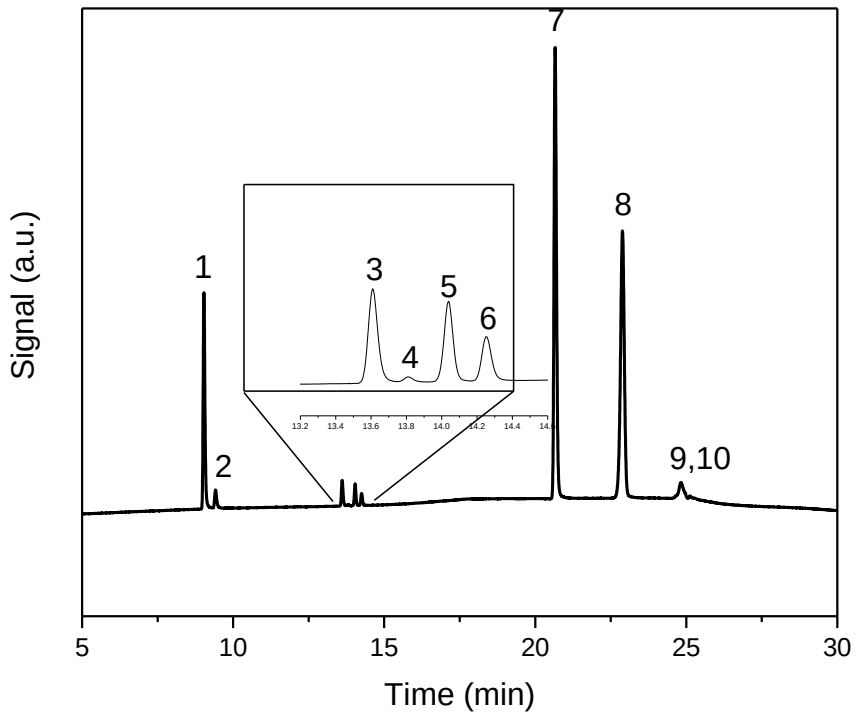

Figure 2.8: FID trace for crotonaldehyde deoxygenation over $Co_{1.00}Ru_{1.00}P/SiO_2$.

Deoxygenation Activity Measurements

The molar flow rate of furan or crotonaldehyde through the reactor was determined as follows. The Antoine equation (Equation 2.4) was used to determine the vapor pressure, where P is pressure of the compound, T is temperature, and A (unitless), B (K), and C (K) are constants for a given compound.

$$P = 10^{A-\frac{B}{C+T}} \tag{2.4}$$

Using a recirculating bath, the temperature of the bubblers containing furan or crotonaldehyde was set to a specific temperature corresponding to a desired vapor pressure. The calculated vapor pressure was used to determine a mol% of the compound in the reactor feed (Equations 2.5-2.7), which was converted into a molar flow rate using the ideal gas law and flow rate of H_2 through the reactor (Equations 2.8, 2.9).

$$\text{Mol \% Compound} = \frac{P_{Compound}}{P_{atm}} * 100 \quad (2.5)$$

$$\text{Mol \% Compound} = \frac{P_{crotonaldehyde}}{P_{atm}} * 100 = \frac{7.6 \text{ torr}}{760 \text{ torr}} * 100 = 1 \text{ mol\% crotonaldehyde} \quad (2.6)$$

$$\text{Mol \% Compound} = \frac{P_{furan}}{P_{atm}} * 100 = \frac{61.62 \text{ torr}}{760 \text{ torr}} * 100 = 8.15 \text{ mol\% furan} \quad (2.7)$$

$$PV = nRT \quad (2.8)$$

$$n = \frac{PV}{RT} = \frac{1 \text{ atm} * 0.05 \frac{L}{min}}{0.08206 \frac{L*atm}{mol*K} * 273 \text{ K}} = 0.002232 \frac{mol}{min} \quad (2.9)$$

The molar flow rates calculated were used with the mol% crotonaldehyde or furan present in the reactor feed to calculate flow rates for each model compound in units of nmol/s (Equations 2.10, 2.11).

$$\text{Crotonaldehyde Flow Rate} = 0.2232 \frac{mol}{min} * 0.01 * \left(\frac{10^9 nmol}{1 mol}\right) * \left(\frac{1 min}{60 s}\right) = 3720 \frac{nmol}{s} \quad (2.10)$$

$$\text{Furan Flow Rate} = 0.2232 \frac{mol}{min} * 0.0815 * \left(\frac{10^9 nmol}{1 mol}\right) * \left(\frac{1 min}{60 s}\right) = 30318 \frac{nmol}{s} \quad (2.11)$$

Deoxygenation activities were then calculated using the relative peak area corresponding to that compound as detected by GC, and molar flow rates used to report activities in units of nanomoles compound converted per second per gram of catalyst (nmol * s^{-1} * g^{-1}).

3. Results

3.1 Catalyst Characterization

Powder X-ray diffraction (XRD) was used to confirm the crystalline phases present and to determine average crystallite sizes using the Scherrer equation (Eqn. 2.1) in each of the catalysts prepared in this research by comparing the diffraction patterns of the synthesized catalysts to reference patterns from the JCPDS database.[36] Energy-dispersive X-ray spectroscopy (EDX) was used to determine the elemental composition of each catalyst. X-ray photoelectron spectroscopy (XPS) was used to probe chemical states and measure elemental concentrations at catalyst surfaces. Brunauer-Emmett-Teller (BET) theory and N_2 adsorption was used to make single-point surface area measurements of the prepared catalysts, and CO chemisorption was used to estimate the active site densities of the catalysts. Finally, carbon and sulfur analysis was used to determine the carbon content of the catalysts after deoxygenation measurements.

3.1.1 X-ray Diffraction Analysis

Ru/SiO_2 Catalyst

Figure 3.1 shows the X-ray diffraction pattern for an as-prepared Ru/SiO_2 catalyst. The XRD pattern compares well with a Ru reference pattern (card no. 00-006-0663) from the JCPDS database.[36] The average Ru crystallite size (8 nm) of the Ru/SiO_2 catalyst was calculated using the Scherrer equation and the peak at 38.4^o corresponding to the {100} reflection in figure 3.1. An XRD pattern of the Ru/SiO_2 catalyst was acquired after furan deoxygenation testing and there was no change observed in the crystalline phase or average crystallite size (6 nm) of the catalyst.

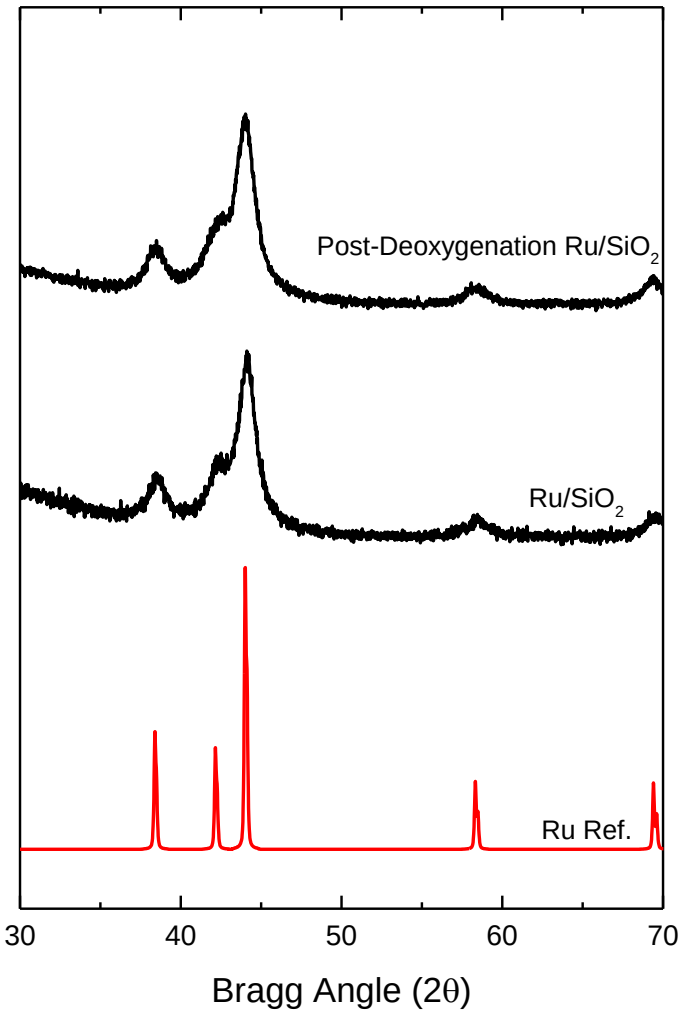

Figure 3.1: XRD patterns of an as-prepared Ru/SiO_2 catalyst before and after furan deoxygenation testing.

Co/SiO_2 Catalyst

Figure 3.2 shows the X-ray diffraction pattern for an as-prepared Co/SiO_2 catalyst. The XRD pattern exhibits no peaks with which to compare with a Co reference pattern (card no. 01-070-2633) from the JCPDS database, suggesting that the particle size is below the limit of detection for XRD.[36] An XRD pattern of the Co/SiO_2 catalyst following crotonaldehyde deoxygenation testing showed a broad peak, suggesting that minor sintering had occurred over the course of testing. The average

crystallite size (<5 nm) of the catalyst following testing could not be calculated using the Scherrer equation.

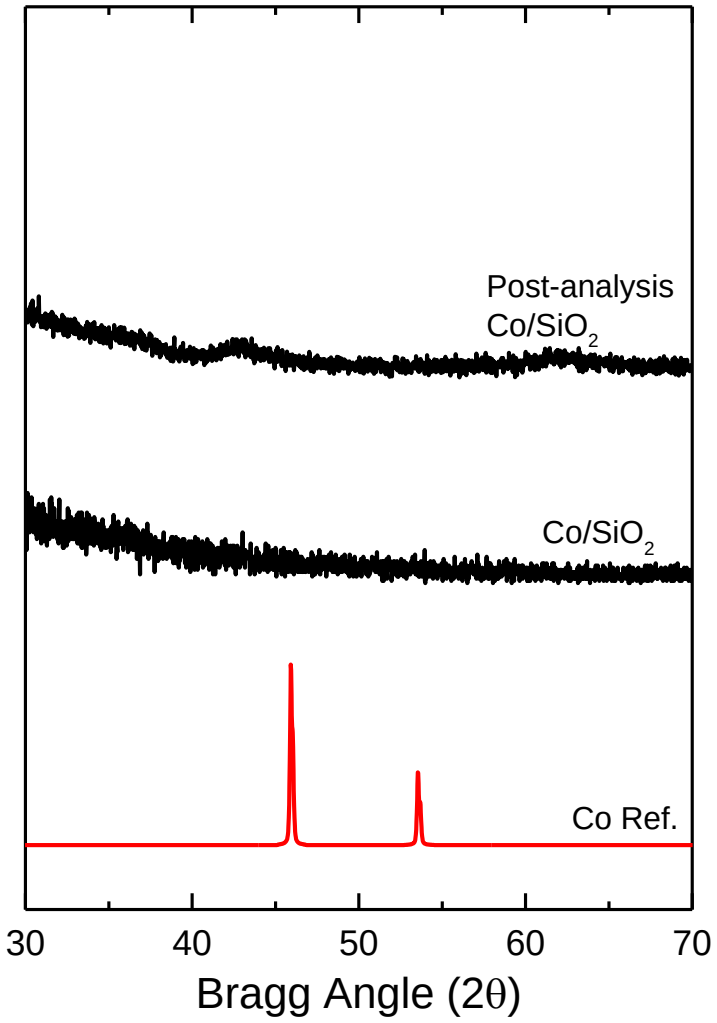

Figure 3.2: XRD pattern of an as-prepared Co/SiO_2 catalyst before and after crotonaldehyde deoxygenation testing.

Ru_2P/SiO_2 Catalyst

Figure 3.3 shows the X-ray diffraction pattern for an as-prepared 15 wt% Ru_2P/SiO_2 catalyst. The diffraction pattern compares well with a Ru_2P reference pattern (card no. 96-900-9204) from the JCPDS database.[36] The average crystallite size of the Ru_2P (7 nm) was calculated using the Scherrer equation and the peak at 38.4° corresponding to the {112} reflection. An XRD pattern of the

Ru_2P/SiO_2 catalyst was acquired after crotonaldehyde deoxygenation testing and no significant changes were observed in the crystalline phase or average crystallite size (7 nm) of the catalyst.

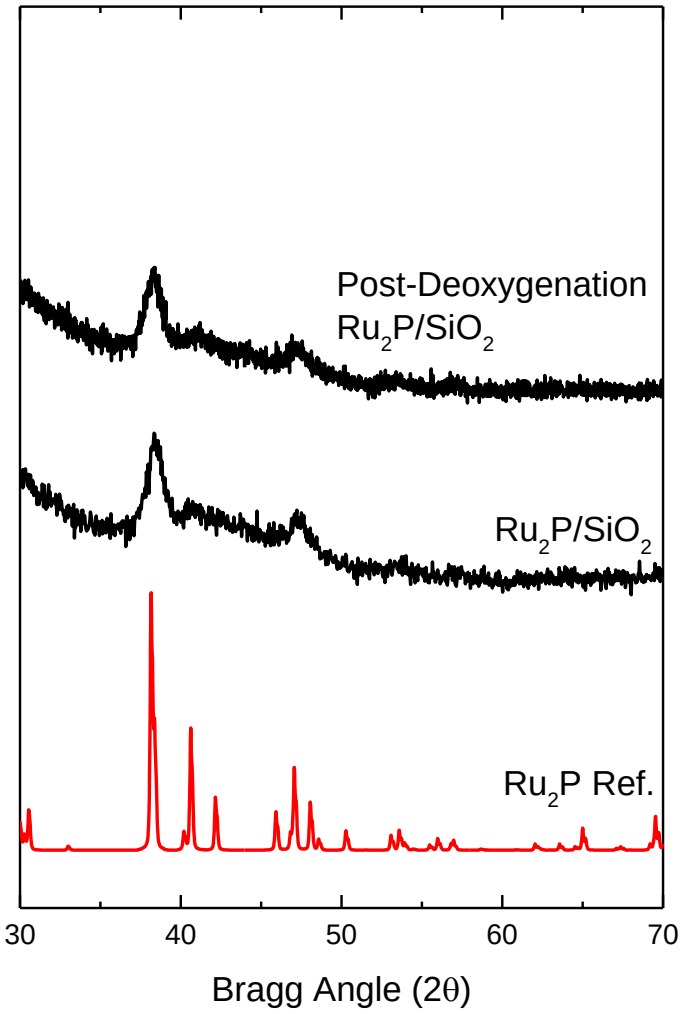

Figure 3.3 XRD pattern of an as-prepared Ru_2P/SiO_2 catalyst before and after crotonaldehyde deoxygenation testing.

Rh_2P/SiO_2 catalyst

Figure 3.4 shows the X-ray diffraction pattern for an as-prepared 15 wt% Rh_2P/SiO_2 catalyst. The diffraction pattern compares well with an Rh_2P reference pattern (card no: 96-101-1345) from the JCPDS database.[36] The average crystallite size of the Rh_2P (6 nm) was calculated using the Scherrer equation and the peak at 32.73° corresponding to the {002} reflection. An XRD pattern of

the Rh_2P/SiO_2 catalyst was acquired after crotonaldehyde deoxygenation testing and no change in the crystalline phase of the catalyst was observed. A significant change was observed in the average crystallite size (21 nm) of the catalyst following testing, indicating that sintering occurred during deoxygenation testing.

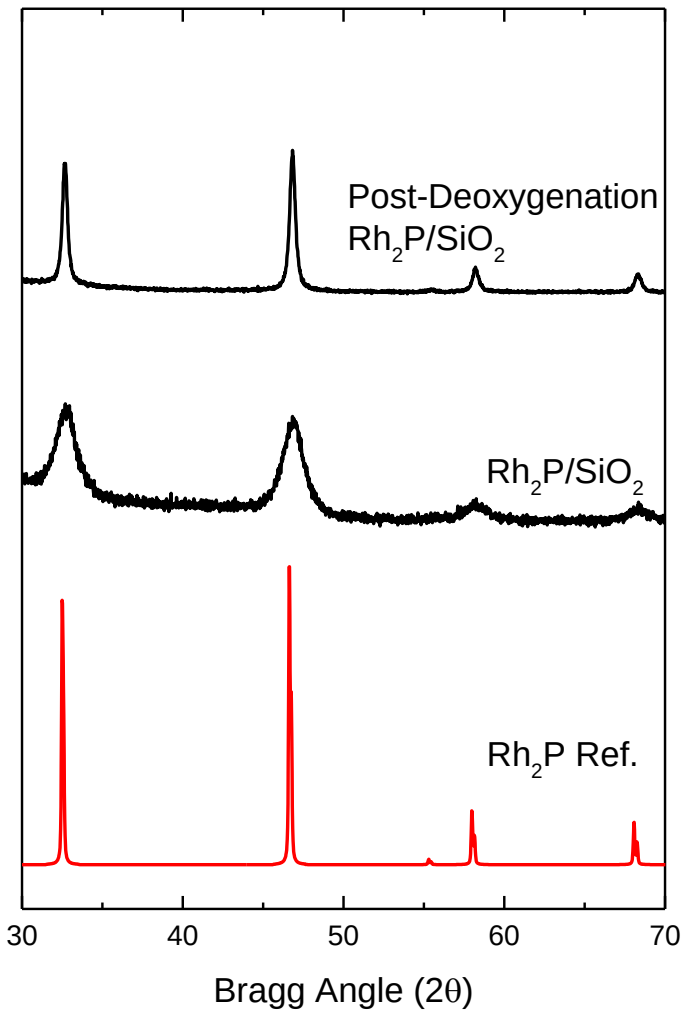

Figure 3.4: XRD pattern of an as-prepared Rh_2P/SiO_2 catalyst before and after crotonaldehyde deoxygenation testing.

Co_2P/SiO_2 Catalyst

Figure 3.5 shows the measured X-ray diffraction pattern for an as-prepared 15 wt% Co_2P/SiO_2 catalyst. The diffraction pattern does not compare well with the Co_2P reference pattern (card no: 99-017-0003) from the JCPDS database, as the observed peaks are too small to properly confirm crystalline phase.[36] The average crystallite size of the catalyst (9 nm) was calculated using the Scherrer equation and the peak at 40.72° corresponding to the {112} reflection. An XRD pattern of the Co_2P/SiO_2 catalyst was acquired after furan deoxygenation testing and no significant change was observed in the crystalline phase, but an increase in the average crystallite size (13 nm) of the catalyst was measured.

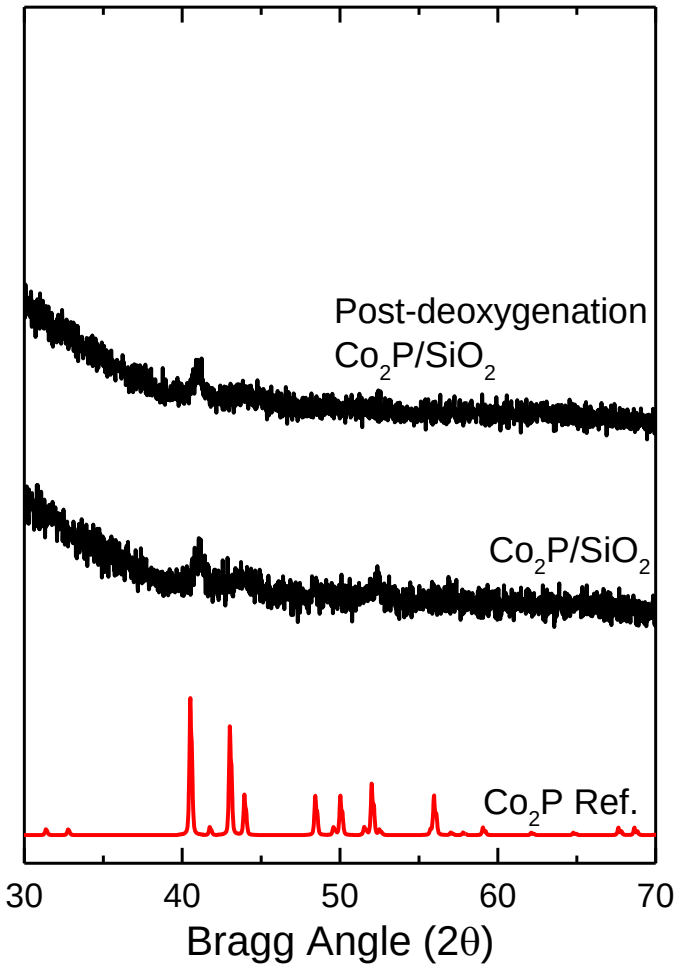

Figure 3.5: XRD pattern of an as-prepared Co_2P/SiO_2 before and after crotonaldehyde deoxygenation testing.

$Co_xRu_{2-x}P/SiO_2$ Catalysts

XRD patterns of the 25 wt % $Co_xRu_{2-x}P/SiO_2$ catalysts showed greater peak intensity than the 15 wt % series, as indicated by the patterns for the 15 and 25 wt% $Co_{1.00}Ru_{1.00}P/SiO_2$ catalysts (Figure 3.6).

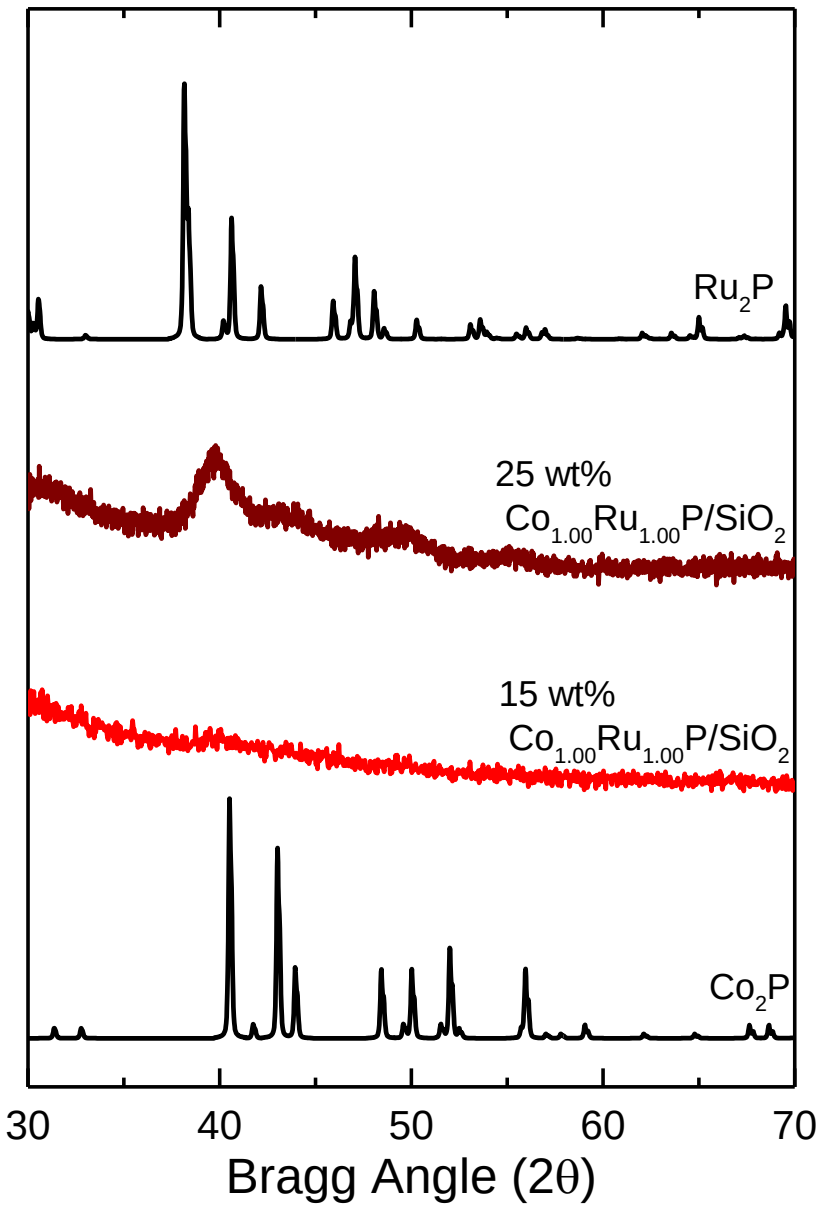

Figure 3.6: Comparison between XRD patterns for the 15 and 25 wt% $Co_{1.00}Ru_{1.00}P/SiO_2$ catalyst.

X-ray diffraction patterns were acquired for the 15 wt % $Co_xRu_{2-x}P/SiO_2$ catalyst series (Figure 3.7); a gradual shift in peak location can be observed as the composition of the catalysts is altered from Co-rich to Ru-rich. The peak intensities for many compositions in the 15 wt% $Co_xRu_{2-x}P/SiO_2$ catalysts are too low to confirm phase purity, so a series of 25 wt % $Co_xRu_{2-x}P/SiO_2$ catalysts was prepared. The XRD patterns of the 25 wt % $Co_xRu_{2-x}P/SiO_2$ catalysts (Figure 3.8) showed well-defined peaks and enabled confirmation that the catalysts contained a single crystalline phase, indicating that the synthesis method yielded phase-pure bimetallic phosphides. The XRD pattern of each $Co_xRu_{2-x}P/SiO_2$ catalyst showed a single crystalline phase, with a gradual shift in peak location as catalyst composition changed. Between the $Co_{1.75}Ru_{0.25}P/SiO_2$ and $Co_{0.25}Ru_{1.75}P/SiO_2$ catalysts, the location of the {112} reflection changes from 41.0° to 38.5°. The shift in peak locations suggests that a solid solution containing one bimetallic phosphide phase is present, as opposed to mixture of two separate monometallic phosphide phases. If the catalysts were instead composed of mixed Co_2P and Ru_2P phases, then their XRD patterns would show peaks for each phase, with the intensity of the different phases changing with composition.

Diffraction patterns were acquired for each of the $Co_xRh_{2-x}P/SiO_2$ catalysts in order to confirm their phase purity (Figure 3.9). The acquired diffraction patterns were found to be phase-pure and corresponded to either Co_2P or Rh_2P crystal phases, suggesting that only one crystalline phase is present in each sample. The Rh-rich samples showed two peaks at 32.5° and 46.6°, which match the reference pattern for Rh_2P (card no: 96-101-1345). The Co-rich samples show one peak at 40.5°, which matches with the largest peak in the Co_2P reference pattern (card no: 99-017-0003). A significant change is observed between the diffraction patterns of $Co_{0.75}Rh_{1.25}P$ and Co_1Rh_1P showcasing the change in crystalline phase that occurs between catalysts with high Rh content and those with high Co content.

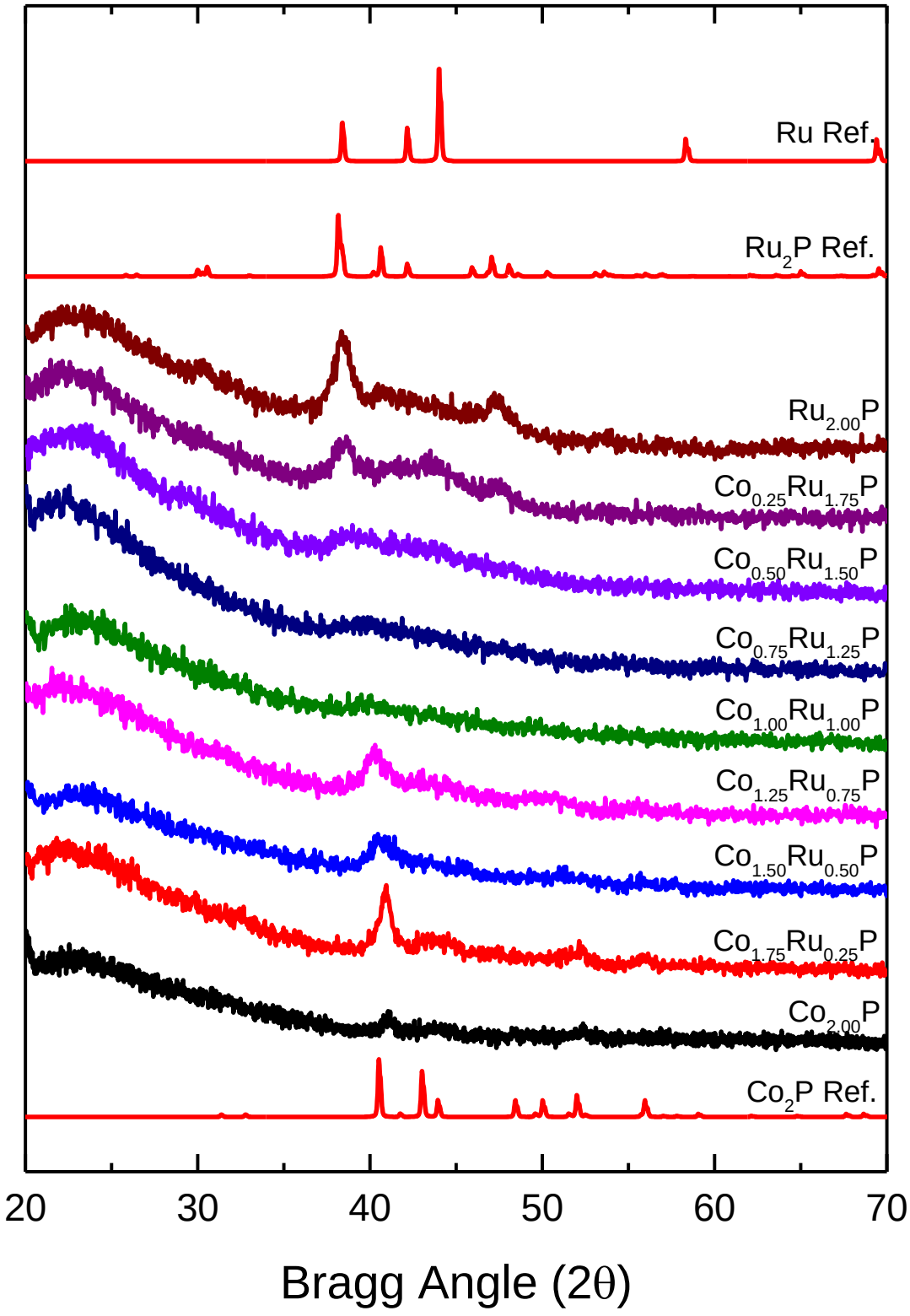

Figure 3.7: XRD patterns for as-prepared 15 wt% $Co_xRu_{2-x}P/SiO_2$ catalysts.

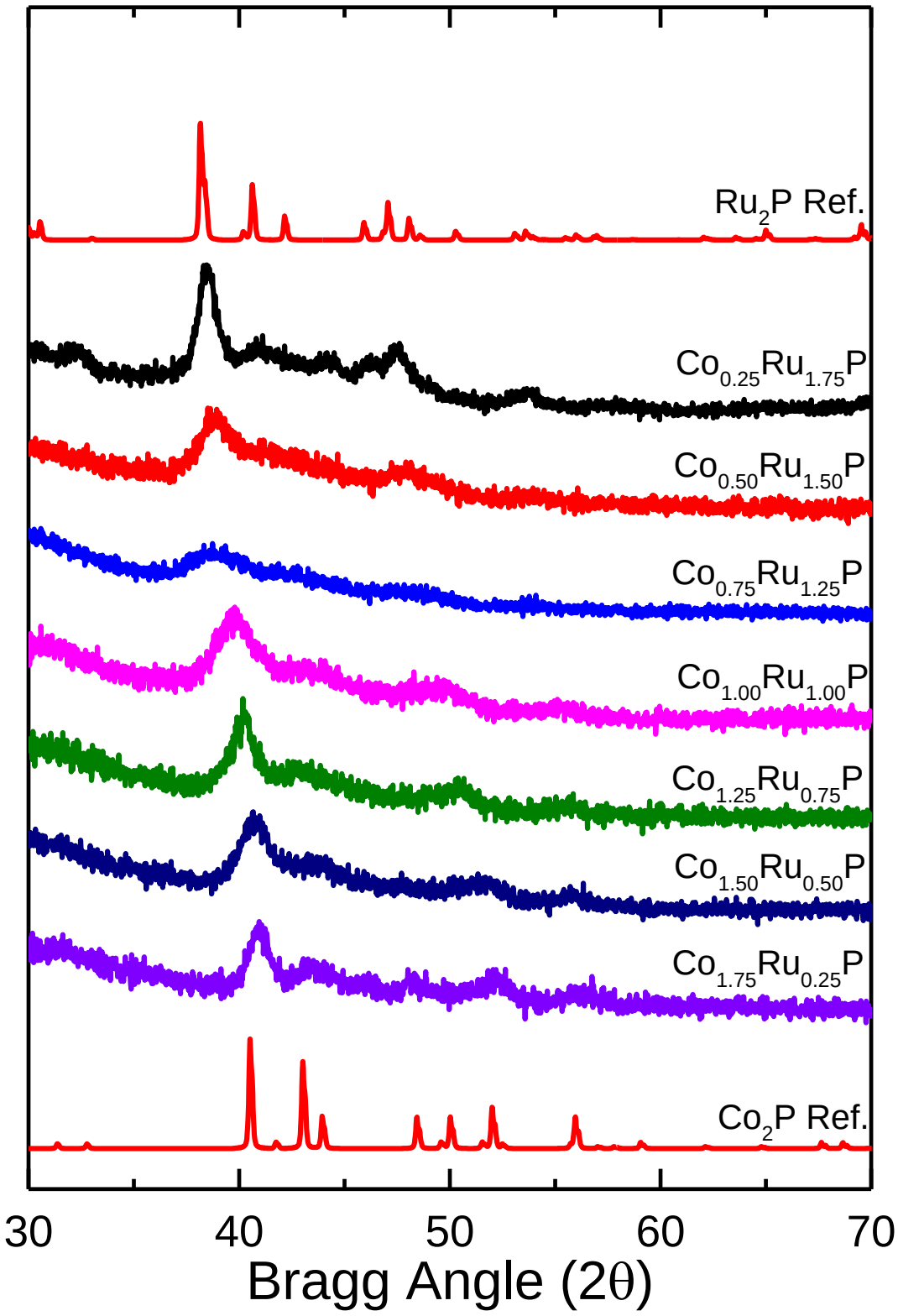

Figure 3.8: XRD patterns for as-prepared 25 wt% $Co_xRu_{2-x}P/SiO_2$ catalysts.

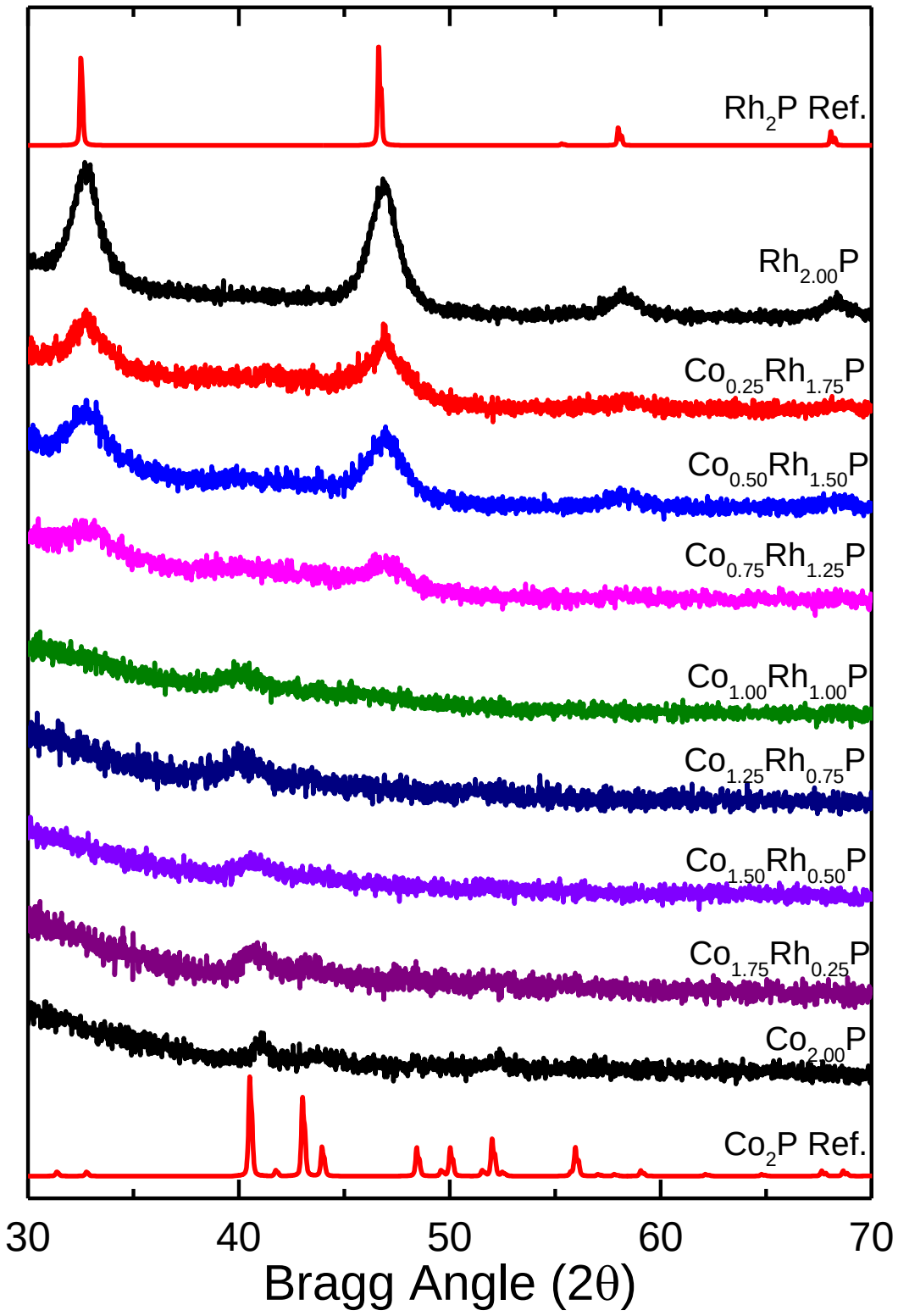

Figure 3.9: XRD patterns of as-prepared $Co_xRh_{2-x}P/SiO_2$ catalysts.

3.1.2 Energy Dispersive X-ray Analysis

Energy dispersive X-ray analysis is a technique used to quantify elemental compositions of solid samples. SEM-EDX analysis was used to determine the elemental compositions of the 15 and 25 wt% $Co_xRu_{2-x}P/SiO_2$ catalysts (Figure 3.10) as well as the 15 wt% $Co_xRh_{2-x}P/SiO_2$ catalysts (Figure 3.11). Elemental concentrations were quantified by measuring the area of the response generated by the phosphorous K_α (2.0 keV), ruthenium L_α (2.6 keV), rhodium L_α and L_β (2.7 and 2.8 keV) and cobalt K_α (6.9 keV) transitions.

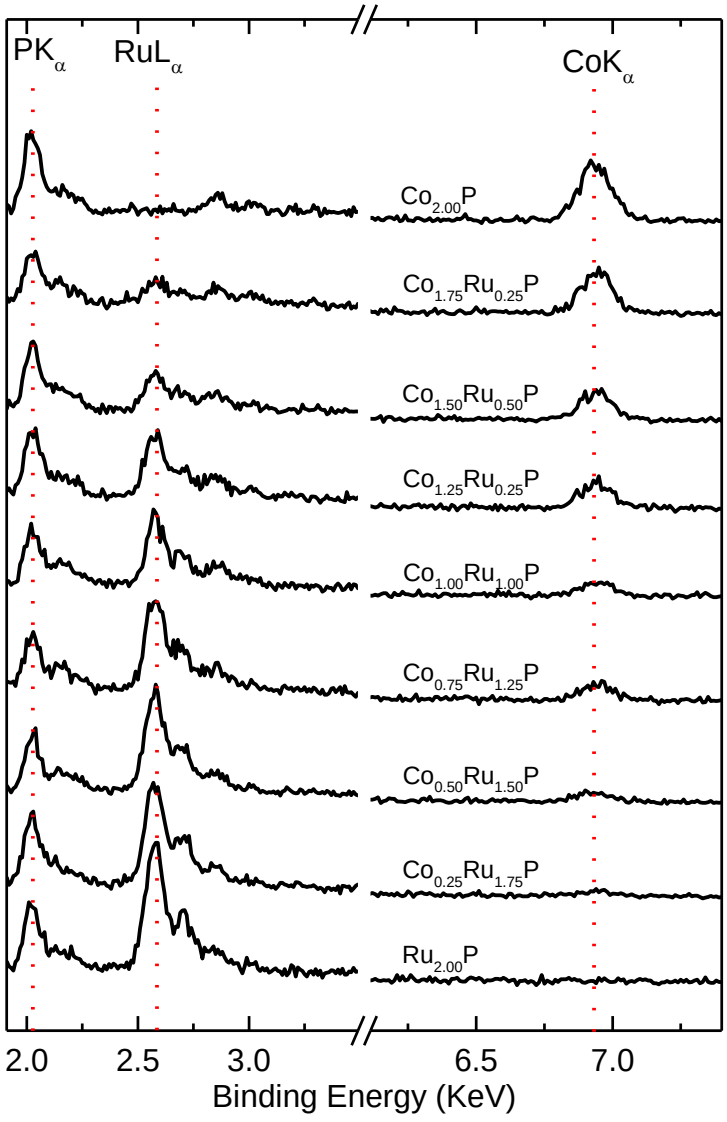

Figure 3.10: EDX spectra of as-prepared 15 wt% $Co_xRu_{2-x}P/SiO_2$ catalysts.

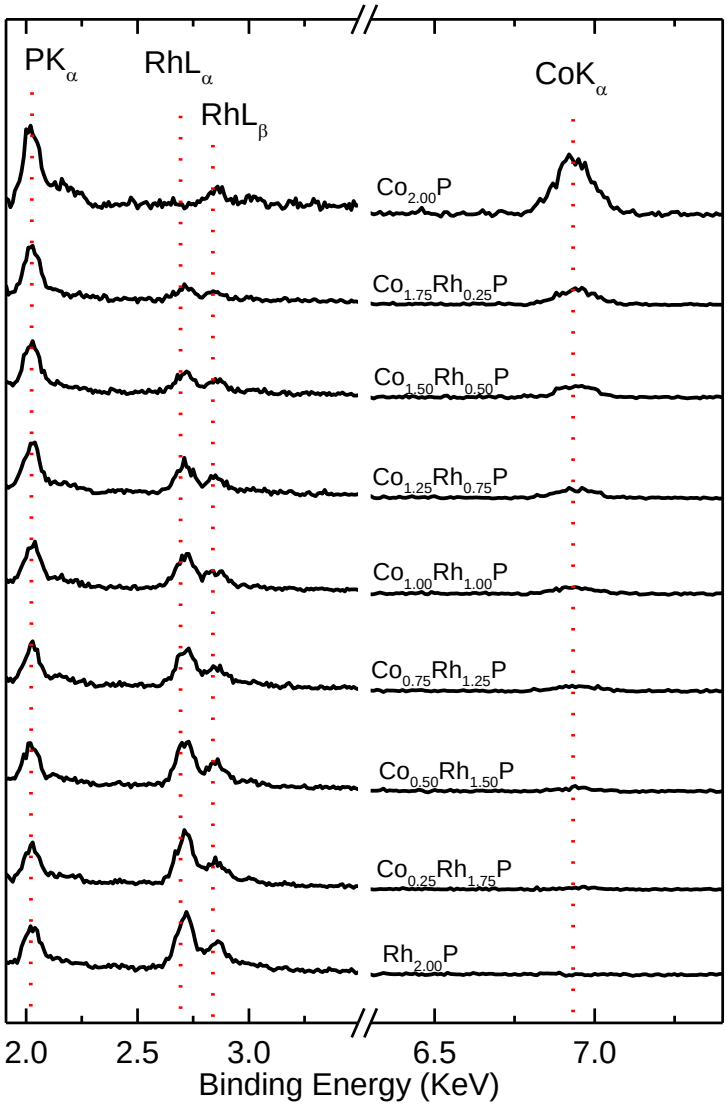

Figure 3.11: EDX spectra of as-prepared 15 wt% $Co_xRh_{2-x}P/SiO_2$ catalysts.

The metal compositions of the $Co_xRh_{2-x}P/SiO_2$ and $Co_xRu_{2-x}P/SiO_2$ catalysts measured using EDX agreed well with the nominal compositions (Figures 3.12, 3.14, 3.16), except that all samples were somewhat Co-rich for the 15 wt% $Co_xRu_{2-x}P/SiO_2$ catalysts. The phosphorous to metal molar ratios (P/M) were not consistent between the 15 and 25 wt% $Co_xRu_{2-x}P/SiO_2$ catalysts (Figures 3.13, 3.15). The P contents of the $Co_xRh_{2-x}P/SiO_2$ and 25 wt% $Co_xRu_{2-x}P/SiO_2$ catalysts were found to be greater

than the nominal values (Fig. 3.15, 3.17), while the 15 wt% $Co_xRu_{2-x}P/SiO_2$ series had P contents that were mostly below the nominal values (Fig. 3.13).

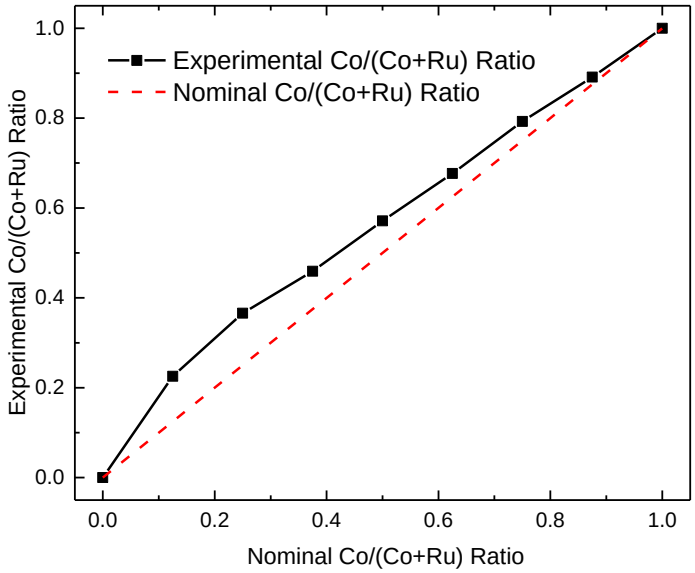

Figure 3.12: Experimental Co/(Co+Ru) molar ratio for 15 wt% $Co_xRu_{2-x}P/SiO_2$ catalysts.

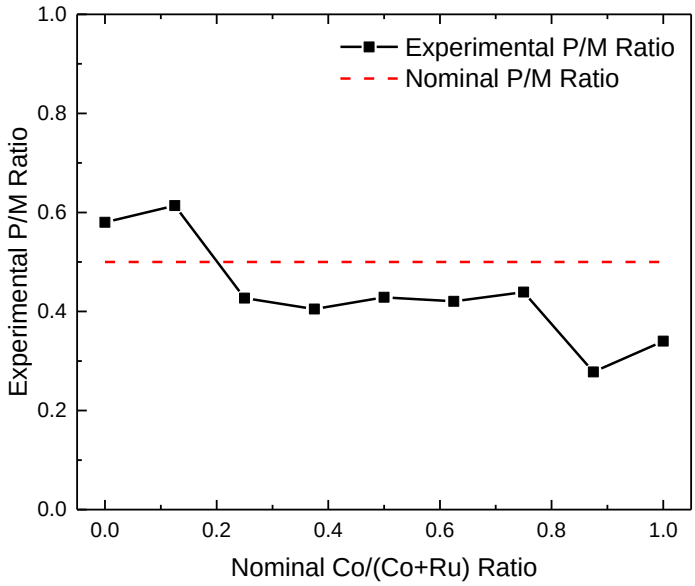

Figure 3.13: Experimental P/(Co+Ru) molar ratio for 15 wt% $Co_xRu_{2-x}P/SiO_2$ catalysts.

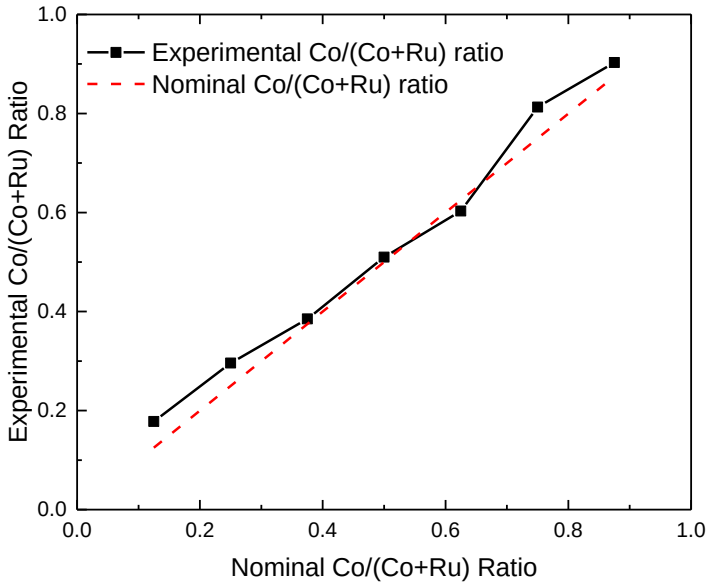

Figure 3.14: Experimental Co/(Co+Ru) molar ratio for 25 wt% $Co_xRu_{2-x}P/SiO_2$ catalysts.

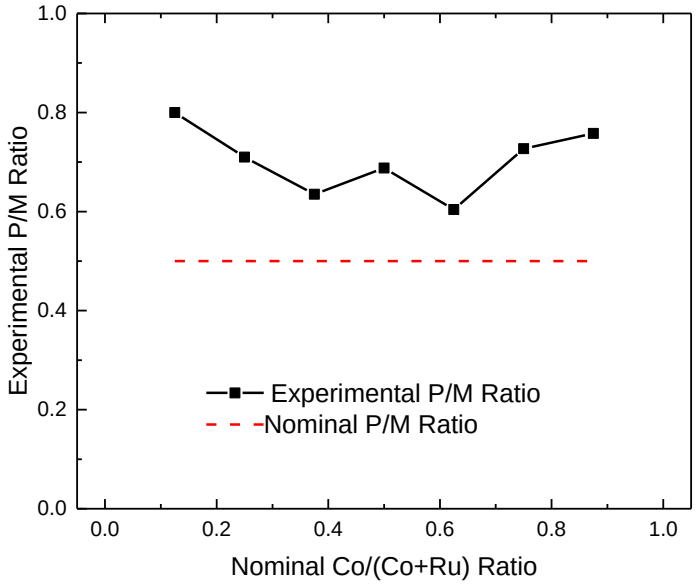

Figure 3.15: Experimental P/(Co+Ru) molar ratio for 25 wt% $Co_xRu_{2-x}P/SiO_2$ catalysts.

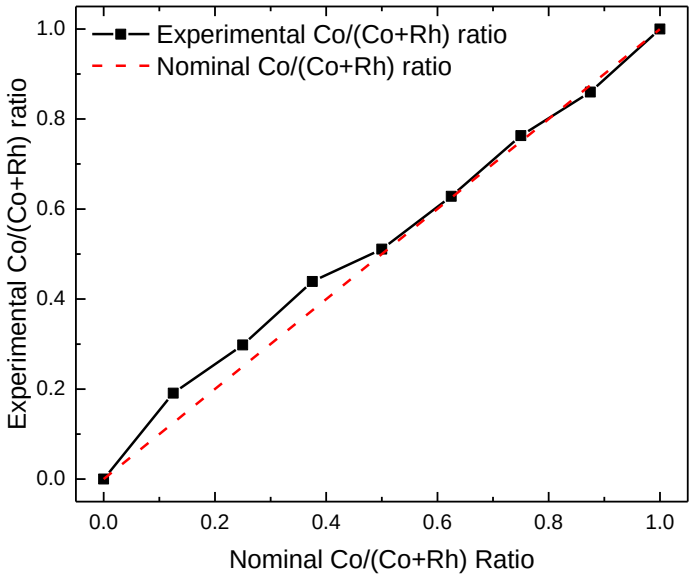

Figure 3.16: Experimental Co/(Co+Rh) molar ratio for $Co_xRh_{2-x}P/SiO_2$ catalysts.

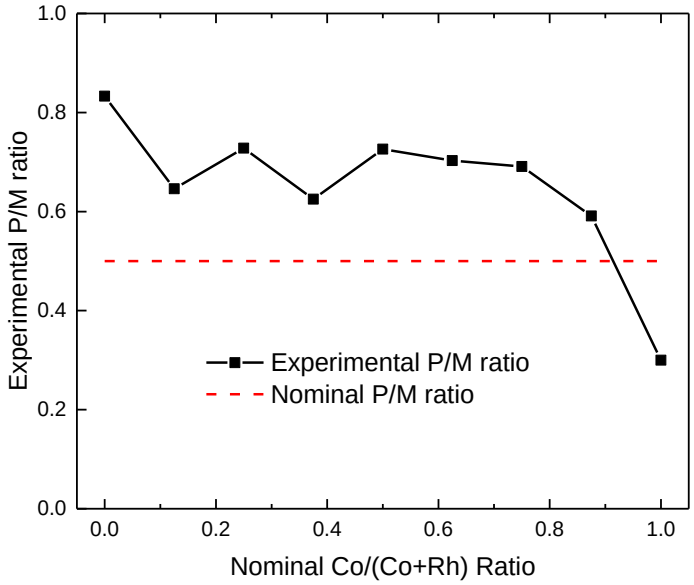

Figure 3.17: Experimental P/(Co+Rh) molar ratio for $Co_xRh_{2-x}P/SiO_2$ catalysts.

3.1.3 BET Surface Area and CO Chemisorption Analysis

The BET surface areas were for the 15 wt% $Co_xRu_{2-x}P/SiO_2$ and $Co_xRh_{2-x}P/SiO_2$ catalysts are plotted in Figures 3.18 and 3.19 and reported in Tables 3.1 and 3.2.

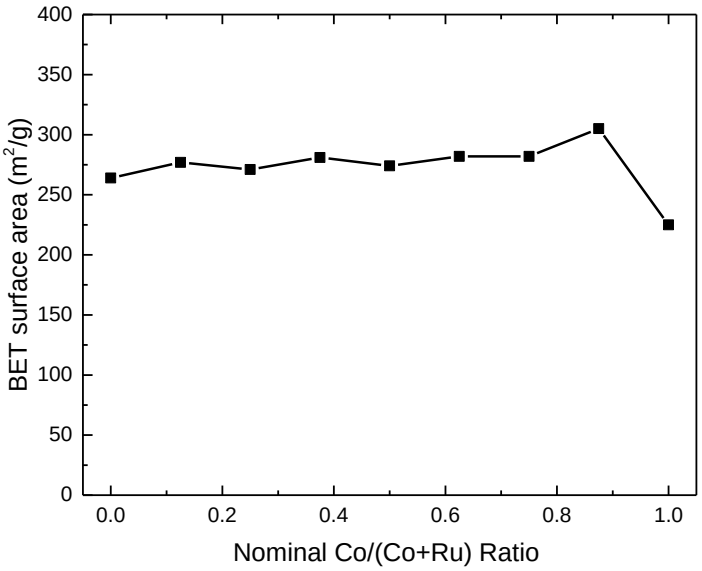

Figure 3.18: BET surface areas of 15 wt% $Co_xRu_{2-x}P/SiO_2$ catalysts.

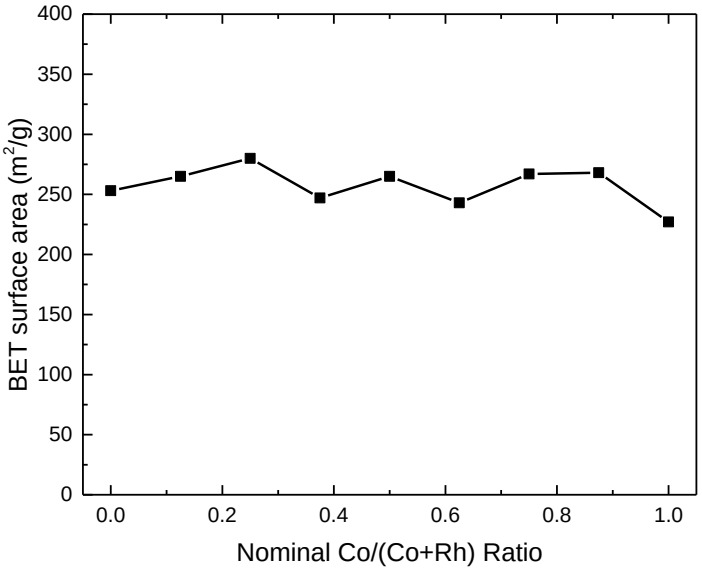

Figure 3.19: BET surface areas of 15 wt% $Co_xRh_{2-x}P/SiO_2$ catalysts.

Table 3.1: BET surface areas and CO chemisorption capacities of 15 wt% $Co_xRu_{2-x}P/SiO_2$ catalysts.

Nominal Composition	Surface Area (m^2/g)	Chemisorption Capacity (μmol/g)
Ru_2P	264	200
$Co_{0.25}Ru_{1.75}P$	277	268
$Co_{0.5}Ru_{1.5}P$	271	402
$Co_{0.75}Ru_{1.25}P$	281	226
Co_1Ru_1P	274	255
$Co_{1.25}Ru_{0.75}P$	282	146
$Co_{1.5}Ru_{0.5}P$	282	120
$Co_{1.75}Ru_{0.25}P$	305	148
Co_2P	227	65

The CO chemisorption capacities of the 15 wt% $Co_xRu_{2-x}P/SiO_2$ catalysts are listed in Tables 3.1 and 3.2 and are plotted in Figures 3.20 and 3.21, and it was found that catalysts with higher Ru content possessed higher chemisorption capacities. The Ru-rich $Co_xRu_{2-x}P/SiO_2$ catalysts ($0 \leq x \leq 2$) had higher CO chemisorption capacities than the Ru_2P/SiO_2 catalyst, while the Co-rich catalysts had higher CO chemisorption capacities than the Co_2P/SiO_2 catalyst, but lower chemisorption capacity than the Ru-rich catalysts.

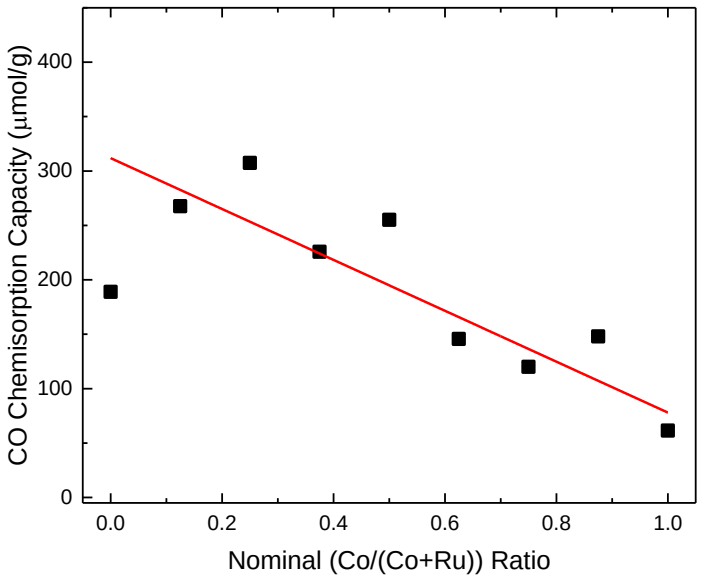

Figure 3.20: CO chemisorption capacities of 15 wt% $Co_xRu_{2-x}P/SiO_2$ catalysts.

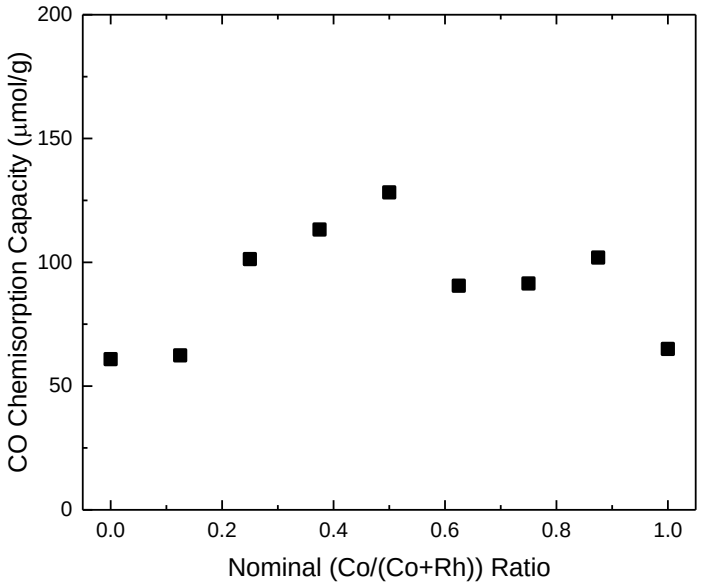

Figure 3.21: CO chemisorption capacities of 15 wt% $Co_xRh_{2-x}P/SiO_2$ catalysts.

Table 3.2: BET surface areas and CO chemisorption capacities of 15 wt% $Co_xRh_{2-x}P/SiO_2$ catalysts.

Nominal Composition	Chemisorption Capacity (μmol/g)	Surface Area (m^2/g)
Rh_2P	61	253
$Co_{0.25}Rh_{1.75}P$	62	265
$Co_{0.5}Rh_{1.5}P$	101	280
$Co_{0.75}Rh_{1.25}P$	113	247
Co_1Rh_1P	128	265
$Co_{1.25}Rh_{0.75}P$	90	243
$Co_{1.5}Rh_{0.5}P$	91	267
$Co_{1.75}Rh_{0.25}P$	112	268
Co_2P	65	227

3.1.4 X-ray Photoelectron Spectroscopy

XPS spectra were collected for selected $Co_xRu_{2-x}P/SiO_2$ and $Co_xRh_{2-x}P/SiO_2$ catalysts (Fig. 3.22, 3.23). Peaks in the XPS spectra correlate with the binding energies of electrons in core levels of different elements. The identified peaks were compared with a National Institute of Standards and Technologies (NIST) XPS database to identify the elements in each sample.[39] Differences in the chemical environment of an atom results in slight changes in electron binding energies, causing peaks to shift from their reference state values. Information regarding the chemical state of identified elements can then be inferred from the direction and magnitude of the binding energy shift by comparison with literature values. Binding energies measured for the $Co_xRu_{2-x}P/SiO_2$ and $Co_xRh_{2-x}P/SiO_2$ catalysts are reported in Tables 3.3 and 3.4, respectively. The presence of Co in samples was confirmed using the Co $2p_{3/2}$ peak, which for Co^0 is located at 779.1 eV.[39] The presence of Ru in samples was confirmed by identifying the Ru $3d_{5/2}$ peak, which for Ru^0 is located at 280.0-280.2 eV.[39] The presence of Rh in samples was confirmed using the Rh $3d_{5/2}$ peak, which for Rh^0 is

located at 307.0 eV. The presence of P in samples was confirmed using the P $2p_{1/2}$ and P $2p_{3/2}$ peaks, which for elemental P^0 are located near 129.4 and 130.2 eV, respectively.[39] The instrument used in this study was unable to resolve the two peaks however, and as such P appears as a single P 2p peak.

In the XPS spectra of the $Co_xRu_{2-x}P/SiO_2$ catalysts (Fig. 3.22), the P 2p peak was observed shift to higher binding energies, occurring at values in the range 133.7-134.8 eV, which is consistent with binding energies observed for P in highly oxidized states, such as PO_4^{3-}. The Ru $3d_{5/2}$ peak was observed at values in the range 280.6-281.1 eV, which are slightly higher than values reported for Ru^0. The Co $2p_{3/2}$ peak was observed at values 781.1-782.0 eV. The observed peaks are consistent with values reported for Co in +2 and +3 oxidation states.

In the XPS spectra of the $Co_xRh_{2-x}P/SiO_2$ catalysts (Fig. 3.23), the P 2p peak was observed to shift higher binding energies, occurring at values in the range 134.0-135.8 eV, which is consistent with binding energies observed for P in a +5 oxidation state. The Rh $3d_{5/2}$ peak was observed at 307.5-307.8 eV, which are slightly higher than values reported for Rh^0. The Co $2p_{3/2}$ peak was observed at values between 782.0 and 782.3 eV. The observed peaks are consistent with values reported for Co in +2 and +3 oxidation states.

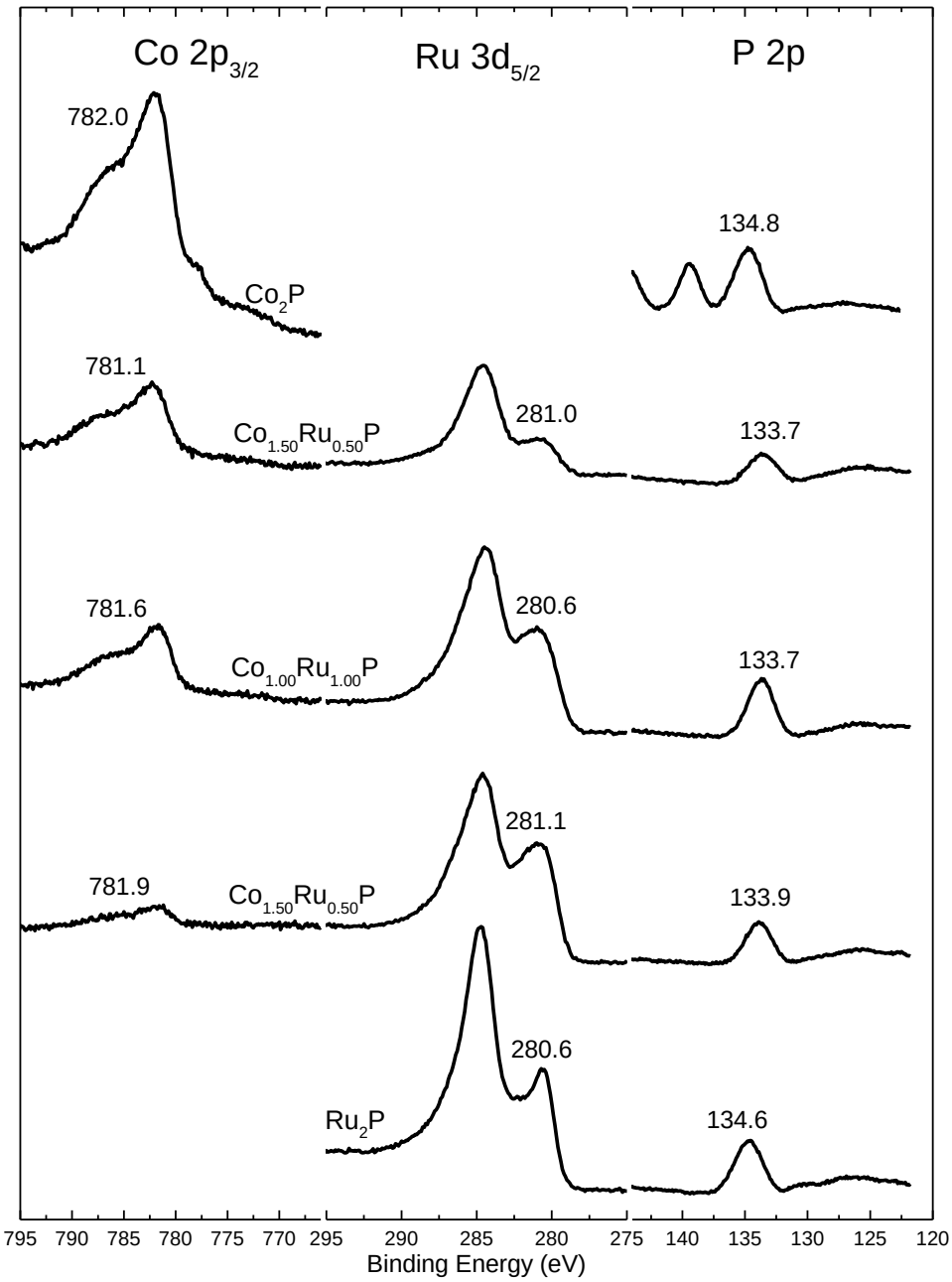

Figure 3.22: XPS spectra of select $Co_xRu_{2-x}P/SiO_2$ catalysts.

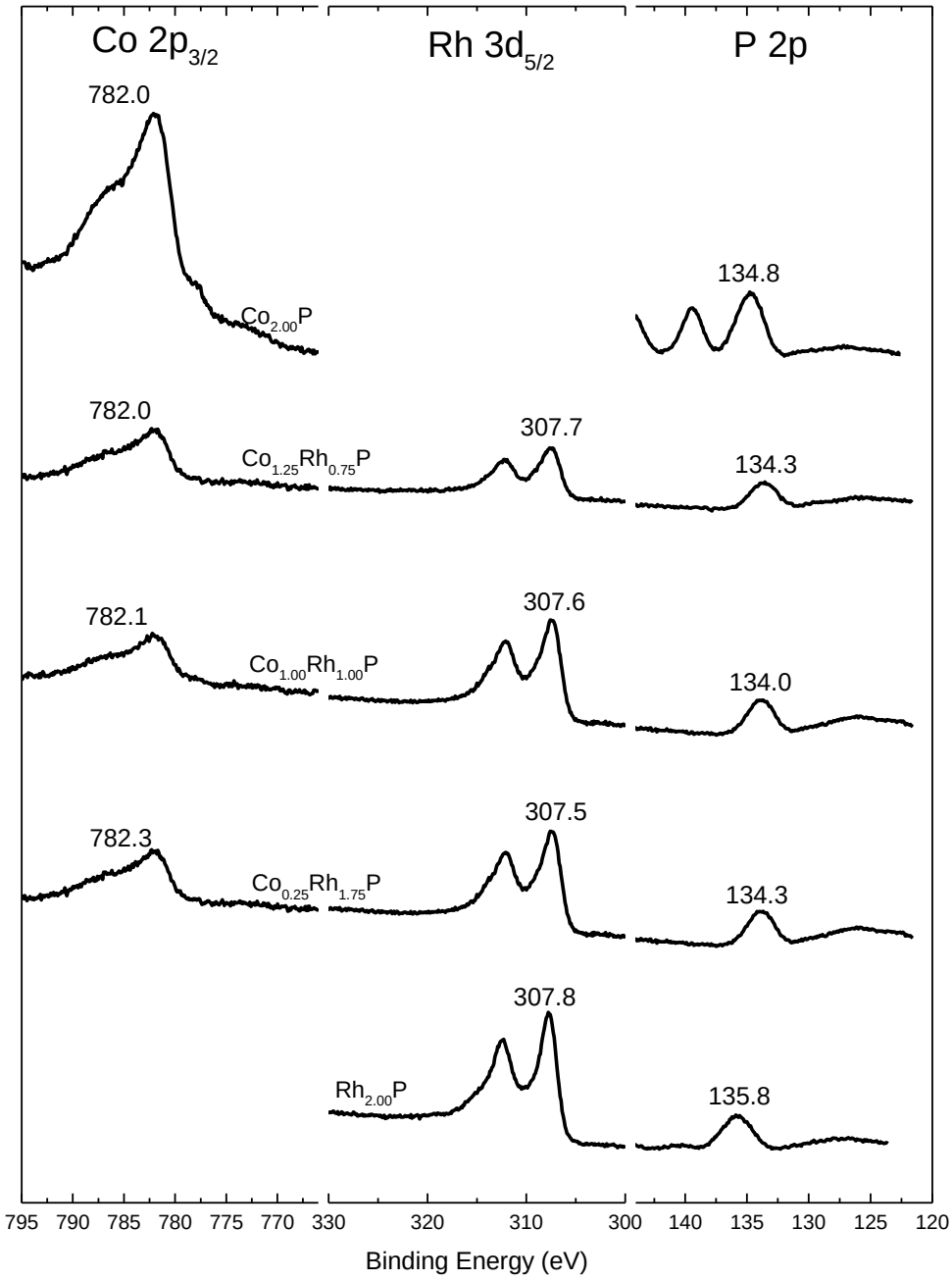

Figure 3.23: XPS spectra of $Co_xRh_{2-x}P/SiO_2$ catalysts.

Surface elemental compositions measured from XPS suggest that the surfaces of $Co_xRu_{2-x}P/SiO_2$ and $Co_xRh_{2-x}P/SiO_2$ catalysts are P-rich.

Table 3.3: Binding energies and surface compositions for select $Co_xRu_{2-x}P/SiO_2$ catalysts.

Nominal Composition	Surface Composition	Surface P/M ratio	P 2p BE (eV)	Co $2p_{3/2}$ BE (eV)	Ru $3d_{5/2}$ BE (eV)
Ru_2P	$Ru_{0.39}P$	2.55	134.6	N/A	280.6
$Co_{0.5}Ru_{1.5}P$	$Co_{0.16}Ru_{0.64}P$	1.24	133.9	781.9	281.1
Co_1Ru_1P	$Co_{0.30}Ru_{0.20}P$	1.96	133.7	781.6	280.6
$Co_{1.5}Ru_{0.5}P$	$Co_{0.61}Ru_{0.24}P$	1.16	133.7	782.1	281.0
Co_2P	$Co_{0.85}P$	1.18	134.8	782.0	N/A

Table 3.4: Binding energies and surface compositions for select $Co_xRh_{2-x}P/SiO_2$ catalysts.

Nominal Composition	Surface Composition	Surface P/M ratio	P 2p BE (eV)	Co $2p_{3/2}$ BE (eV)	Rh $3d_{5/2}$ BE (eV)
Rh_2P	$Rh_{0.57}P$	1.70	135.8	N/A	307.8
$Co_{0.25}Rh_{1.75}P$	$Co_{0.12}Rh_{0.31}P$	2.26	134.3	782.3	307.5
Co_1Rh_1P	$Co_{0.40}Rh_{0.50}P$	1.12	134.0	782.1	307.6
$Co_{1.25}Rh_{0.75}P$	$Co_{0.49}Rh_{0.30}P$	1.25	133.8	782.0	307.7
Co_2P	$Co_{0.85}P$	1.18	134.8	782.0	N/A

3.1.5 Carbon and Sulfur Analysis

Following deoxygenation, the carbon and sulfur contents of deoxygenation-tested catalysts were measured in order to determine the degree of carbon deposition that occurred on the catalyst over the course of testing. The carbon content observed for the $Co_xRu_{2-x}P/SiO_2$ catalysts after furan deoxygenation testing was in the range of 0.29-1.63 wt% and a general trend of decreasing C content with increasing Co content was observed.

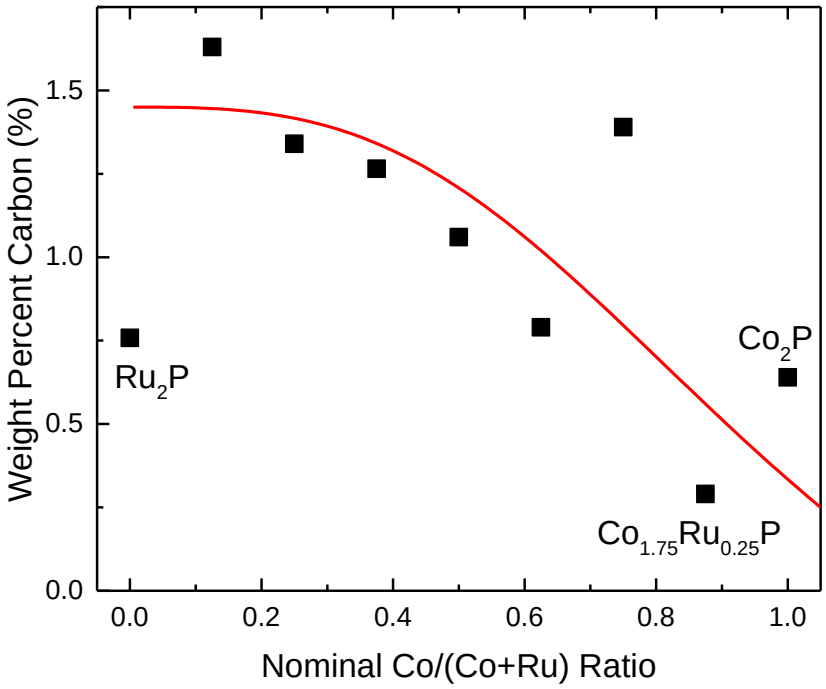

Figure 3.24: Carbon content of $Co_xRu_{2-x}P/SiO_2$ catalysts following furan deoxygenation.

The $Co_xRu_{2-x}P/SiO_2$ (Fig. 3.25) and $Co_xRh_{2-x}P/SiO_2$ (Fig. 3.26) catalysts that underwent crotonaldehyde deoxygenation measurements showed significantly higher carbon contents than the catalysts that underwent furan deoxygenation, with C contents in the 4-6 wt% range. The post-crotonaldehyde deoxygenation Ru_2P/SiO_2 catalyst was found to contain 10.68 wt% C. These high C-contents imply that more coking occurred during the crotonaldehyde conversion reactions than during the furan deoxygenation reactions.

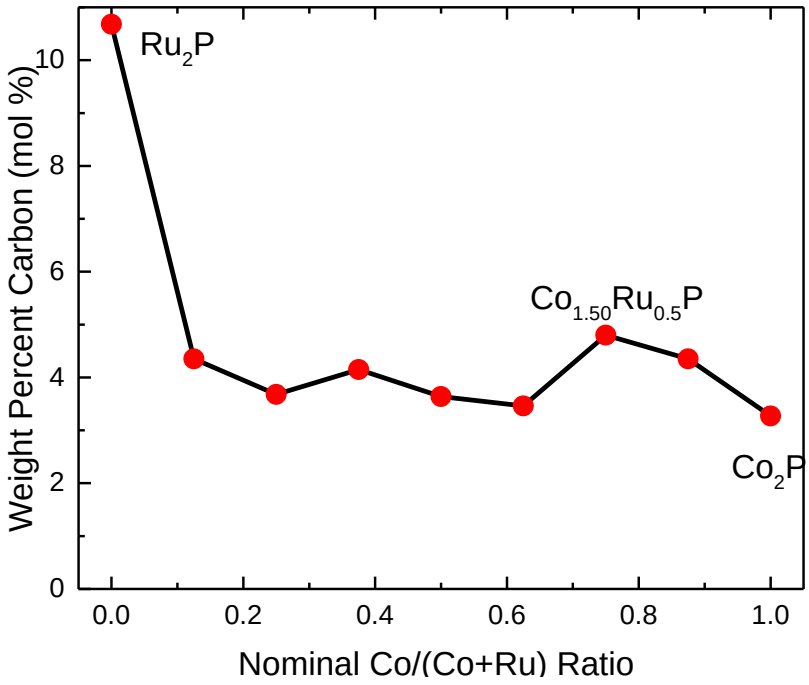

Figure 3.25: Carbon content of $Co_xRu_{2-x}P/SiO_2$ catalysts following crotonaldehyde deoxygenation.

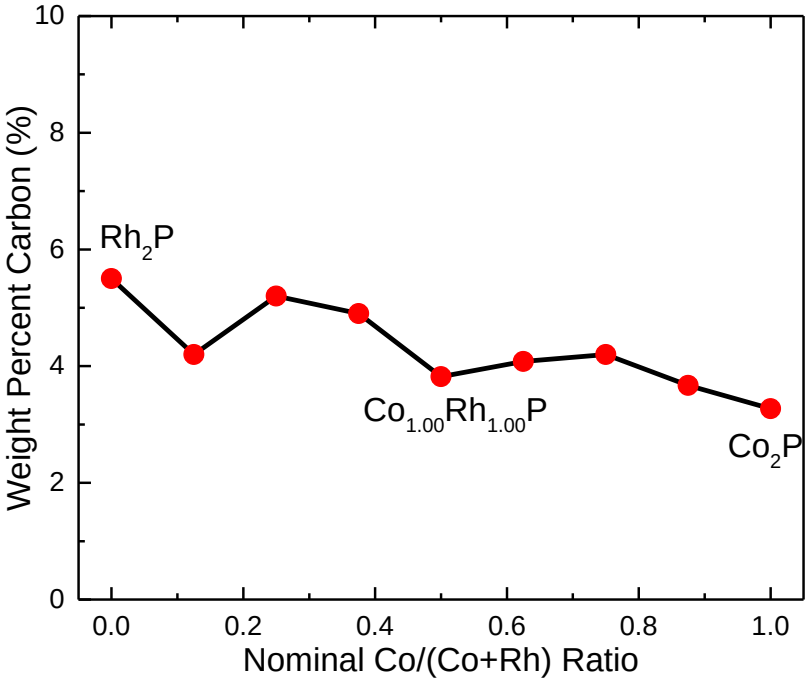

Figure 3.26: Carbon content of $Co_xRh_{2-x}P/SiO_2$ catalysts following crotonaldehyde deoxygenation.

Table 3.5 shows the experimentally determined compositions, average crystallite sizes, BET surface areas, and CO chemisorption capacities measured for the as-prepared 15 wt% $Co_xRu_{2-x}P/SiO_2$ catalysts. The surface areas for the bimetallic phosphide catalysts were similar to each other (271-305 m^2/g) and higher than the surface areas calculated for either Ru_2P (264 m^2/g) or Co_2P (225 m^2/g). The average crystallite sizes as determined by XRD were smaller than 5 nm (the XRD detection limit), with the exception of a few catalysts. The Co-rich samples in the $Co_xRu_{2-x}P/SiO_2$ series were found to possess lower active site densities than the Ru-rich samples as measured via CO chemisorption.

Table 3.5: Summary of characterization data for 15 wt% $Co_xRu_{2-x}P/SiO_2$ catalysts.

Nominal Composition	Experimental Composition	Surface Composition	Average Crystallite Size (nm)	Surface Area (m^2/g)	CO Chemisorption Capacity (μmol CO/g)
Ru_2P	$Ru_{1.75}P_{1.00}$	$Ru_{0.39}P$	7	264	200
$Co_{0.25}Ru_{1.75}P$	$Co_{0.37}Ru_{1.26}P_{1.00}$	-	<5	277	268
$Co_{0.5}Ru_{1.5}P$	$Co_{0.85}Ru_{1.48}P_{1.00}$	$Co_{0.16}Ru_{0.64}P$	<5	271	402
$Co_{0.75}Ru_{1.25}P$	$Co_{1.13}Ru_{1.33}P_{1.00}$	-	<5	281	226
Co_1Ru_1P	$Co_{1.33}Ru_{1.00}P_{1.00}$	$Co_{0.30}Ru_{0.20}P$	<5	274	255
$Co_{1.25}Ru_{0.75}P$	$Co_{1.61}Ru_{0.78}P_{1.00}$	-	6	282	146
$Co_{1.5}Ru_{0.5}P$	$Co_{1.81}Ru_{0.47}P_{1.00}$	$Co_{0.61}Ru_{0.24}P$	<5	282	120
$Co_{1.75}Ru_{0.25}P$	$Co_{3.2}Ru_{0.39}P_{1.00}$	-	11	305	148
Co_2P	$Co_{2.9}P_{1.00}$	$Co_{0.85}P$	9	227	65

Table 3.6 shows the experimentally determined compositions, average crystallite sizes, BET surface areas, and CO chemisorption capacities measured for the as-prepared 15 wt% $Co_xRh_{2-x}P/SiO_2$ catalysts. The surface areas for the bimetallic phosphide catalysts were similar to each other (243-280 m^2/g) and larger than the surface areas calculated for either Rh_2P (253 m^2/g) or Co_2P (225 m^2/g). The average crystallite sizes as determined by XRD ranged from 5-9 nm. No trend was observed in the CO chemisorption capacities of the $Co_xRh_{2-x}P/SiO_2$ catalysts.

Table 3.6: Summary of characterization data for 15 wt% $Co_xRh_{2-x}P/SiO_2$ catalysts.

Nominal Composition	Experimental Composition	Surface Composition	Average Crystallite Size (nm)	Surface Area (m^2/g)	CO Chemisorption Capacity (μmol CO/g)
Rh_2P	$Rh_{1.20}P_{1.00}$	$Rh_{0.57}P$	6.3	253	61
$Co_{0.25}Rh_{1.75}P$	$Co_{0.30}Rh_{1.25}P_{1.00}$	$Co_{0.12}Rh_{0.31}P$	6	265	62
$Co_{0.5}Rh_{1.5}P$	$Co_{0.41}Rh_{0.96}P_{1.00}$	-	6	280	101
$Co_{0.75}Rh_{1.25}P$	$Co_{0.71}Rh_{0.90}P_{1.00}$	-	5	247	113
Co_1Rh_1P	$Co_{0.70}Rh_{0.67}P_{1.00}$	$Co_{0.40}Rh_{0.50}P$	6	265	128
$Co_{1.25}Rh_{0.75}P$	$Co_{0.89}Rh_{0.53}P_{1.00}$	$Co_{0.49}Rh_{0.30}P$	6	243	90
$Co_{1.5}Rh_{0.5}P$	$Co_{1.10}Rh_{0.34}P_{1.00}$	-	5	267	91
$Co_{1.75}Rh_{0.25}P$	$Co_{1.45}Rh_{0.24}P_{1.00}$	-	8	268	112
Co_2P	$Co_{2.9}P_{1.00}$	$Co_{0.85}P$	9	227	65

3.2 Deoxygenation

3.2.1 Furan Deoxygenation

The furan deoxygenation properties of the 15 wt% $Co_xRu_{2-x}P/SiO_2$ catalysts, as well as for a Ru/SiO_2 catalyst, were measured for 48 h on-stream in order to assess the stability of the catalysts in the reaction conditions (T= 573 K, P = 1 atm) (Figure 3.27).

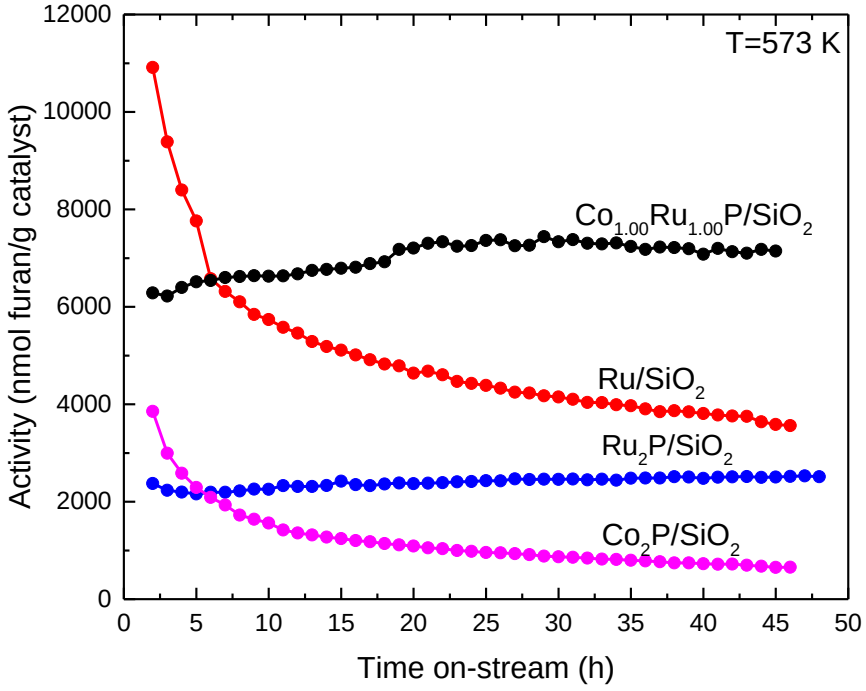

Figure 3.27: Furan deoxygenation activity vs. time at 573 K.

The Ru/SiO_2 catalyst showed a high initial activity followed by rapid deactivation. A Ru_2P/SiO_2 catalyst exhibited a lower furan deoxygenation activity than the Ru/SiO_2 catalyst, but it showed no deactivation over 48 h. A Co_2P/SiO_2 catalyst displayed a low initial furan deoxygenation activity and significant deactivation over time. The 15 wt% $Co_xRu_{2-x}P/SiO_2$ catalysts possessed a high initial

activity compared to either monometallic phosphide, and also showed no deactivation over 48 h. This increased activity and stability when compared to the Ru_2P/SiO_2 and Co_2P/SiO_2 catalysts provides evidence for synergistic effects between Co and Ru in the $Co_xRu_{2-x}P/SiO_2$ catalysts.

The furan deoxygenation activity of the $Co_xRu_{2-x}P/SiO_2$ catalysts were compared after 48 h on-stream (Figure 3.28). The deoxygenation activities of the catalysts depended strongly on the metal composition of the catalyst, with catalysts having higher Co contents (except for Co_2P/SiO_2) showing much higher furan conversion activity than the Ru-rich catalysts.

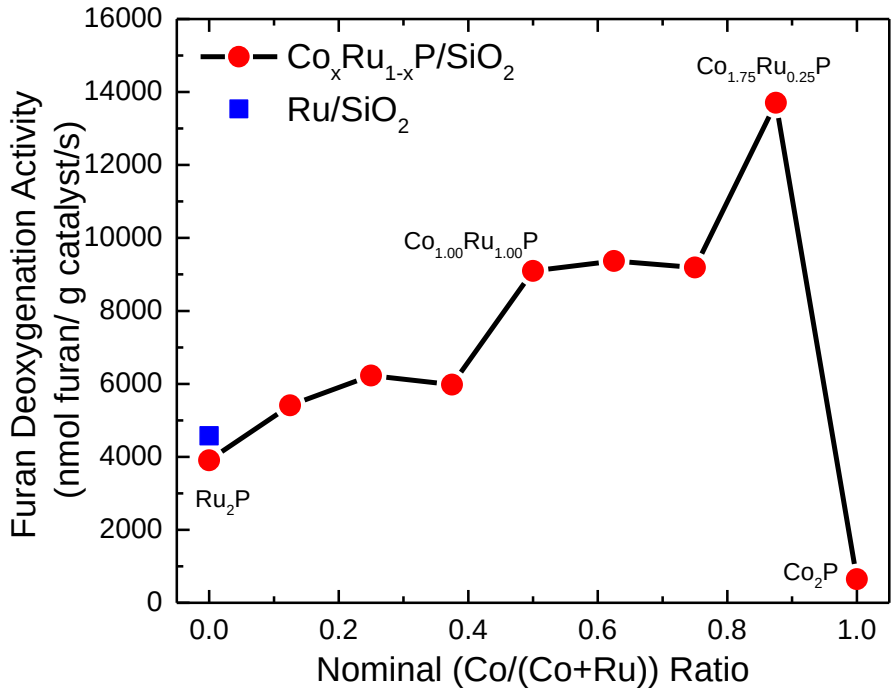

Figure 3.28: Furan deoxygenation activities of $Co_xRu_{2-x}P/SiO_2$ catalysts after 48 h on-stream at 573 K.

The $Co_xRu_{2-x}P/SiO_2$ catalysts exhibited higher furan deoxygenation activities than either of the monometallic phosphides (Ru_2P/SiO_2, Co_2P/SiO_2), further suggesting the presence of synergistic effects between Co and Ru in the bimetallic phosphides. Furan deoxygenation turnover frequencies (TOFs) were calculated for the $Co_xRu_{2-x}P/SiO_2$ catalytic series using their CO chemisorption capacities and furan deoxygenation activities after 48 h on-stream (Figure 3.29). The Co-rich catalysts

possessed higher TOFs than the Ru-rich compositions, with the exception of the Co_2P/SiO_2 catalyst, which had the lowest TOF.

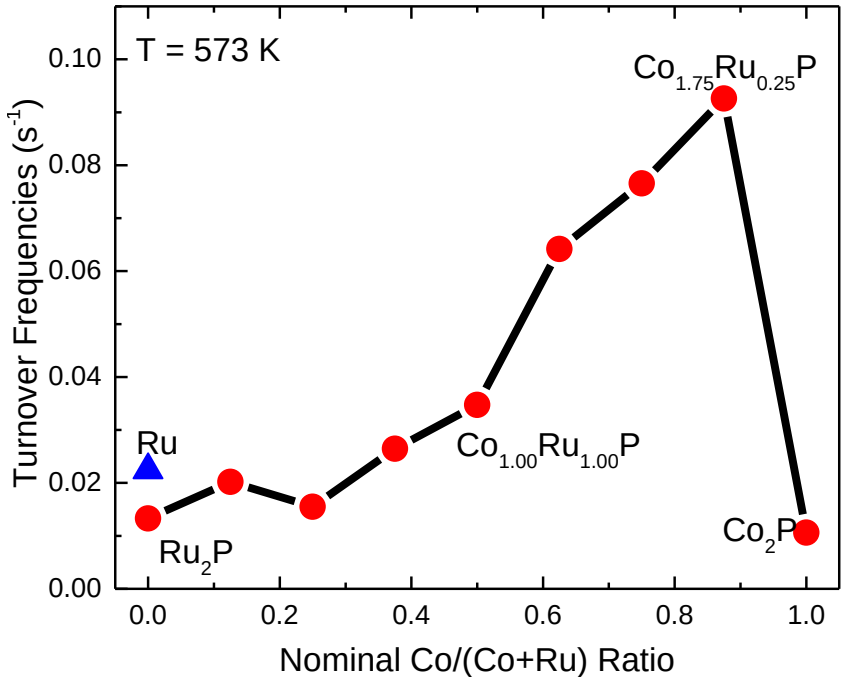

Figure 3.29: Furan deoxygenation TOFs for $Co_xRu_{2-x}P/SiO_2$ catalysts after 48 h on stream at 573 K.

The products generated by furan deoxygenation over the $Co_xRu_{2-x}P/SiO_2$ catalysts were quantified using an on-line GC; the selectivities for a few catalysts are plotted in Figure 3.30. The bimetallic phosphides were found to preferentially remove oxygen via decarbonylation pathways, with a majority of the products being C_3 hydrocarbons (propane and propylene). Other major products included C_4 hydrocarbons (butane, butenes) as well as a small amount of methane. The distribution of products did not change significantly for different bimetallic phosphide compositions; however, there were significant differences between the bimetallic and monometallic phosphide catalysts, with Ru_2P showing a greater propensity towards C_4 hydrocarbon production and Co_2P producing a much larger fraction of C_3 hydrocarbons than the bimetallic phosphides. The Ru/SiO_2

catalyst was shown to produce primarily methane, as well as trace amounts of ethane, propane and butane.

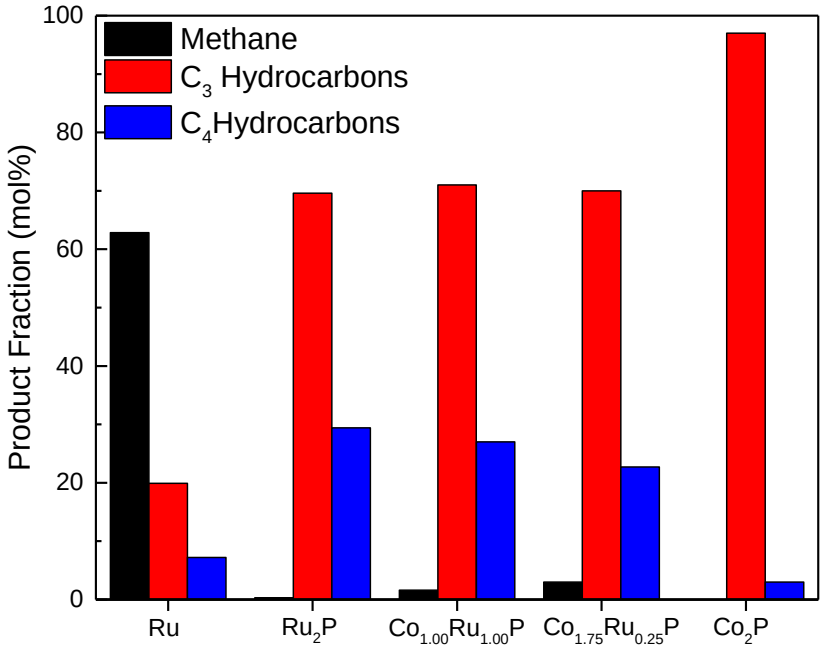

Figure 3.30: Furan deoxygenation product selectivity of selected $Co_xRu_{2-x}P/SiO_2$ catalysts and a Ru/SiO_2 catalyst.

3.2.2 Crotonaldehyde Conversion

Crotonaldehyde was chosen as a model compound because it can be used to investigate deoxygenation and hydrogenation pathways, both of which are relevant to the upgrading of bio-oil. The catalytic reaction network of crotonaldehyde is shown in Figure 3.31. The two likely deoxygenation pathways are shown on the right side of the figure, illustrating either hydrodeoxygenation to form C_4H_y products and water or decarbonylation to form C_3H_y products and carbon monoxide. The hydrogenation pathways available to crotonaldehyde are shown on the left side of the figure; either the C=C bond can be hydrogenated to form butyraldehyde or the C=O bond can be selectively hydrogenated to form crotyl alcohol. Either of those initial hydrogenation products can then be further hydrogenated to form butanol.

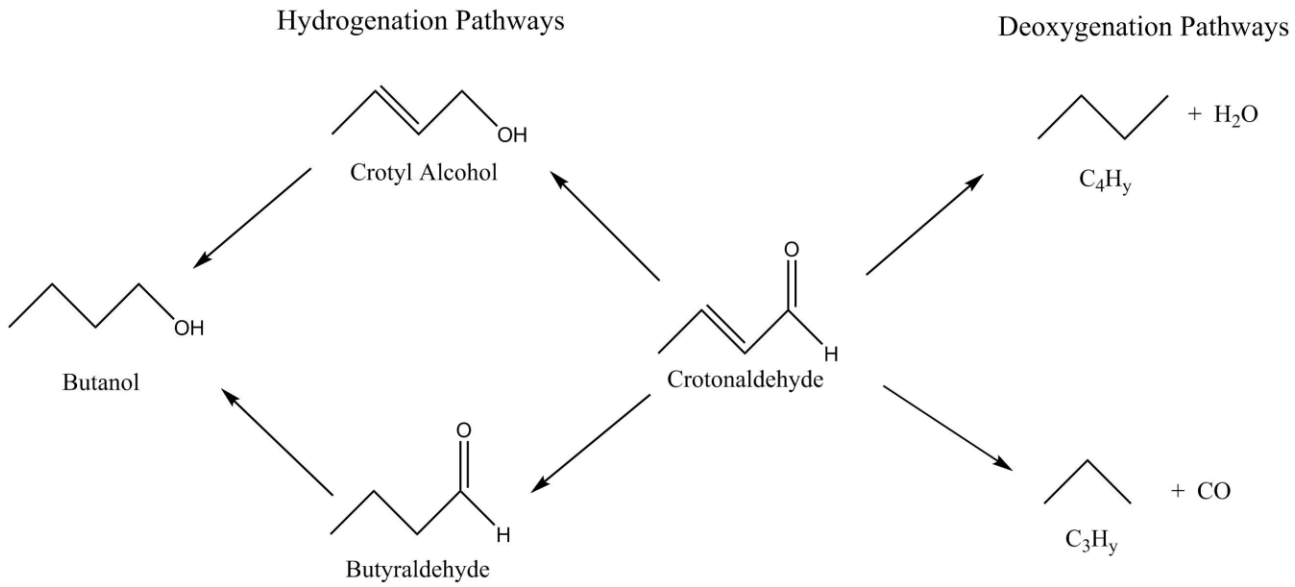

Figure 3.31: Crotonaldehyde reaction network.

$Co_xRu_{2-x}P/SiO_2$ crotonaldehyde deoxygenation

The deoxygenation properties of $Co_xRu_{2-x}P/SiO_2$ catalysts were also investigated using crotonaldehyde as a model compound. The crotonaldehyde deoxygenation measurements were performed at reactor temperatures in the range of 423–573 K, in order to understand how catalyst activity changed with temperature. The Ru_2P/SiO_2 catalyst showed approximately linear increasing crotonaldehyde conversion in the 475-575 K range (Fig. 3.32). Both C_3H_y and C_4H_y products were produced in significant quantities, showing a selectivity towards deoxygenation pathways, with C_3H_y hydrocarbons being selected for more than C_4H_y hydrocarbons. Very little butyraldehyde was observed as a product.

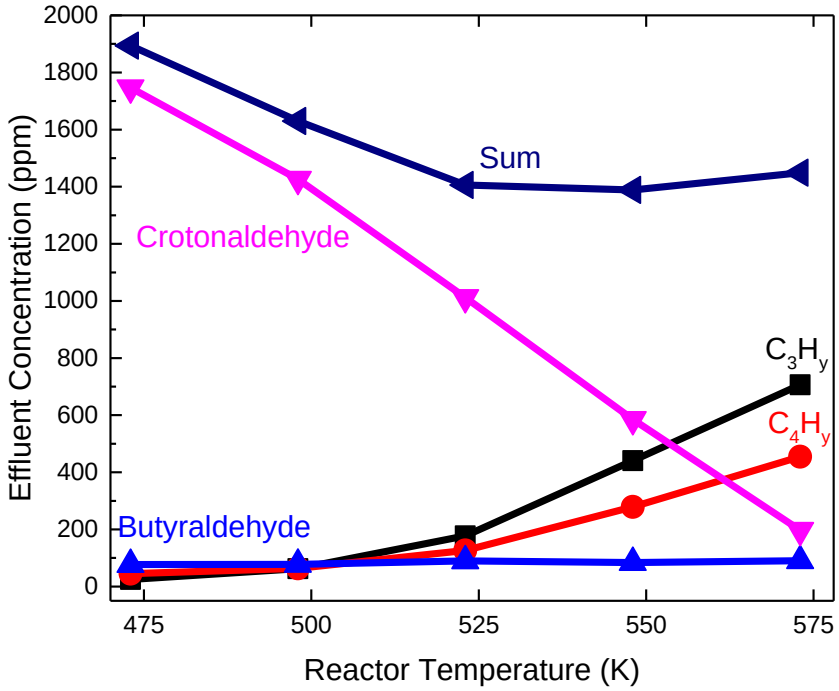

Figure 3.32: Crotonaldehyde conversion products for a Ru_2P/SiO_2 catalyst as a function of the reactor temperature.

The Co_2P/SiO_2 catalyst (Fig. 3.33) also showed increasing crotonaldehyde conversion with increasing temperature. At temperatures in the range 425-500 K, the Co_2P/SiO_2 catalyst showed selectivity towards C_3H_y and C_4H_y products; however, at 525-575 K decarbonylation to C_3H_y products becomes favored over hydrogenation to butyraldehyde, as indicated by a decrease in butyraldehyde and an increase in C_3H_y products. This change in selectivity is likely due to the decarbonylation of butyraldehyde at these temperatures. The Co_2P/SiO_2 catalyst does not convert all of the crotonaldehyde at 575 K.

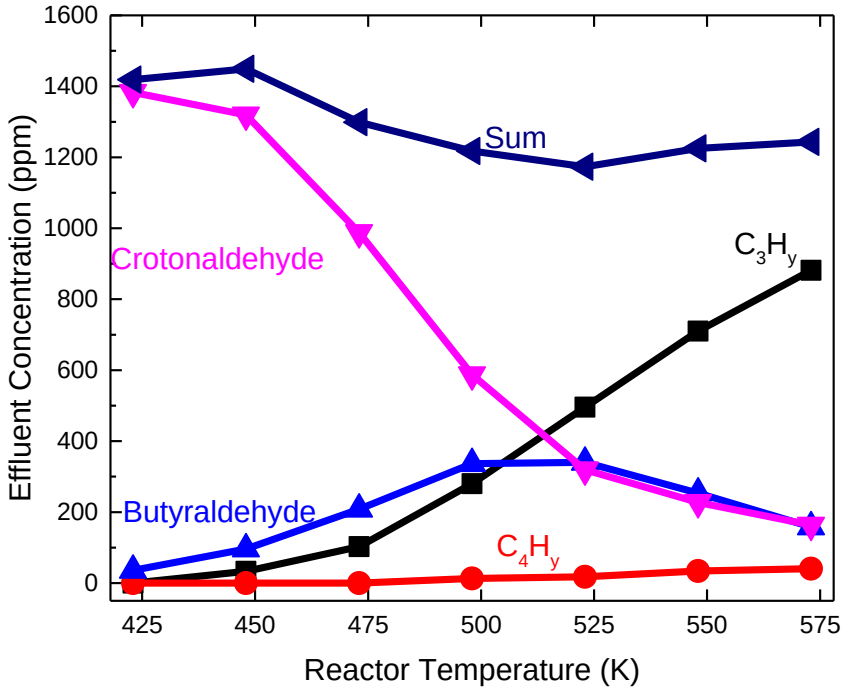

Figure 3.33: Crotonaldehyde conversion products for a Co_2P/SiO_2 catalyst as a function of the reactor temperature.

At temperatures in the range 425-500 K, the $Co_{1.5}Ru_{0.5}P/SiO_2$ catalyst converted crotonaldehyde primarily to butyraldehyde via hydrogenation of the C=C bond (Figure 3.34). At higher temperatures (500-575 K), decarbonylation to produce C_3H_y was favored over hydrogenation to butyraldehyde, as indicated by a decrease in butyraldehyde and an increase in C_3H_y products. By 550 K, crotonaldehyde was no longer detected in the reactor effluent, indicating a complete conversion of crotonaldehyde over the $Co_{1.5}Ru_{0.5}P/SiO_2$ catalyst at this temperature.

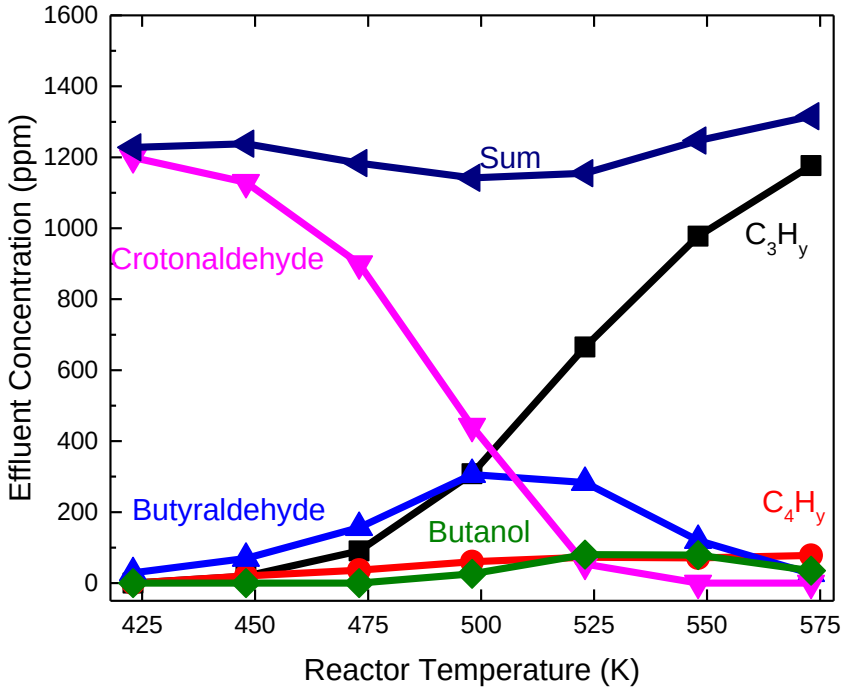

Figure 3.34: Crotonaldehyde conversion products for a $Co_{1.5}Ru_{0.5}P/SiO_2$ catalyst as a function of the reactor temperature.

The crotonaldehyde conversion activity of the $Co_{1.5}Ru_{0.5}P/SiO_2$ catalyst was tested for separate catalyst samples in order to determine the reproducibility of the measurements (Figure 3.35). The two tests had very similar results, indicating high reproducibility. After the second run was performed, the activity of the catalyst was tested at 498 K again, in order to determine whether catalytic deactivation occurred at high temperature (575 K), and it was observed that the activity of the catalyst was slightly higher than it was before. This observation is consistent with the furan deoxygenation measurements, in which bimetallic phosphide catalysts were observed to have increasing deoxygenation activity over 48 h at 573 K (Fig. 3.27).

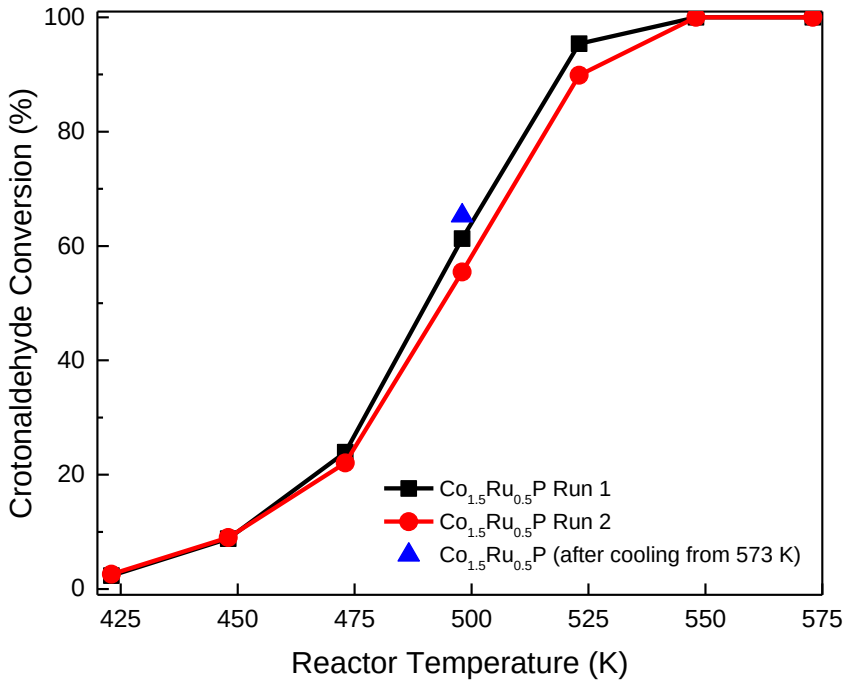

Figure 3.35: Crotonaldehyde deoxygenation conversion vs. temperature for a $Co_{1.5}Ru_{0.5}P/SiO_2$ catalyst.

The crotonaldehyde conversion properties of the series of $Co_XRu_{2-X}P/SiO_2$ catalysts were investigated (Figure 3.36). Similar to the furan deoxygenation results, the crotonaldehyde conversion of the $Co_XRu_{2-X}P/SiO_2$ catalysts was observed to increase with Co content. However, the Co_2P/SiO_2 catalyst out-performed many of the Ru-rich $Co_XRu_{2-X}P/SiO_2$ catalysts, while the Ru_2P/SiO_2 catalyst had the lowest activity of all of the $Co_XRu_{2-X}P/SiO_2$ catalysts. The most active of the $Co_XRu_{2-X}P/SiO_2$ catalysts was the $Co_{1.5}Ru_{0.5}P/SiO_2$ catalyst.

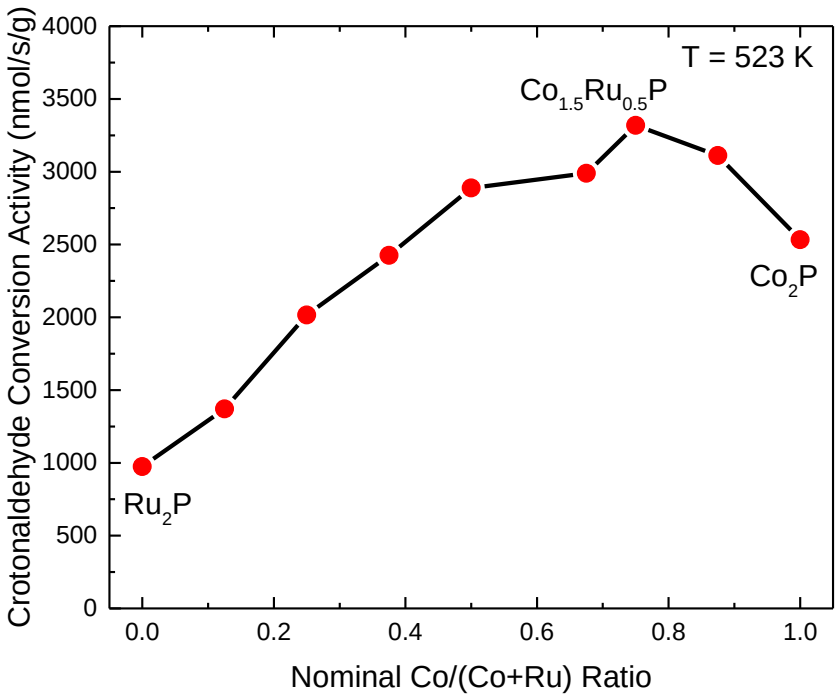

Figure 3.36: Crotonaldehyde conversion activity of $Co_xRu_{2-x}P/SiO_2$ catalysts.

At 523 K, the major products observed in the conversion of crotonaldehyde over $Co_xRu_{2-x}P/SiO_2$ catalysts were C_3H_y hydrocarbons (propane and propylene) produced via the decarbonylation pathway, butyraldehyde produced via the hydrogenation pathway, and C_4H_y hydrocarbons (butane and butenes) produced via the hydrodeoxygenation pathway. A small fraction of butanol was also produced (Fig. 3.37). The product selectivities of the $Co_xRu_{2-x}P/SiO_2$ catalysts depended on metal composition, with higher Co-loading catalysts showing slightly higher selectivities towards C_3H_y products, butyraldehyde, and butanol, and significantly lower selectivity towards C_4H_y products. At 573 K, a different product selectivity was observed (Fig. 3.38); with significantly less butyraldehyde being produced and catalysts selecting primarily for C_3H_y products. Small amounts of C_4H_y hydrocarbons and butanol were produced as well. Product selectivity was dependent upon metal

composition, with higher Ru content resulting in a greater selectivity toward C_4H_y products, while the Co-rich catalysts showed a greater selectivity towards decarbonylation.

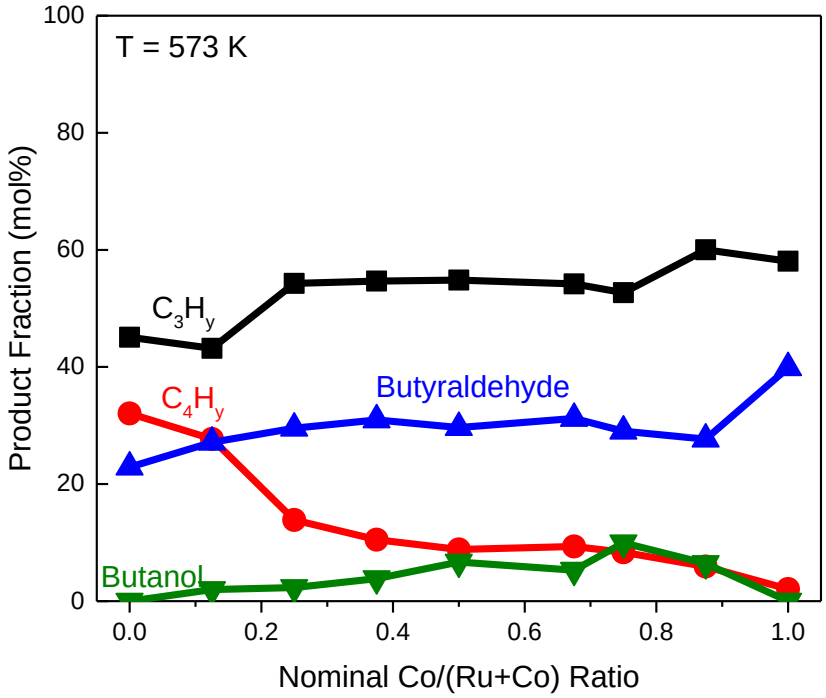

Figure 3.37: Crotonaldehyde conversion product selectivity of $Co_xRu_{2-x}P/SiO_2$ catalysts at 523 K.

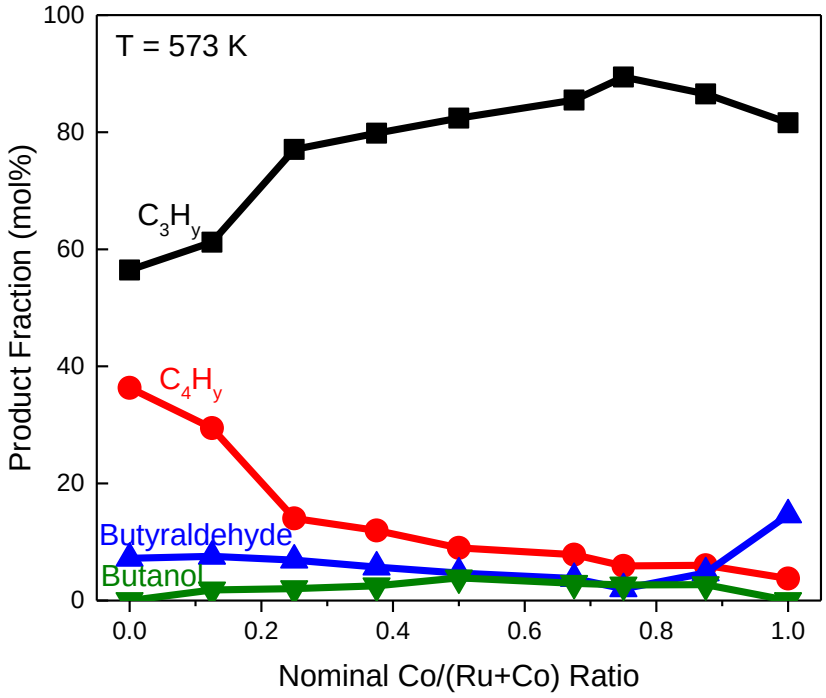

Figure 3.38: Crotonaldehyde conversion product selectivity of $Co_xRu_{2-x}P/SiO_2$ catalysts at 573 K.

Turnover frequencies for crotonaldehyde conversion were calculated for the $Co_XRu_{2-X}P/SiO_2$ catalysts using their CO chemisorption capacities and crotonaldehyde conversion activities at 573 K (Figure 3.39). The trend between the crotonaldehyde conversion TOFs and metal compositions for $Co_XRu_{2-X}P/SiO_2$ catalysts is similar to that observed for the conversion of furan, with higher TOFs found for catalysts with higher Co contents, with the exception of Co_2P, which exhibited a higher TOF for crotonaldehyde than for furan deoxygenation. This difference is likely due in part to the differences between the furan and crotonaldehyde measurements. The furan activity data were collected after 48 h on-stream at 573 K, while the crotonaldehyde conversion data were collected at 25 K intervals for temperatures in the range 473-573 K, with the reactor held at each temperature for 2 h. The Co_2P catalyst may not have undergone deactivation in the crotonaldehyde conversion measurement, while it experienced significant deactivation in the furan deoxygenation measurement.

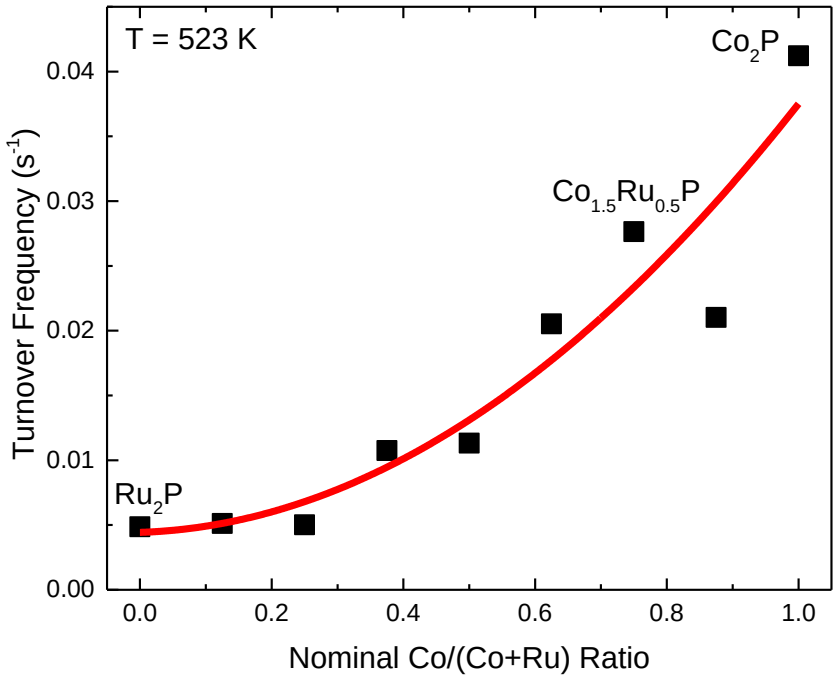

Figure 3.39: Crotonaldehyde conversion TOFs for $Co_XRu_{2-X}P/SiO_2$ catalysts at 523 K.

Crotonaldehyde conversion measurements were carried out for Ru/SiO_2 and Co/SiO_2 catalysts as well; however, the catalysts were observed to be very active and select heavily for products which condensed and flooded the catalyst bed. GC-MS of the condensate collected from the reaction tube showed that it was composed primarily of isobutyl and n-butyl isomers of 1,1-dibutoxybutane (Fig. 3.40). On-line GC the reactor effluent showed butyraldehyde and butanol as products. It is possible that the 1,1-dibutoxybutane products could have been formed by the refluxing of crotonaldehyde hydrogenation products under hydrotreating conditions.

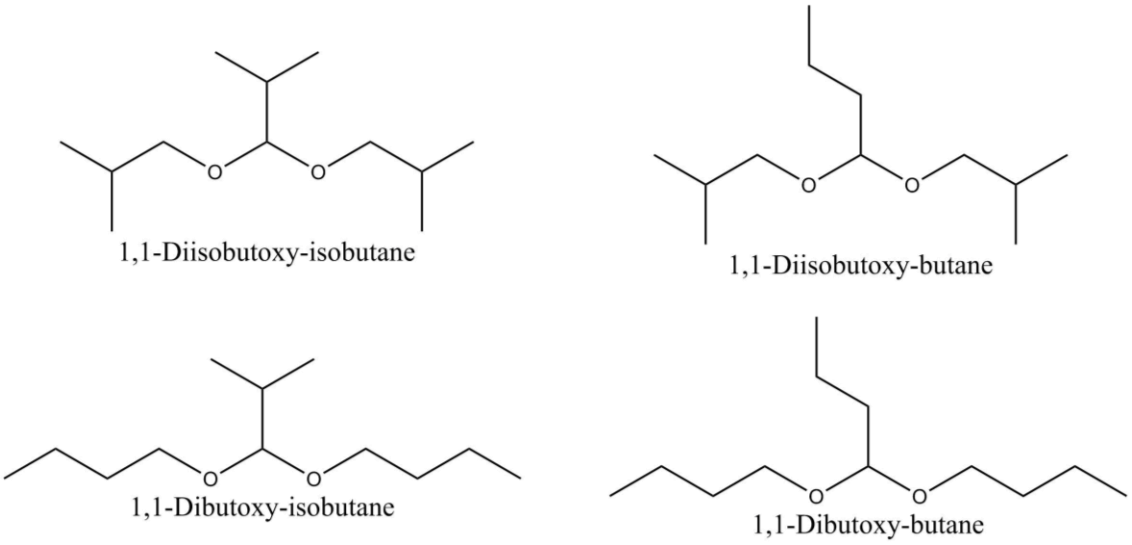

Figure 3.40: Chemical structures determined by GC for the condensate taken from conversion of crotonaldehyde over Ru/SiO_2 and Co/SiO_2 catalysts.

$Co_xRh_{2-x}P/SiO_2$ crotonaldehyde deoxygenation

The deoxygenation properties of $Co_xRh_{2-x}P/SiO_2$ catalysts were studied using crotonaldehyde as a model compound. The crotonaldehyde deoxygenation measurements were performed at reactor temperatures in the range of 303–573 K, in order to probe how catalyst activity changed with temperature. The Rh_2P/SiO_2 catalyst showed conversion of crotonaldehyde at 303 K, and a high selectivity for butyraldehyde (Fig. 3.41). The amount of butyraldehyde produced increased with

increasing temperature in the range 300-400 K, at which point the amount of butyraldehyde produced decreased with temperature, while the production of C_3H_y hydrocarbons increased with temperature. The Rh_2P/SiO_2 catalyst was observed to have complete crotonaldehyde conversion by 400 K. At 498 K, C_3H_y hydrocarbons constituted the majority of the observed products, with a small fraction of butyraldehyde produced as well.

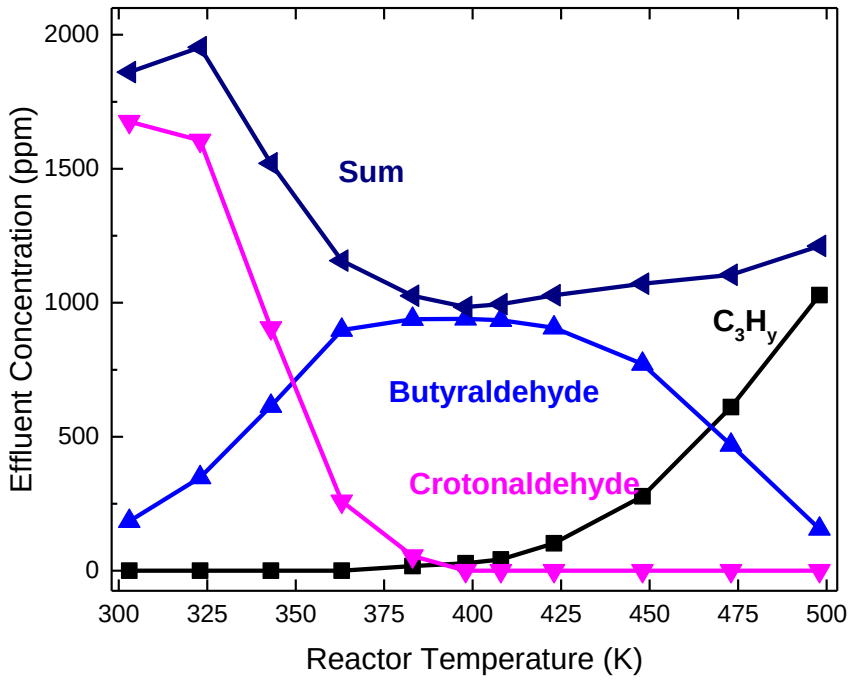

Figure 3.41: Crotonaldehyde conversion product selectivity of Rh_2P/SiO_2 at selected temperatures.

The $Co_{1.00}Rh_{1.00}P/SiO_2$ catalyst (Fig. 3.42) showed very little crotonaldehyde conversion at temperatures in the range 300-450 K, with butyraldehyde being the major product at those temperatures. Above 450 K, crotonaldehyde conversion was observed to increase significantly with temperature, with C_3H_y hydrocarbons observed at 475 K and small amounts of butanol and C_4H_y hydrocarbons also observed. At 500 K, the production of butanol began to decrease with temperature as the decarbonylation pathway become more favored than the hydrogenation

pathway and the production of C_3H_y hydrocarbons began to increase dramatically with temperature. The $Co_{1.00}Rh_{1.00}P/SiO_2$ catalyst was observed to fully convert the crotonaldehyde by 550 K.

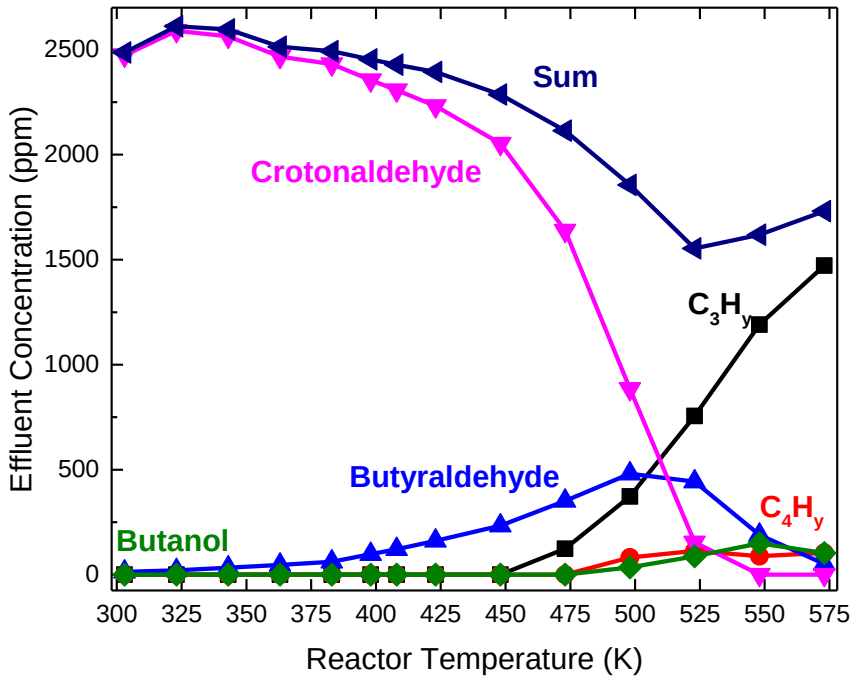

Figure 3.42: Crotonaldehyde conversion product selectivity of $Co_{1.00}Rh_{1.00}P/SiO_2$ at selected temperatures.

At temperatures in the range 300-400 K, a $Co_{0.25}Rh_{1.75}P/SiO_2$ catalyst primarily converted crotonaldehyde to butyraldehyde via hydrogenation of the C=C bond (Figure 3.43). At higher temperatures (400-500 K), however, decarbonylation to C_3H_y products was favored, as indicated by a decrease in butyraldehyde and an increase in C_3H_y products observed. The decrease in selectivity to butyraldehyde was likely due to its decarbonylation to give C_3H_y products.

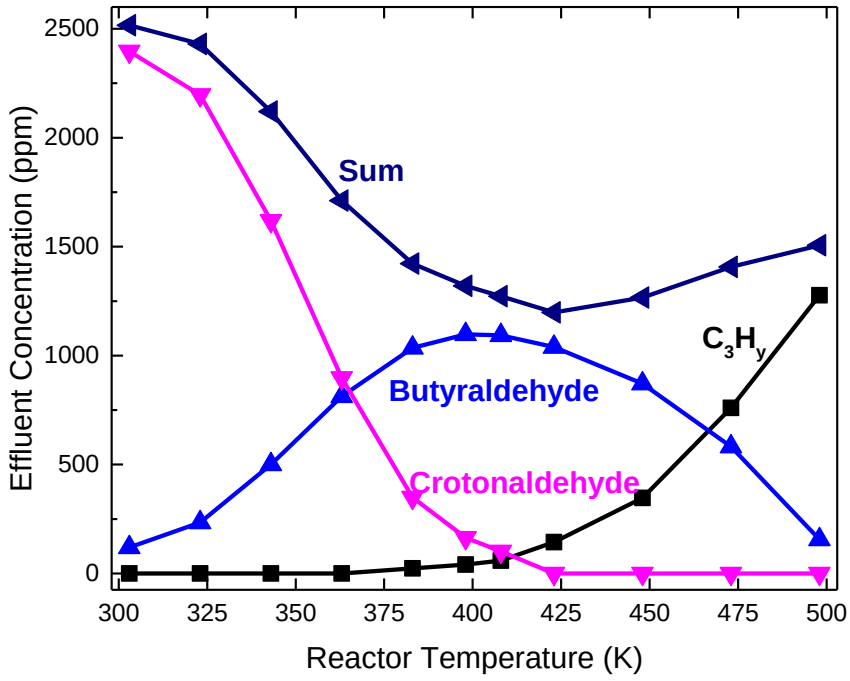

Figure 3.43: Crotonaldehyde conversion product selectivity of $Co_{0.25}Rh_{1.75}P/SiO_2$ at selected temperatures.

The Co-rich $Co_xRh_{2-x}P/SiO_2$ catalysts having high Co contents generally showed lower crotonaldehyde conversion than the high Rh-loading catalysts, with the exception of a significant drop in activity from the $Co_{1.25}Rh_{0.75}P/SiO_2$ catalyst to the $Co_{1.00}Rh_{1.00}P/SiO_2$ catalyst (Fig. 3.44). All of the $Co_xRh_{2-x}P/SiO_2$ catalysts were more active than the Co_2P/SiO_2 catalyst, while the Rh_2P/SiO_2 catalyst was more active than all but the $Co_{0.25}Rh_{1.75}P/SiO_2$ and $Co_{0.5}Rh_{1.5}P/SiO_2$ catalysts. The $Co_{0.25}Rh_{1.75}P/SiO_2$ catalyst was observed to be the most active of all the $Co_xRh_{2-x}P/SiO_2$ catalysts, converting 100% of the crotonaldehyde passed over it at a reactor temperature of 423 K.

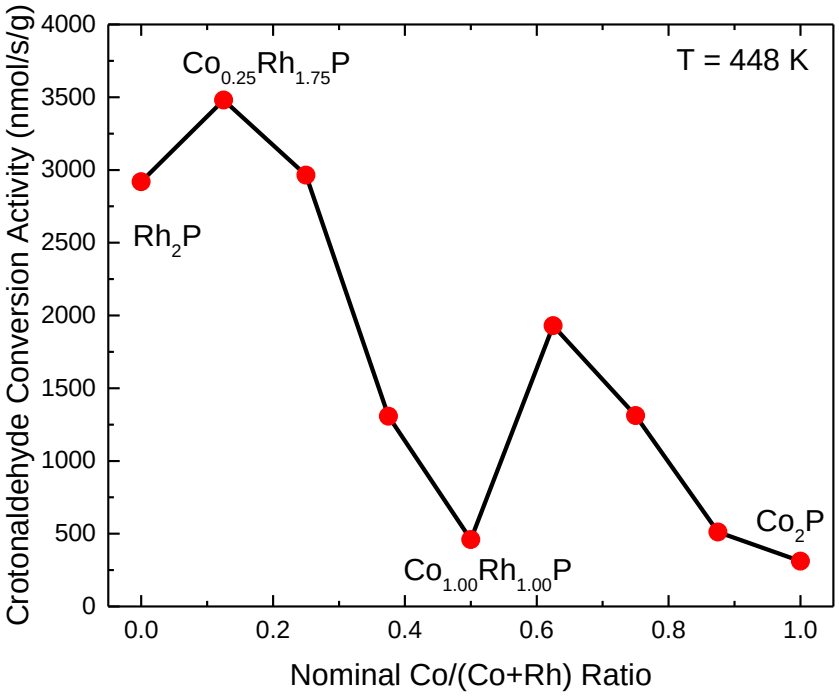

Figure 3.44: Crotonaldehyde conversion activity of $Co_xRh_{2-x}P/SiO_2$ catalysts at 448 K.

At 448 K, the major product observed for crotonaldehyde conversion over the $Co_xRh_{2-x}P/SiO_2$ catalysts was butyraldehyde (Fig. 3.45); C_3H_y hydrocarbons were produced in smaller amounts for most catalyst compositions. Almost no butanol or C_4H_y hydrocarbons were produced at 448 K. The product selectivities appeared to be related to metal composition, with the more active catalysts (Rh_2P/SiO_2, $Co_{0.25}Rh_{1.75}P/SiO_2$, Co_2P/SiO_2) producing a greater fraction of C_3H_y hydrocarbons than the less active catalysts ($Co_{1.00}Rh_{1.00}P/SiO_2$, $Co_{1.75}Rh_{0.25}P/SiO_2$). At 498 K, the major products observed for crotonaldehyde conversion over $Co_xRh_{2-x}P/SiO_2$ catalysts were butyraldehyde and C_3H_y hydrocarbons (Fig. 3.46); small amounts of butanol and C_4H_y hydrocarbons were produced as well.

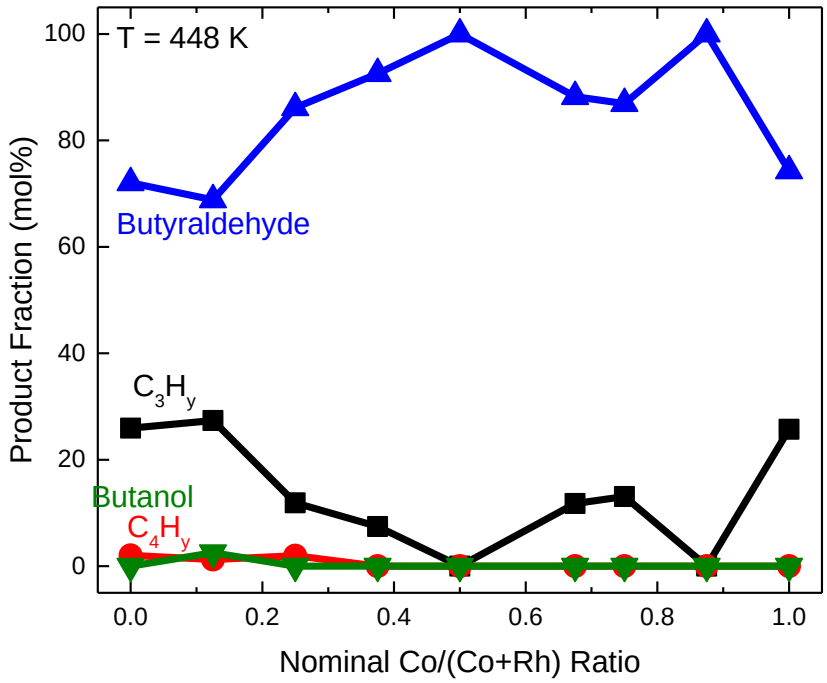

Figure 3.45: Crotonaldehyde conversion product selectivity of $Co_xRh_{2-x}P/SiO_2$ catalysts at 448 K.

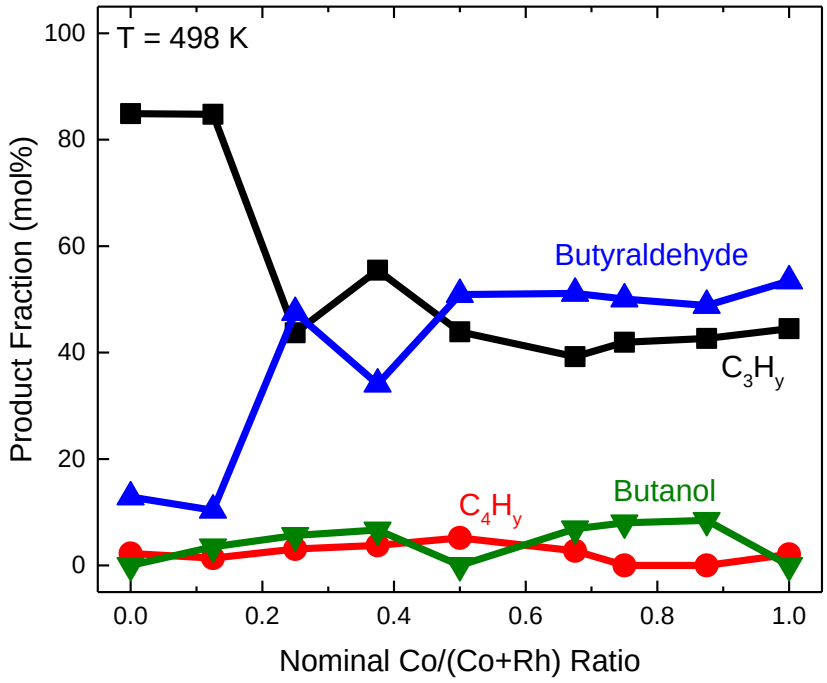

Figure 3.46: Crotonaldehyde conversion product selectivity of $Co_xRh_{2-x}P/SiO_2$ catalysts at 498 K.

Turnover frequencies for crotonaldehyde conversion were calculated for the $Co_XRh_{2-X}P/SiO_2$ catalysts using their CO chemisorption capacities and crotonaldehyde conversion activities at 573 K (Figure 3.47). A decreasing trend is present between Co content and TOF for the $Co_XRh_{2-X}P/SiO_2$ catalysts, with the exception of a large rise in TOF from the $Co_{1.00}Rh_{1.00}P$ catalyst to the $Co_{1.25}Rh_{0.75}P/SiO_2$ catalyst. The $Co_XRh_{2-X}P/SiO_2$ catalysts had higher TOFs than the Co_2P/SiO_2 catalyst, with the exception of the $Co_{1.00}Rh_{1.00}P/SiO_2$ and $Co_{1.75}Rh_{0.25}P/SiO_2$ catalysts. The $Co_{0.25}Rh_{1.75}P/SiO_2$ catalyst possessed the highest TOF.

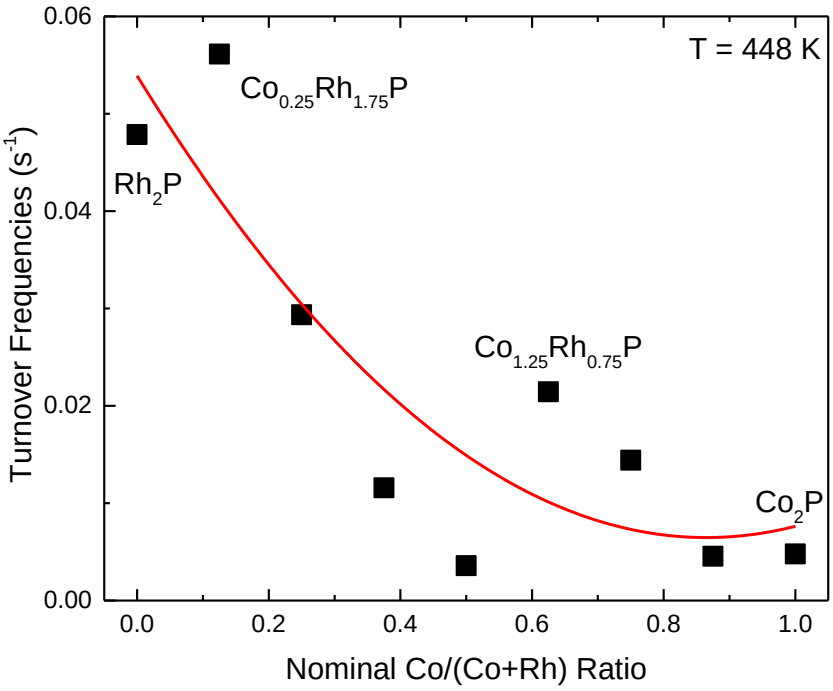

Figure 3.47: Crotonaldehyde conversion TOFs for $Co_XRh_{2-X}P/SiO_2$ catalysts.

4. Discussion

The goals of this research were to synthesize and characterize series of $Co_XRu_{2-X}P/SiO_2$ and $Co_XRh_{2-X}P/SiO_2$ ($0 \leq X \leq 2$) catalysts and to assess their potential as bio-oil hydrotreating catalysts by investigating their furan and crotonaldehyde deoxygenation properties. The chemoselective hydrogenation properties (C=C vs C=O) were also investigated in order to probe the potential of the $Co_XRu_{2-X}P/SiO_2$ and $Co_XRh_{2-X}P/SiO_2$ catalysts as either deoxygenation or mild hydrogenation catalysts for bio-oil stabilization and as selective hydrogenation catalysts for the fine chemicals industry.

There has been significant political, economic, and environmental pressure to transition from the consumption of petroleum-based fuels to the use of alternative sources of energy, due primarily to concern over the amount of CO_2 generated from the combustion of fossil fuel-derived liquid fuels. Liquid fuels make up a significant portion of global energy use, and their consumption is projected to continue to rise in developing nations that lack the resources to pursue more environmentally friendly alternatives.[1,2] While alternative energy sources are being pursued, there are applications in the transportation and industrial sectors where the use of liquid fuels will continue to be a necessity for the foreseeable future. Biofuels are a promising alternative to petroleum-based fuels; they are renewable, possess a smaller carbon footprint than fossil fuels, and can in many cases be mixed directly with petroleum-based fuels. Biofuels also carry the advantage of possessing lower sulfur contents than petroleum fuels, and as such their combustion carries a lower risk of poisoning the expensive catalysts found in emission control devices.[3]

Second generation biofuels, produced from lignocellulosic biomass not fit for human consumption, are currently the most promising type of biofuel, as they do not consume food crops in their production and are not limited by the technological hurdles associated with the production of algal-derived biofuels. The cellulose, hemicellulose, and lignin polymers that compose the

majority of lignocellulosic biomass are long-chain polymers which contain a significant amount of oxygen heteroatoms.[5] In order to produce a liquid fuel from these materials, they must be subjected to a thermochemical degradation process. Fast pyrolysis is typically used in the production of bio-oil over other thermochemical processes due to the low capital investment required and large liquid fraction produced.[4,6,7]

The source of lignocellulosic biomass used in the production of bio-oil has been shown to have a significant effect on the chemical composition of the resulting bio-oil; however, bio-oils produced from lignocellulosic biomass have several undesirable traits in common, including a high water content, high oxygen content, low pH, chemical instability, and a tendency towards phase separation.[6,11,12] These traits make crude bio-oil unusable in most liquid fuel infrastructure, and require that significant upgrading be performed before the bio-oil can be consumed. Most of the undesirable traits of bio-oils can be linked to their high oxygen content, which primarily takes the form of carbonyls, heterocycles, and alcohols. Catalytic removal of this oxygen is key to enabling the use of biofuels as an alternative to petroleum-based fuels.

Many catalytic studies are performed using crude bio-oil as a feed, and such studies are made challenging by the chemical complexity of bio-oil. Many studies now focus on the deoxygenation of model compounds representing common functional groups found in bio-oil.[4,5,16] In this research, furan and crotonaldehyde were chosen as model compounds. Furan was chosen due to the prevalence of heterocyclic rings and furan derivatives in bio-oil, while crotonaldehyde was chosen because it allows for the study of deoxygenation and hydrogenation pathways, and allows for modelling of catalyst potential for both the initial stabilization and later deoxygenation steps present in the process of upgrading bio-oil.

Noble metal catalysts have been shown to be effective deoxygenation catalysts, however, their use in commercial hydrotreating is limited by their prohibitive cost.[12] Many metal phosphide catalysts have been shown to possess desirable catalytic properties such as high catalytic activities and stability under hydrotreating conditions.[16,28,29] Zhao et al. have compared the guaiacol hydrodeoxygenation properties of several transition metal phosphides to those of Pd/Al_2O_3 and $CoMoS/Al_2O_3$ catalysts, and found that the while the metal phosphides were less active than these catalysts, they showed selectivity toward the more desirable deoxygenation products, while the Pd/Al_2O_3 catalysts primarily produced an undesirable hydrogenation product.[16] Noble metal phosphides, such as Ru_2P and Rh_2P, have shown promising catalytic properties compared to their noble metal counterparts; however the high price of noble metals makes such catalysts not economical for use.[31] The use of a bimetallic phosphide catalyst would allow for the expensive noble metals to be diluted with a cheaper metal. Bimetallic phosphide catalysts have shown unique selectivities and greater catalytic activities, and many have shown synergistic effects between metals, allowing for greater activities and unique selectivities than are present in constituent monometallic phosphides.[18,21,22,30,35]

XRD was used to confirm phase purity for the 15 and 25 wt% $Co_xRu_{2-x}P/SiO_2$ catalysts. Peaks in the XRD patterns showed a shift to higher Bragg angles in the Co-rich catalysts. The diffraction patterns of the higher loading catalysts clearly show the presence of only one crystalline phase, indicating that a solid solution was formed in the $Co_xRu_{2-x}P/SiO_2$ catalysts. XRD patterns of $Co_xRu_{2-x}P/SiO_2$ catalysts following furan or crotonaldehyde deoxygenation testing did not show significant increases in crystallite size, suggesting that little or no sintering occurred. $Co_xRu_{2-x}P/SiO_2$ catalysts have not yet been reported in literature; however, Reinkainen et al. have reported the synthesis, characterization, and CO hydrogenation activity of $Co\text{-}Ru/SiO_2$ catalysts.[40] Their results suggest that the bimetallic $Co\text{-}Ru/SiO_2$ catalysts form a mixed Co-Ru phase, rather than separate Co and Ru

phases. These findings are similar to those for the bimetallic phosphide catalysts studied in this research.

XRD was used to confirm the phase purity of the $Co_xRh_{2-x}P/SiO_2$ catalysts. The diffraction patterns for the Co-rich catalysts ($1.00 \leq X \leq 1.75$) were similar to that of a Co_2P reference, while the diffraction patterns for the Rh-rich catalysts ($0.25 \leq X \leq 0.75$) were similar to a Rh_2P reference. The XRD patterns indicate a change in crystal phase occurs from the cubic (Rh_2P) structure for the $Co_{0.75}Rh_{1.25}P/SiO_2$ catalyst to the orthorhombic (Co_2P) structure for the $Co_{1.00}Rh_{1.00}P/SiO_2$ catalyst.

EDX spectra were used to confirm the elemental composition of the $Co_xRu_{2-x}P/SiO_2$ catalysts. The 15 wt% catalysts were found to be generally Co-rich and P-poor relative to the nominal compositions. The disparity between experimental and nominal metal compositions was found to be greater in the catalysts with low Co loadings. Metal compositions for the 25 wt% $Co_xRu_{2-x}P/SiO_2$ catalysts were found to track much more closely to the nominal values; however, they were found to be P-rich relative to the nominal P/M molar ratio of 0.5. EDX was also used to determine elemental compositions of the $Co_xRh_{2-x}P/SiO_2$ catalysts. The low Co-loading catalysts were found to have higher than nominal Co contents, this was similar to the trend observed in the composition for the 15 wt% $Co_xRu_{2-x}P/SiO_2$ catalysts. The $Co_xRh_{2-x}P/SiO_2$ catalysts were also found to possess a higher than nominal P content. The EDX composition results indicate that the synthetic method used to prepare the $Co_xRu_{2-x}P/SiO_2$ and $Co_xRh_{2-x}P/SiO_2$ catalysts is capable of producing catalysts close to the desired compositions. While the synthesis of bimetallic phosphides has not yet been extensively researched; Co_2P/SiO_2, Ru_2P/SiO_2, and Rh_2P/SiO_2 catalysts have all been reported in the literature as having been synthesized via a similar impregnation and TPR technique.[28,31,32,41]

CO chemisorption capacities were used to measure the active site density of the $Co_xRu_{2-x}P/SiO_2$ catalysts. A trend of decreasing CO chemisorption capacity with increasing Co-content was

observed, although the Ru_2P/SiO_2 catalyst showed a lower active site density than the Ru-rich bimetallic phosphide catalysts. The higher active site densities of the Ru-rich $Co_xRu_{2-x}P/SiO_2$ catalysts relative to the Ru_2P/SiO_2 catalyst suggest synergistic effects between metals in the $Co_xRu_{2-x}P/SiO_2$ catalysts. The CO chemisorption capacities found for the Ru_2P/SiO_2 and Co_2P/SiO_2 catalysts are consistent with CO chemisorption capacities found in the literature for Ru_2P/SiO_2 and Co_2P/SiO_2 catalysts.[28,32]

CO chemisorption capacities were used to measure active site densities for the $Co_xRh_{2-x}P/SiO_2$ catalysts. The chemisorption capacities of the $Co_xRh_{2-x}P/SiO_2$ catalysts did not follow the same linear trend observed for the $Co_xRu_{2-x}P/SiO_2$ catalysts. Higher chemisorption capacities were observed for the catalysts near the middle of the series, and lower capacities were observed for both the Rh-rich and Co-rich catalysts. The chemisorption capacities of the bimetallic $Co_xRh_{2-x}P/SiO_2$ catalysts were higher than those for the Rh_2P/SiO_2 or Co_2P/SiO_2 catalysts, supporting the idea that synergistic effects may exist between metals in the $Co_xRh_{2-x}P/SiO_2$ catalysts. The chemisorption capacities found for the Rh_2P/SiO_2 and Co_2P/SiO_2 catalysts are consistent with chemisorption capacities previously reported for Rh_2P/SiO_2 and Co_2P/SiO_2 catalysts.[32,41]

The furan deoxygenation properties of the $Co_xRu_{2-x}P/SiO_2$ catalysts were studied at 573 K. The bimetallic phosphide catalysts showed little variation in product selectivity across different metal compositions, and had similar product distributions to the Co_2P/SiO_2 and Ru_2P/SiO_2 catalysts. The main products were C_3H_y hydrocarbons produced via the decarbonylation pathway, while a smaller amount of C_4H_y hydrocarbons produced via the hydrodeoxygenation pathway were also observed. The product distribution of the metal phosphides differed significantly from that of the Ru/SiO_2 catalyst, which produced primarily methane. This difference in product selectivity, as well as a difference in catalytic activity, between metal phosphide catalysts (e.g. Ru_2P/SiO_2) and their metal counterparts (e.g. Ru/SiO_2) has been reported for metal phosphide phases.[28,29,31,34,41] Bowker et al.

compared the furan deoxygenation properties of Ru_2P/SiO_2 and Ru/SiO_2 catalysts.[28] The Ru_2P/SiO_2 catalyst exhibited similar or higher furan deoxygenation activity, and selected primarily for hydrodeoxygenation products, while the Ru/SiO_2 catalyst selected for decarbonylation products. Hayes et al. compared the dibenzothiophene desulfurization properties of Rh_2P/SiO_2 and Rh/SiO_2 catalysts.[41] The Rh_2P/SiO_2 catalyst had a higher activity than either the Rh/SiO_2 or sulfided Rh/SiO_2 catalysts, and was even found to be more active than a commercial $Ni\text{-}Mo/Al_2O_3$ catalyst. The Rh_2P/SiO_2 catalyst selected primarily for the hydrogenation pathway, while the metal catalysts strongly favored the direct desulfurization pathway.

The Co_2P/SiO_2 and Ru_2P/SiO_2 catalysts possessed lower furan deoxygenation activities than the $Co_xRu_{2-x}P/SiO_2$ catalysts, suggesting synergistic effects between Co and Ru in the bimetallic phosphide catalysts. Reinkainen et al. have reported synergistic effects between metals in $Co\text{-}Ru/SiO_2$ catalysts.[40] The $Co\text{-}Ru/SiO_2$ catalyst showed higher hydrogen and CO uptake than the Ru/SiO_2 or Co/SiO_2 catalysts, and outperformed a physical mixture of the two metal catalysts as well. The $Co\text{-}Ru/SiO_2$ catalyst was also shown to possess unique selectivity compared to either constituent metal catalyst, further confirming the presence of synergistic effects. Reinkainen et al. concluded that Ru acted to reduce Co in the bimetallic system, altering the system's catalytic properties. In this thesis research, a trend was observed that Co-rich $Co_xRu_{2-x}P/SiO_2$ catalysts possessed higher furan deoxygenation activities, with the most active $Co_{1.75}Ru_{0.25}P/SiO_2$ catalyst showing more than double the furan conversion than the least active $Co_{0.25}Ru_{1.75}P/SiO_2$ catalyst. This trend is opposite that observed in the CO chemisorption capacities, in which lower Co-content catalysts showed higher chemisorption capacities then the higher Co-content catalysts (Fig. 4.1).

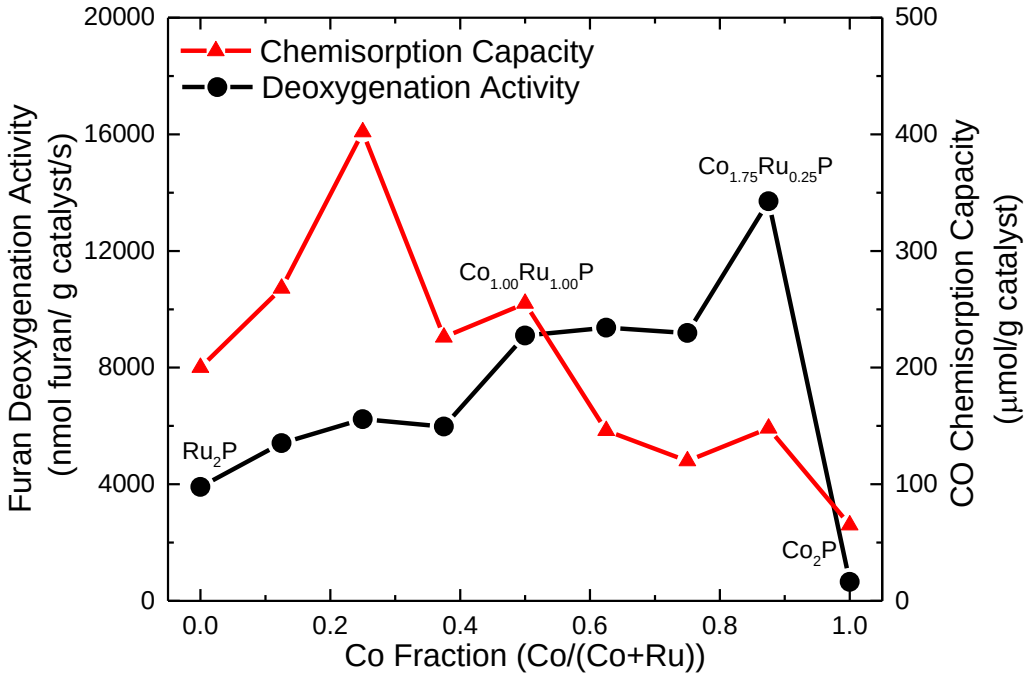

Figure 4.1: CO chemisorption capacity and furan deoxygenation activity of $Co_xRu_{2-x}P/SiO_2$ catalysts.

The trend of higher activity catalysts showing lower chemisorption capacities is reflected in the turnover frequencies calculated for the $Co_xRu_{2-x}P/SiO_2$ catalysts, in which the higher Co-loading catalysts showed significantly higher TOFs than the low Co-loading catalysts. This indicates that the high Co-loading catalysts contain sites that are more active than catalysts with higher Ru-content; this further supports synergistic effects between metals in the bimetallic phosphides. While the bimetallic phosphide catalysts with higher Co-content showed higher activities and TOFs, this trend does not carry over to the Co_2P/SiO_2 catalyst, which was observed to have the lowest activity, TOF, and chemisorption capacity. The fact that the catalysts with lower Ru-content showed higher furan deoxygenation activities suggests that it may be possible to produce an active deoxygenation catalyst by doping an earth abundant metal phosphide (e.g. Co_2P) with small amounts of a more expensive noble metal (e.g. Ru, Rh). In order to optimize these catalysts, it would be necessary to increase their active site densities. One way of accomplishing this would be by increasing the active surface area of the catalyst; this could be accomplished by fine-tuning the temperature

programmed reduction process used in catalyst synthesis, as higher reduction temperatures are likely to cause sintering, which lowers the active site density.

Ru catalysts have been reported in the literature to be promising catalysts for selective hydrogenation reactions,[13,17,18,22] so there was interest in studying the selective hydrogenation properties of the $Co_XRu_{2-X}P/SiO_2$ catalysts. Li et al. reported the selective hydrogenation of crotonaldehyde over a Ru/ZnO catalyst. They found that the surface acidity of the catalyst affected its activity and selectivity, and reported a Ru/ZnO catalyst with a selectivity towards the desired crotyl alcohol product of 88% at 393 K.[17] Martinez et al. report studying the selective crotonaldehyde hydrogenation properties of Ti-doped Ru/SiO_2 catalysts, finding that the bimetallic catalyst had a 30 times greater selectivity towards the desired unsaturated alcohol product at 333 and 353 K.[22] Because many metal phosphide phases exhibit metallic properties, it is possible that doping Ru_2P/SiO_2 catalysts with other metals (e.g. Co) could show similar effects as those observed in doped Ru/SiO_2 catalysts.[29]

The crotonaldehyde hydrogenation/deoxygenation studies were performed to probe changes in catalyst activity and product selectivity across different reactor temperatures (423-573 K). The Ru_2P/SiO_2 catalyst was observed to produce primarily C_3H_y and C_4H_y hydrocarbons through decarbonylation and hydrodeoxygenation pathways, respectively, with little hydrogenation observed. The $Co_XRu_{2-X}P/SiO_2$ and Co_2P/SiO_2 catalysts showed primarily hydrogenation at lower temperatures (423-498 K), indicated by the production of butyraldehyde. At higher temperatures, the amount of observed butyraldehyde decreased and the primary product became C_3H_y hydrocarbons, indicating that butyraldehyde deoxygenation pathways become more accessible at higher temperatures (Figure 4.2).

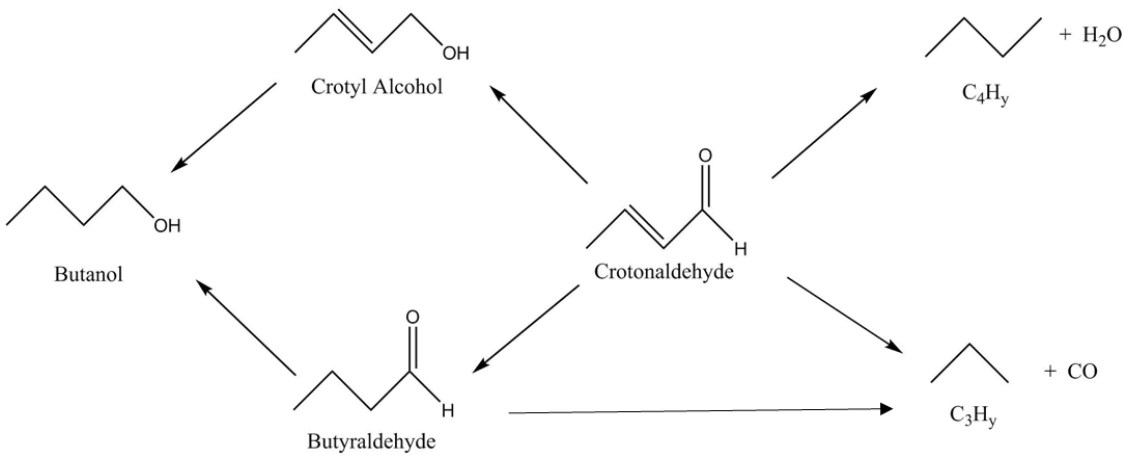

Figure 4.2: Reaction pathways available to crotonaldehyde at higher temperatures.

Product selectivity was observed to change with metal composition, with catalysts having greater Ru-contents observed to produce more C_4H_y hydrocarbons than catalysts with lower Ru-contents. As well, the metal compositions of the $Co_XRu_{2-X}P/SiO_2$ catalysts were observed to affect their preference towards deoxygenation and hydrogenation pathways in crotonaldehyde conversion testing (Fig. 4.3). Ru-rich catalysts were less active, but selected primarily for deoxygenation products; higher Co-loading catalysts were more active, however a large fraction of their increased activity was due to hydrogenation pathways being accessed. Riguetto et al. investigated the effects of Sn addition to Ru/SiO_2 catalysts, and observed decreased hydrogenation of the C=C bond with Sn addition, resulting in a greater selectivity toward hydrogenation of the C=O bond in crotonaldehyde. Additionally, catalysts prepared with different Sn/(Ru + Sn) ratios were found to possess different product selectivities.[18]

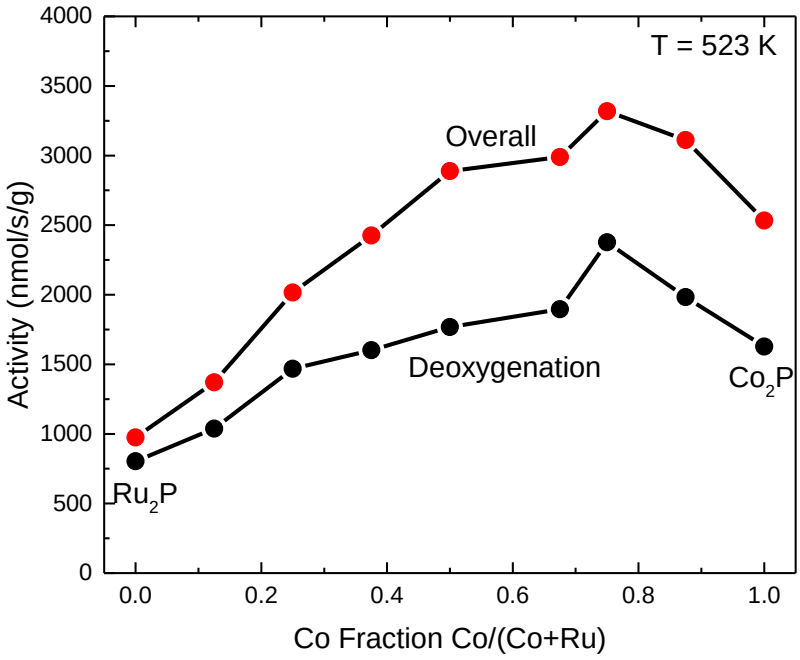

Figure 4.3: Overall crotonaldehyde conversion activity vs. crotonaldehyde deoxygenation activity for $Co_xRu_{2-x}P/SiO_2$ catalysts at 523 K.

There are three main pathways of catalyst deactivation: thermal sintering, CO poisoning, and carbon deposition.[42] XRD patterns of the $Co_xRu_{2-x}P/SiO_2$ catalysts acquired after deoxygenation testing did not show evidence of sintering occurring during the catalytic measurements, as the average crystallite size of the catalyst measured by XRD did not change significantly after deoxygenation testing. This suggests that either CO poisoning or coking are the most likely sources of deactivation. The $Co_xRu_{2-x}P/SiO_2$ catalysts displayed a resistance to deactivation under furan deoxygenation conditions when compared to Ru/SiO_2, Ru_2P/SiO_2, and Co_2P/SiO_2 catalysts, showing no drop in furan deoxygenation activity over 48 h. The Ru/SiO_2 and Co_2P/SiO_2 were observed to experience severe deactivation over the first 10 h under deoxygenation testing conditions. Carbon and sulfur analysis was performed on $Co_xRu_{2-x}P/SiO_2$ catalysts following catalytic measurements, and a trend was observed of decreasing carbon deposition with increasing Co content following the furan deoxygenation measurements, indicating that the most active catalysts showed the lowest

carbon deposition. After crotonaldehyde conversion measurements, the $Co_xRu_{2-x}P/SiO_2$ catalysts possessed lower C content than the Ru_2P/SiO_2 catalyst, suggesting that the incorporation of Co into the Ru_2P phase results in greater resistance to carbon deposition. Carbon and sulfur analysis was also used to quantify the amount of C deposited on the surface of the $Co_xRh_{2-x}P/SiO_2$ catalysts following crotonaldehyde conversion. A slight decreasing trend was observed between deposited carbon and Co-content. In addition, the carbon content for the $Co_xRh_{2-x}P/SiO_2$ catalysts ranged from 4-6 wt% C, which is similar to those measured for the $Co_xRu_{2-x}P/SiO_2$ catalysts following crotonaldehyde conversion. These observations are consistent with coke deposition being a mode of deactivation for the $Co_xRu_{2-x}P/SiO_2$ and $Co_xRh_{2-x}P/SiO_2$ catalysts. The carbon deposition observed following crotonaldehyde conversion was significantly higher than measured after furan deoxygenation, and no trend was observed between bimetallic phosphide composition and carbon deposition, but the Ru_2P catalyst, which had the lowest TOF in the $Co_xRu_{2-x}P/SiO_2$ crotonaldehyde conversion study, was observed to possess twice the carbon deposition as the catalyst with the next highest C content. In a study performed by Li et al. investigating the selective hydrogenation of crotonaldehyde over a Ru/ZnO catalyst, it was found that the primary modes of deactivation for the Ru/ZnO catalyst were the deposition of C on the catalyst surfaces, and poisoning through irreversible binding of CO to Ru active sites.[17]

$Co_xRu_{2-x}P/SiO_2$ catalysts with high Co content showed higher activities in the conversion of crotonaldehyde and the deoxygenation of furan than the low Co content catalysts. The Co_2P/SiO_2 catalyst outperformed the Ru-rich $Co_xRu_{2-x}P/SiO_2$ catalysts in the crotonaldehyde measurements, while in the furan study the Co_2P/SiO_2 catalyst was found to be the least active. This difference in activity may be due to kinetic differences in the conversion of crotonaldehyde vs. furan; it is possible that the Co_2P/SiO_2 catalyst has a low activity for C-O cleavage in the ring opening of furan, while that energy barrier is not present in crotonaldehyde deoxygenation. It is also possible that this difference

in activity is due to differences in methodology between the furan and crotonaldehyde studies; the crotonaldehyde study was performed at lower temperatures and over shorter time spans, and it is possible that the Co_2P/SiO_2 catalysts did not have time to fully deactivate in the crotonaldehyde study. The high activity and low susceptibility to deactivation observed for the $Co_xRu_{2-x}P/SiO_2$ catalysts make them promising for use in bio-oil deoxygenation. As well, the catalysts with the lowest Ru contents were found to be the most active, which is desirable as it allows for reduction in the amount of noble metal used in the $Co_xRu_{2-x}P/SiO_2$ catalysts.

Rhodium catalysts are known to be highly active in hydrotreating reactions. Recently, an Rh_2P/SiO_2 catalyst was shown to be more active in the hydrodesulfurization of dibenzothiophene than either a Rh/SiO_2 catalyst or a commercial $Ni\text{-}Mo/Al_2O_3$ catalyst.[41] Because Rh_2P has been shown to be an effective HDS catalyst, there was interest in investigating the deoxygenation capabilities of a series of $Co_xRh_{2-x}P/SiO_2$ catalysts. An interesting trend was observed between the metal composition of the $Co_xRh_{2-x}P/SiO_2$ catalysts and crotonaldehyde conversion activity. The catalytic activity was found to decrease with increasing Co content, which is opposite the trend observed for the $Co_xRu_{2-x}P/SiO_2$ catalysts (Fig. 4.2). Additionally, a significant drop in crotonaldehyde conversion activity was observed for the $Co_{0.75}Rh_{1.25}P/SiO_2$ and $Co_{1.00}Rh_{1.00}P/SiO_2$ catalysts relative to the other catalysts in the series. The $Co_xRh_{2-x}P/SiO_2$ catalysts showed significantly higher crotonaldehyde conversion than the $Co_xRu_{2-x}P/SiO_2$ catalysts, with the most active catalyst, $Co_{0.25}Rh_{1.75}P/SiO_2$, able to convert 100% of the crotonaldehyde feed at a temperature of 448 K (Fig. 4.4).

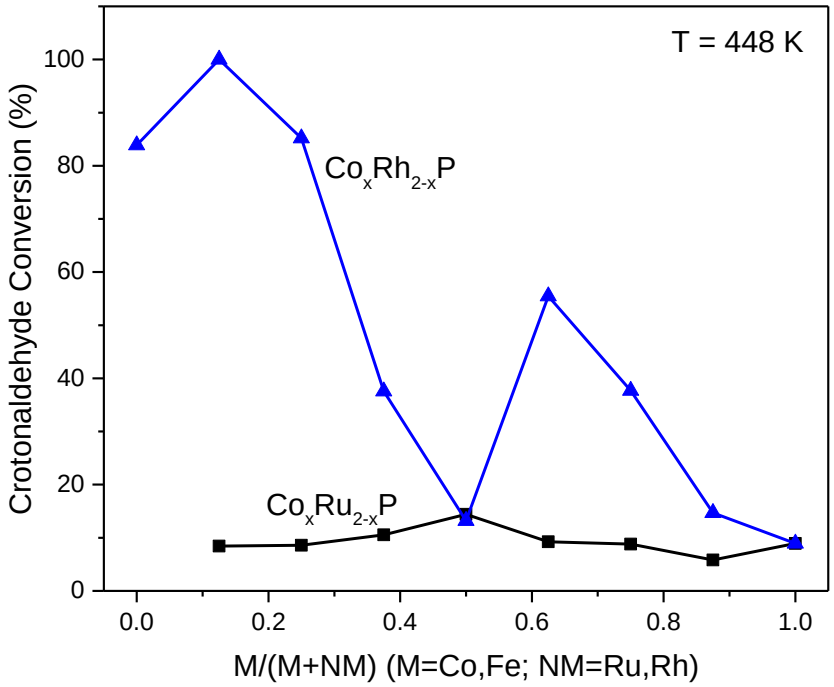

Figure 4.4: Comparison between the crotonaldehyde conversion activities of $Co_xRu_{2-x}P/SiO_2$ and $Co_xRh_{2-x}P/SiO_2$ catalysts

Turnover frequencies calculated for the $Co_xRh_{2-x}P/SiO_2$ catalysts showed a trend of decreasing TOF with increasing Co content. The $Co_{0.25}Rh_{1.75}P/SiO_2$ catalyst possessed a higher TOF than either the Rh_2P/SiO_2 or Co_2P/SiO_2 catalysts, pointing to synergy between Co and Rh in these bimetallic phosphide catalysts. The high activity of the $Co_xRh_{2-x}P/SiO_2$ catalysts at relatively low temperatures combined with their strong selectivity towards deoxygenation pathways makes them promising catalysts for bio-oil deoxygenation reactions; however, this potential is limited by the prohibitive cost of Rh, and the high Rh content in the most active $Co_xRh_{2-x}P/SiO_2$ catalysts.

The product selectivities for crotonaldehyde conversion over the $Co_xRh_{2-x}P/SiO_2$ catalysts were similar to those observed for the $Co_xRu_{2-x}P/SiO_2$ catalysts. At low temperatures, butyraldehyde is primarily produced via the hydrogenation pathway; while at high temperatures, butyraldehyde

production goes down as decarbonylation pathways become more favored, and C_3H_y hydrocarbons become the primary product. Little to no C_4H_y hydrocarbons or alcohol products are observed from the crotonaldehyde conversion over the $Co_xRh_{2-x}P/SiO_2$ catalysts. The deoxygenation activities observed for the $Co_xRh_{2-x}P/SiO_2$ catalysts at 448 K roughly tracked with catalyst activities (Fig. 4.5).

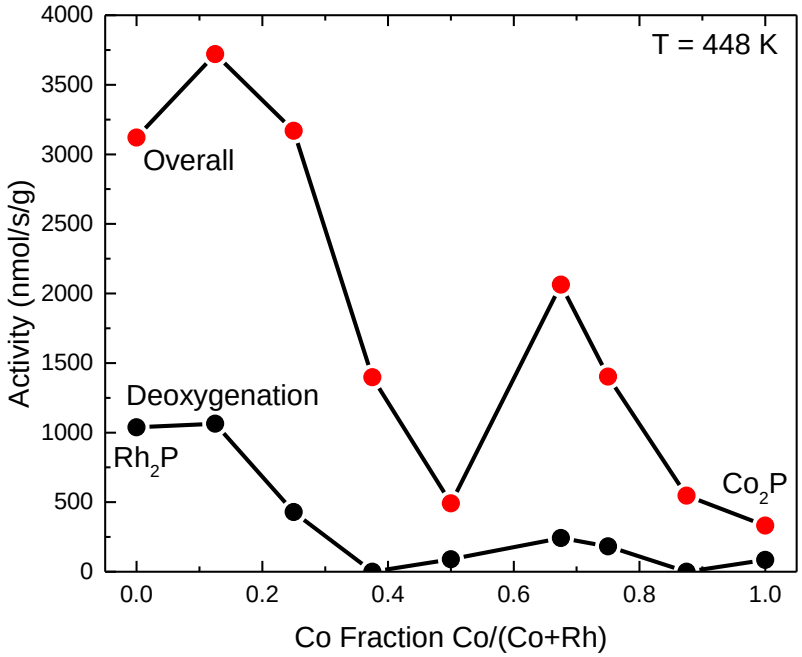

Figure 4.5: Overall crotonaldehyde conversion activity vs. crotonaldehyde deoxygenation activity for $Co_xRh_{2-x}P/SiO_2$ catalysts at 448 K.

While bimetallic catalysts (e.g. Ru-Ti, Ru-Sn) have been reported to show a strong selectivity towards hydrogenation of the C=O bond of crotonaldehyde, It is clear from this research that the $Co_xRu_{2-x}P/SiO_2$ and $Co_xRh_{2-x}P/SiO_2$ catalysts select primarily for C=C hydrogenation and decarbonylation pathways in the conversion of crotonaldehyde. [17-22,30s] It was also observed that at higher temperatures the $Co_xRu_{2-x}P/SiO_2$ and $Co_xRh_{2-x}P/SiO_2$ catalysts are able to access butyraldehyde decarbonylation pathways, resulting in these bimetallic phosphides selecting primarily for C_3H_y products at elevated temperatures.

5. Conclusion

The goals of this thesis research were to synthesize and characterize series of $Co_XRu_{2-X}P/SiO_2$ and $Co_XRh_{2-X}P/SiO_2$ ($0 \leq X \leq 2$) catalysts and to assess their potential as bio-oil hydrotreating catalysts. The $Co_XRu_{2-X}P/SiO_2$ catalysts were tested for furan and crotonaldehyde deoxygenation, as well as for crotonaldehyde hydrogenation. The $Co_XRu_{2-X}P/SiO_2$ catalysts were observed to be active deoxygenation catalysts, selecting primarily for decarbonylation pathways. The deoxygenation activities of the $Co_XRu_{2-X}P/SiO_2$ catalysts tracked strongly with Co-content, with high Co-content catalysts showing higher deoxygenation activity; the most active catalysts were found to be those which contained the least Ru. The bimetallic $Co_XRu_{2-X}P/SiO_2$ catalysts possessed higher furan deoxygenation activities than either of the Ru_2P/SiO_2 or Co_2P/SiO_2 catalysts, showing synergistic effects between Ru and Co in the bimetallic phosphide phases. Additionally, differences in metal composition in the bimetallic phosphides were seen to affect the product selectivities of the catalysts. The Rh-rich $Co_XRh_{2-X}P/SiO_2$ catalysts ($Co_{0.25}Rh_{1.75}P/SiO_2$, $Co_{0.5}Rh_{1.5}P/SiO_2$) were found to be highly active in the deoxygenation of crotonaldehyde, and a decreasing trend in activity was observed with increasing Co content for the $Co_XRh_{2-X}P/SiO_2$ catalysts. The $Co_XRh_{2-X}P/SiO_2$ catalysts showed significantly higher activity than the $Co_XRu_{2-X}P/SiO_2$ catalysts at 448 K; however, butyraldehyde made up a majority of the products at that temperature. The $Co_XRh_{2-X}P/SiO_2$ and $Co_XRu_{2-X}P/SiO_2$ catalysts selected primarily for butyraldehyde in the hydrogenation of crotonaldehyde, showing little to no selectivity for the alcohol products, butanol and crotyl alcohol. The $Co_XRh_{2-X}P/SiO_2$ and $Co_XRu_{2-X}P/SiO_2$ catalysts show high deoxygenation activities, which supports their potential use in the deoxygenation of bio-oil. The $Co_XRu_{2-X}P/SiO_2$ catalysts were most active for the compositions that contained the least Ru; and as such the use of these catalysts would allow for a reduction in the use of noble metals for catalysis. The lack of C=O hydrogenation character makes

the bimetallic phosphide catalysts unlikely to be used in the initial light hydrogenation steps necessary in the upgrading of bio-oil. While the studies performed allowed for investigation into the kinetics of deoxygenation over $Co_XRh_{2-X}P/SiO_2$ and $Co_XRu_{2-X}P/SiO_2$ catalysts, an in-depth mechanistic study would require further investigation into the surface structure of the bimetallic phosphides.

References

1.) Oak Ridge National Laboratory, Transportation Energy Data Book. http://cta.ornl.gov/data/chapter1.shtml (accessed September 2015).

2.) International Energy Outlook 2014, U.S. Energy Information Administration. http://www.eia.gov/forecasts/ieo/ (accessed May 7, 2015).

3.) Bartholomew, C. H.; Agrawal, P. K.; Katzer, R. J., Sulfur Poisoning of Metals. *Advances in Catalysis* **1982**, *31*, 135-242.

4.) Wang, H.; Johnathan, M.; Wang, Y., Recent advances in hydrotreating of pyrolysis bio-oil and its oxygen-containing model compounds. *ACS Catalysis* **2013**, *3*, 1047-1070.

5.) Elliott, D. C.; Hart, T. R., Catalytic hydroprocessing of chemical models for bio-oil. *Energy & Fuels* **2009**, *23*, 631-637.

6.) Dickerson, T.; Soria, J., Catalytic fast pyrolysis: A review. *Energies* **2013**, *6*, 514-538.

7.) Mohan, D.; Pittman, C. U., Jr.; Steele, P. H., Pyrolysis of wood/biomass for bio-oil: A critical review. *Energy & Fuels* **2006**, *20*, 848-889.

8.) Production of Gasoline and Diesel from Biomass via Fast Pyrolysis, Hydrotreating and Hydrocracking: A Design Case. http://www.pnl.gov/main/publications/external/technical_reports/pnnl-18284.pdf (accessed September 2015).

9.) Uddin, N.; Daud, W.; Abbas, H. F., Potential hydrogen and non-condensable gases production from biomass pyrolysis: Insights into the process variables. *Renewable and Sustainable Energy Reviews* **2013**, 27, 204–224.

10.) Dobele, G.; Urbanovich, I.; Volpert, A.; Kampars, V.; Samulis, E., Fast pyrolysis – effect of wood drying on the yield and properties of bio-oil. *BioResources* **2007**, *2*, 699-706.

11.) Elliott, D. C.; Hart, T. R.; Neuenschwander, G. G.; Rotness, L. J.; Olarte, M. V.; Zacher, A. H.; Solantausta, Y., Catalytic hydroprocessing of fast pyrolysis bio-oil from pine sawdust. *Energy Fuels* **2012**, *26*, 3891-3896.

12.) Wildschut, J.; Mahfud, F. H.; Venderbosch, R. H.; Heeres, H. J., Hydrotreatment of fast pyrolysis oil using heterogeneous noble-metal catalysts. *Industrial and Engineering Chemistry Research* **2009**, *48*, 10324-10334.

13.) Mercader, F. M.; Koehorst, P. J. J.; Heeres, H. J.; Kersten, S. R. A.; Hogendoorn J. A., Competition between hydrotreating and polymerization reactions during pyrolysis oil hydrodeoxygenation. *Journal of the American Institute of Chemical Engineers* **2011**, *57*, 3160-3170.

14.) Venderbosch, R. H.; Ardiyanti A. R.; Wildschut, J.; Oasmaa, A.; Heeres, H. J., Stabilization of biomass-derived pyrolysis oils. *Journal of Chemical Technology and Biotechnology* **2010**, *85*, 674-686.

15.) Wildschut, J.; Iqbal, M.; Mahfud, F. H.; Cabrera, I. M.; Venderbosch, R. H.; Heeres, H. J., Insights in the hydrotreatment of fast pyrolysis oil using ruthenium on carbon catalyst. *Energy and Environmental Science* **2010**, *3*, 962-970.

16.) Zhao, H. Y.; Li, D.; Bui, P.; Oyama, S.T., Hydrodeoxygenation of guaiacol as model compound for pyrolysis oil on transition metal phosphide hydroprocessing catalysts. et. al. *Applied Catalysis A: General* **2011**, *391*, 305-310.

17.) Li, B.; Hu, G.; Jin, L.; Hong, X.; Lu, J.; Luo, M., Characterizations of Ru/ZnO catalysts with different Ru contents for selective hydrogenation of crotonaldehyde. *Journal of Industrial and Engineering Chemistry* **2013,** *19,* 250-255.

18.) Riguetto, B. A.; Rodrigues, C. E. C.; Morales, M. A.; Baggio-Saitovitch, E.; Gengembre, L.; Payen, E.; Marques, C. M. P.; Bueno, J. M. C., Ru-Sn catayst for selective hydrogenation of crotonaldehyde: Effect of the Sn/(Ru + Sn) ratio. *Applied Catalysis A: General* **2007**, *318*, 70-78.

19.) Hong, X.; Lu, J.; Li, B. Jin, L.; Hu, G.; Wang, Y.; Luo, M., Selective hydrogenation of crotonaldehyde over supported Ir catalysts: effect of surface acidity on catalysts deactivation. *Indian Journal of Chemistry* **2013**, *52A*, 28-33.

20.) Grass, M. E.; Rioux, R. M., Dependence of gas-phase crotonaldehyde hydrogenation selectivity and activity on the size of Pt nanoparticles (1.7-7.1 nm) supported on SBA-15. *Catalysis Letters* **2009**, *128*, 1-8.

21.) Bachiller-Baeza, B.; Rodriguez-Ramos, I.; Guerrero-Ruiz, A., Influence of Mg and Ce addition to ruthenium based catalysts used in the selective hydrogenation of α,β-unsaturated aldehydes. *Applied Catalysis A: General* **2001**, *205*, 227-237.

22.) Ruiz-Martinez, J.; Fukui, Y.; Komatsu, T., Sepulveda-Escribano, A., Ru-Ti intermetallic catalysts for the selective hydrogenation of crotonaldehyde. *Journal of Catalysis* **2008**, *260*, 150-156.

23.) Badawi, M.; Cristol, S.; Paul, J.; Payen, E., DFT study of furan adsorption over stable molybdenum sulfide catalyst under HDO conditions. *C. R. Chimie* **2009***, 12,* 754-761.

24.) Choe, J.; Lee, C., FTIR and TPD spectroscopic studies of the catalytic hydrodeoxygenation reaction of furan. *J. Ind. Eng. Chem.* **2004,** *10*, 239-246.

25.) Yakovlev, V. A.; Khromova, S. A.; Sherstyuk, O. V.; Dundich, V. O.; Ermakov, D. Y.; Novopashina, V. M.; Lebedev, M. Y.; Bulavchenko, O.; Parmon, V. N., Development of new catalytic systems for upgraded bio-fuels production from bio-crude-oil and biodiesel. *Catalysis Today* **2009**, *144*, 362-366.

26.) Laurent, E; Delmon, B., Influence of water in the deactivation of a sulfided NiMo/γ-Al_2O_3 catalyst during hydrodeoxygenation. *Journal of Catalysis* **1994**, 146, 281-291.

27.) Kubicka, D.; Horacek, J., Deactivation of HDS catalysts in deoxygenation of vegetable oils. *Applied Catalysis A: General* **2011**, *394,* 9-17.

28.) Bowker, R. H.; Smith, M. C.; Pease, M. L.; Slenkamp, K. M.; Kovarik, L.; Bussell, M. E., Synthesis and hydrodeoxygenation properties of ruthenium phosphide catalysts. *ACS Catalysis* **2011**, *1*, 917-922.

29.) Prins, R.; Bussell, M. E., Metal Phosphides: preparation, characterization and catalytic reactivity. *Catal. Lett.* **2012,** *142*, 1413-1436.

30.) Yu, Q.; Zhang, X.; Li, B.; Lu, J.; Hu, G.; Jia, A.; Luo, C.; Hong, Q.; Song, Y.; Luo, M., Effect of reduction temperature on Ru-Ir/ZnO catalyst for selective hydrogenation of crotonaldehyde. *Journal of Molecular Catalysis* **2014***, 392*, 89-96.

31.) Bowker, R. H.; Smith, M. C.; Carillo, B. A.; Bussell, M. E., Synthesis and Hydrodesulfurization Properties of Noble Metal Phosphides: Ruthenium and Palladium. *Topics in Catalysis* **2012**, *55*, 999-1009.

32.) Burns, A. W.; Layman, K. A.; Bale, D. H.; Bussell, M. E., Understanding the relationship between composition and hydrodesulfurization properties for cobalt phosphide catalysts. *Applied Catalysis A: General* **2008**, *343*, 68-76.

33.) Rundqvist, S., The structures of Co_2P, Ru_2P and related phases. *Acta Chemica Scandinavica* **1960**, *14*, 1961-1979.

34.) Abu, I. I.; Smith, K. J., Hydrodenitrogenation of carbozole over a series of bulk Ni_xMoP catalysts. *Catalysis Today* **2007**, *125*, 248-255.

35.) Oyama, S. T.; Zhao, H.; Freund, H. J.; Asakura, K.; Wlodarczyk, R.; Sierfka, M., Unprecedented Selectivity to the direct desulfurization (DDS) pathway in a highly active FeNi bimetallic phosphide catalyst. *Journal of Catalysis* **2012**, *285*, 1-5.

36.) JCPDS—International Centre for Diffraction Data. PDF-4/full file relational database. International Centre for Diffraction data: Newtown Square, Pa. **2002**.

37.) Muniz, F. T.; Miranda M. A.; Santos, C. M.; Sasaki, J. M., The Scherrer Equation and the Dynamical Theory of X-ray Diffraction. *Acta Crystallographica A* **2016**, *72*, 385-390.

38.) Brunauer, S.; Emmett, P. H.; Teller, E., Adsorption of Gases in Multimolecular Layers. *Journal of the American Chemical Society* **1938**, *60*, 309-319.

39.) National Institute of Standards and Technology X-ray Photoelectron Spectroscopy Database. http://srdata.nist.gov/xps/Default.aspx (accessed June 2016).

40.) Reinkainen, M.; Niemela, M.K.; Kakuta, N.; Suhonen, S., Characterization and activity evaluation of silica supported cobalt and ruthenium catalysts. *Applied Catalysis A: General* **1998**, *174*, 61-75.

41.) Hayes, J.R.; Bowker, R.H.; Gaudette, A.F.; Smith, M.C.; Moak C.E.; Nam C.Y.; Pratum, T.K. Bussell, M.E., Hydrodesulfurization properties of rhodium phosphide: Comparison with rhodium metal and sulfide catalysts. *Journal of Catalysis* **2010**, *276*, 249-258.

42.) Batholomew, C.H., Mechanisms of catalyst deactivation. *Applied Catalysis A: General* **2001**, *212*, 17-60.